

CRANFIELD UNIVERSITY

NASSER ALZEANIDI

ANALYSIS OF THE EFFECT OF IMPACT DAMAGE ON THE  
REPAIRABILITY OF CFRP COMPOSITE LAMINATES

School of Aerospace, Transport and Manufacturing

Doctor of Philosophy - PhD

Academic Year: 2013 - 2017

Supervisor: Dr Hessem Ghasemnejad

Feb 2017

CRANFIELD UNIVERSITY

School of Aerospace, Transport and Manufacturing

Doctor of Philosophy - PhD

Academic Year 2013 - 2017

NASSER ALZEANIDI

ANALYSIS OF THE EFFECT OF IMPACT DAMAGE ON THE  
REPAIRABILITY OF CFRP COMPOSITE LAMINATES

Supervisor: Dr Hessem Ghasemnejad

Feb 2017

This thesis is submitted in partial fulfilment of the requirements for the  
degree of PhD

***(NB. This section can be removed if the award of the degree is  
based solely on examination of the thesis)***

© Cranfield University 2017. All rights reserved. No part of this  
publication may be reproduced without the written permission of the  
copyright owner.

## **Abstract.**

Polymer composite materials are common in the aerospace application such as aircraft structures including primary and secondary structures. Therefore, there has been an increasing demand for composites in both the military and civilian aircraft industry. At least 50% of the next generation of military and civil aircraft structures are likely to be made from composites.

The most important properties for composite materials in aircraft application was the high strength-to-weight ratios, stiffness-to-weight ratios and easy to repair. However, the composite materials have low resistance for impact damage. Impact can lead to significant strength reduction in aircraft structure about 40% to 60% of an undamaged composite laminate strength. Therefore, establish a numerical methodology to defined the optimum repair joint to restore sufficient strength of damaged aircraft composite structures during some operations and exercise activities with limited resources which will be the main contributions to knowledge in this thesis.

To achieve this contribution need to understanding of the behaviour of Carbon Fibre Reinforced Plastic (CFRP) composite laminates subject to high velocity impact and the unrepaired composite laminates and repaired (stepped joint) subject to compression after impact test. Therefore, this study consists of two parts:- first, part a combined of numerical simulation and experimental investigation have been used to evaluate the woven CFRP laminate subject high velocity impact. The selected impact velocities were (140m/s, 183m/s, 200m/s, 225m/s, 226m/s, 236m/s, 270m/s, 305m/s, 354m/s and 368m/s) in order to evaluate the induced impact damage in three different thickness of CFRP composite laminates (6 mm, 4.125 mm and 2.625 mm) these velocities were selected according the gas gun limitation.

The woven composite laminate made of Hexcel G0926 Carbon Fabric 5 harness 6K, Areal Weight 370 gsm. The resin used was Hexcel RTM 6, cured for 1 hour 40 minutes at 180° C at a pressure of 100 psi, with an average thickness of

0.375mm. The laminates were comprised of 16 layers, using the following stacking sequence: [(0/90); ( $\pm 45$ ); ( $\pm 45$ ); (0/90); ( $\pm 45$ ); ( $\pm 45$ ); (0/90); (0/90); ( $\pm 45$ ); (0/90); ( $\pm 45$ ); (0/90); ( $\pm 45$ ); (0/90); ( $\pm 45$ ); (0/90)], 11 layers, using the following stacking sequence: 0/90;  $\pm 45$ ; 0/90;  $\pm 45$ ; 0/90;  $\pm 45$ ; 0/90;  $\pm 45$ ; 0/90;  $\pm 45$ ; 0/90;  $\pm 45$ ; 0/90;  $\pm 45$ ; 0/90;  $\pm 45$ ; 0/90;  $\pm 45$ ; 0/90;  $\pm 45$ ; 0/90;  $\pm 45$ . The density of woven CFRP laminates was  $1.512 \times 10^{-3} \pm 1 \times 10^{-6}$  grm/mm<sup>3</sup>.

The penetration process and also change of kinetic energy absorption characteristics have been used to validate the finite element results. The experimental and numerical method in this study show a significant damage occurs, including delamination, compression through thickness failure, out-of-plane shear failure and in-plane tensile failure of the fibres located at the rear surface when the projectile penetrates the laminate. The penetration mechanism of the projectile had a “plugging-type” (shear) failure and the hole that was formed after impact was conical in shape were shown in experimental and also verified in the numerical model. The residual kinetic energy in numerical model is 5.0 % larger than experimental data which is significantly matched in all simulated cases.

In part two a finite element model is established to optimise the repair joint to restore sufficient strength of damaged composite laminate and used compression after impact test to compare the compression failure load of the sample. In order to achieve this an optimised repair models of stepped lap joints with variable parameters such as number of steps and length of steps have been experiment the undamaged composite laminate and composite laminate subject to high velocity impact and also created a numerical model for these experimental. The experimental CAI failure load of undamaged 7 Plies CFRP composite laminate higher than the failure load of damaged specimens by approximately 23%. The undamaged 11 Plies CFRP composite laminate failed at approximately 40% higher than the damaged specimens. Moreover, the difference between the experimental and numerical results of above tests was about 10%.

The numerical model of repaired composite laminate show the damage initiated at the end of overlap and the average compression failure load of the stepped lap joint increased with the increasing of the number of step and length of step. The 85% and 90% of compressive failure load has been restored.

**Keywords:** High Velocity, Impact, Damage, Repair, LSDYNA, Stepped lap joint, CAI

## **Acknowledgments**

I would like to express my appreciation to my thesis supervisor, Dr. Hessem Ghasemnejad for the support and his supervision during this study. Finally, I cannot put into words the gratitude I have for my family, I thank you for all help and support you have given me over the study.

# Table of Contents

<b>ABSTRACT</b> .....	<b>I</b>
<b>ACKNOWLEDGMENTS</b> .....	<b>IV</b>
<b>TABLE OF CONTENTS</b> .....	<b>V</b>
<b>LIST OF FIGURES</b> .....	<b>IX</b>
<b>LIST OF TABLES</b> .....	<b>XIII</b>
<b>NOMENCLATURE</b> .....	<b>XIV</b>
<b>CHAPTER 1 INTRODUCTION</b> .....	<b>1</b>
1.1 RESEARCH BACKGROUND AND CONTEXT.....	2
1.2 POLYMER COMPOSITE MATERIAL IN AIRCRAFT.....	2
1.3 SURVIVABILITY.....	5
1.4 AIMS AND OBJECTIVES OF STUDY.....	7
1.5 PROPOSED CONTRIBUTIONS TO KNOWLEDGE.....	8
1.6 THESIS LAYOUT.....	8
<b>CHAPTER 2 LITERATURE REVIEW</b> .....	<b>10</b>
2.1 BACKGROUND AND CONTEXT.....	11
2.2 IMPACT DAMAGE.....	11
2.3 CLASSIFICATION OF IMPACTS.....	13
2.4 FAILURE MECHANISMS.....	15
2.5 NUMERICAL SIMULATION OF COMPOSITE LAMINATES UNDER HIGH-VELOCITY IMPACT.....	19
2.5.1 <i>Impact Model</i> .....	19
2.6 REPAIR COMPOSITE LAMINATE.....	21
2.6.1 <i>Repair Geometries</i> .....	23
<b>CHAPTER 3 EXPERIMENTAL STUDIES</b> .....	<b>26</b>
3.1 INTRODUCTION.....	27
3.2 GAS GUN TEST RIG.....	28
3.2.1 <i>Gas System</i> .....	28
3.2.2 <i>Gun System</i> .....	29
3.2.3 <i>Chamber Gauge</i> .....	30
3.2.3.1 Valves.....	30
3.2.3.2 Reservoir (chamber).....	31

3.2.3.3	Barrel.....	31
3.2.3.4	Gas release device.....	32
3.2.4	<i>Impact chamber box</i> .....	32
3.2.4.1	Sabot Stopping Device .....	33
3.2.5	<i>Sabot</i> .....	34
3.2.6	<i>Velocity Measurement Systems</i> .....	34
3.2.6.1	ProChrono Digital Chronograph Device .....	34
3.2.6.2	Optoelectronic device.....	35
3.2.6.3	HAMEG (HM8123) specifications:.....	36
3.2.6.4	Projectile Velocity Calibration .....	37
3.2.7	<i>Support System</i> .....	43
3.2.8	<i>Gas Gun Test Alignment</i> .....	44
3.3	EXPERIMENTAL PROCEDURE .....	45
3.3.1	<i>Experiment Materials</i> .....	46
3.3.2	<i>Impact Testing</i> .....	47
3.4	EXPERIMENTAL RESULTS AND VALIDATION .....	48
3.5	COMPRESSION AFTER IMPACT.....	52
3.5.1	<i>Experimental test procedure</i> .....	54
<b>CHAPTER 4</b>	<b>NUMERICAL METHODOLOGY</b> .....	<b>60</b>
4.1	PRACTICAL NUMERICAL METHODOLOGY TO PREDICT THE BEST REPAIR METHOD AFTER IMPACT DAMAGE .....	61
4.2	FINITE ELEMENT ANALYSIS .....	61
4.3	LS-DYNA.....	62
4.3.1	<i>Lagrangian Formulation</i> .....	62
4.3.2	<i>Governing Equations</i> .....	63
4.3.3	<i>Spatial Discretisation</i> .....	65
4.3.4	<i>Central Difference Method</i> .....	66
4.3.5	<i>Time Step Control</i> .....	68
4.4	MODELLING METHODOLOGY.....	69
4.4.1	<i>Modelling Process</i> .....	70
4.5	COMPOSITE MATERIAL MODEL IN LS-DYNA .....	71
4.6	FAILURE CRITERIA.....	73
4.6.1	<i>Fracture Mechanics</i> .....	73
4.6.2	<i>Stress Based Failure Criteria</i> .....	74
4.6.2.1.	Maximum Stress Failure Criterion.....	74
4.6.2.2.	Chang–Chang Criterion .....	75
4.6.2.3.	Tsai-Wu Criterion .....	76



4.7	CONTACT INTERFACES MODELLING.....	78
4.7.1	<i>Hourglass Control</i> .....	79
4.7.2	<i>Energy</i> .....	79
4.8	MATERIAL MODEL.....	79
4.8.1	<i>Projectile Model</i> .....	79
4.8.2	<i>Composite Laminate Model</i> .....	80
4.8.2.1	Composite Laminate Parameters.....	81
4.9	SENSITIVITY ANALYSIS.....	83
4.9.1	<i>Mesh Sensitivity</i> .....	83
4.9.2	<i>Geometrical imperfection</i> .....	84
4.10	IMPACT DAMAGE SIMULATION.....	85
4.11	NUMERICAL REPAIR MODEL.....	86
4.11.1	<i>Stepped Lap Joint Failure Modes</i> .....	86
4.11.2	<i>Material properties</i> .....	89
4.11.3	<i>Adhesive Mesh Sensitivity</i> .....	91
4.11.4	<i>Contact</i> .....	92
4.11.5	<i>Mesh and boundary conditions</i> .....	93
4.12	OPTIMISATION METHOD.....	98
4.12.1	<i>Design Experiments</i> .....	99
4.12.1.1	Repaired composite laminate (4.125 mm).....	99
4.12.1.2	Repaired composite laminate (2.625 mm).....	100
4.13	COMPRESSION AFTER IMPACT.....	100
<b>CHAPTER 5</b>	<b>RESULT AND DISCUSSION.....</b>	<b>102</b>
5.2	IMPACT DAMAGE SIMULATION.....	103
5.3	COMPRESSION AFTER IMPACT.....	109
5.3.1	<i>11 Plies CFRP composite laminate</i> .....	110
5.3.2	<i>7 Plies CFRP composite laminate</i> .....	115
<b>CHAPTER 6</b>	<b>CONCLUSIONS AND FUTURE WORK.....</b>	<b>119</b>
6.1.	INTRODUCTION.....	120
6.2.	CONCLUSION.....	120
6.3.	FUTURE WORK.....	123
	REFERENCES.....	124
	APPENDIX A.....	130
	APPENDIX B.....	137



# List of Figures

FIGURE 1. 1	TIMELINE OF COMPOSITE INTRODUCTION ON AIRCRAFT (AUSTRALIAN TRANSPORT SAFETY BUREAU, 2007).....	3
FIGURE 1. 2	EUROFIGHTER – MATERIAL SELECTION (DILGER ET AL., 2009). .....	3
FIGURE 1. 3	PERCENTAGE OF COMPOSITE MATERIAL OF BOEING AIRCRAFT STRUCTURAL WEIGHT (ROESELER ET AL., 2007). ..	4
FIGURE 2. 1	(A) HYPERVELOCITY IMPACT; (B) HIGH-VELOCITY IMPACT; AND (C) LOW-VELOCITY IMPACT (OLSSON, 2000) ..	14
FIGURE 2. 2	SCHEMATIC REPRESENTATION OF THE IMPACT RESPONSE UNDER (A) LOW-VELOCITY IMPACT AND (B) HIGH- VELOCITY IMPACT (CANTWELL ET AL., 1989).....	14
FIGURE 2. 3	CATEGORISATION OF FAILURE MODES (WOODWARD 1990). .....	16
FIGURE 2. 4	SCHEMATIC DEMONSTRATING THE THREE PRINCIPAL DAMAGE MECHANISMS FOR IMPACT: A) MATRIX CRACKING, B) DELAMINATION, C) FIBRE FAILURE. (CANTWELL ET. AL., 1985).....	17
FIGURE 2. 5	SCHEMATIC REPRESENTATIONS OF DAMAGE PATTERNS: (A) PIN TREE AND (B) REVERSED PAIN TREE (ABRATE, 1998).....	17
FIGURE 2. 6	SHEAR PLUG FAILURE MECHANISM (ABRATE, 1998).....	18
FIGURE 2. 7	FIBRE FAILURE MODE (ABRATE, 1998). .....	18
FIGURE 2. 8	SPRING-MASS MODEL (ABRATE, 1998).....	19
FIGURE 2. 9	COMMON BONDED JOINTS (GUNNION ET AL., 2006).....	23
FIGURE 2. 10	JOINT TYPE VERSUS BOND JOINT STRENGTH (HART-SMITH, 1986).....	24
FIGURE 3. 1	GAS GUN TEST RIG (CRANFIEL UNIVERSITY LAP, 2011).....	27
FIGURE 3. 2	GAS SYSTEM: (A) MAIN GAS CYLINDER; (B) GAGES AND CONTROL FLOW VALVE. ....	28
FIGURE 3. 3	LOW PRESSURE RELIEF VALVE: (A) VALVE DURING EXPERIMENTAL PHASE; (B) DISASSEMBLED LAYOUT. ....	29
FIGURE 3. 4	GAUGE AND VALVES IN GUN SYSTEM.....	30
FIGURE 3. 5	THE GUN SYSTEM RESERVOIR (CHAMBER): (A) CYLINDER WITH SABOT; (B) CYLINDER COVER WITH O RING. ....	31
FIGURE 3. 6	GUN SYSTEM DEVICES: (A) GAS RELEASE DEVICE; (B) BARREL DEVICE. ....	32
FIGURE 3. 7	IMPACT CHAMBER BOX .....	33
FIGURE 3. 8	SABOT STOPPING DEVICE IN THE GUN SYSTEM: (A) SCHEMATIC ILLUSTRATION; (B) OVERVIEW OF THE DEVICE....	33
FIGURE 3. 9	SABOT WITH SPHERICAL STAINLESS STEEL PROJECTILE. ....	34
FIGURE 3. 10	SABOT WITH SPHERICAL STAINLESS STEEL PROJECTILE. ....	35
FIGURE 3. 11	OPTOELECTRONIC DEVICE: (A) OVERVIEW; (B) TWO HOLES CONTAINING LIGHT-PRODUCING DIODE (LED). ....	36
FIGURE 3. 12	THEORETICAL PROJECTILE VELOCITY AND CHAMBER PRESSURE. ....	42
FIGURE 3. 13	SUPPORT FRAME WITH COMPOSITE LAMINATE IN GUN SYSTEM. ....	44
FIGURE 3. 14	ALIGNING THE BARREL WITH THE SPECIMEN: (A) ADJUSTMENT WITH THE POSITION OF THE CENTRE OF THE IMPACT CHAMBER; (B) ADJUSTING THE POSITION OF THE BARREL. ....	44

FIGURE 3. 15 ADJUSTING THE CENTRE OF COMPOSITE LAMINATE IN THE PATH OF PROJECTILE.....	45
FIGURE 3. 16 BOUNDARY CONDITIONS OF THE SUPPORT FRAME. ....	46
FIGURE 3. 17 THE RESIDUAL KINETIC ENERGY OF THE PROJECTILE AGAINST THE INITIAL IMPACT KINETIC ENERGY FOR TWO DIFFERENT THICKNESS COMPOSITE LAMINATES: 2.625MM (7LAYERS) AND 4.125 MM (11 LAYERS). (140M/S TO 479M/s). ....	49
FIGURE 3. 18 IMPACT FAILURE OF 11 LAYERED CFRP WOVEN COMPOST LAMINATE IMPACTED AT 141 J (200 M/s): (A) REAR SURFACE (B) FRONT SURFACE.....	50
FIGURE 3. 19 PETALLING FORMATION FAILURE OF 11 LAYERED CFRP WOVEN COMPOST LAMINATE IMPACTED AT 141 J (200 M/s). ....	51
FIGURE 3. 20 MICROGRAPH OF IMPACT FAILURE OF 7 LAYERED CFRP WOVEN COMPOST LAMINATE IMPACTED AT 141 J (200 M/s). ....	51
FIGURE 3. 21 250 KN INSTRON 8500 TEST RIG (BOEING STANDARD 4ASTM D 7137). ....	52
FIGURE 3. 22 BOEING ANTI-BUCKLING RIG. ....	53
FIGURE 3. 23 EXPERIMENTAL SETUP FOR COMPRESSION AFTER IMPACT (CAI) TEST (CRANFIELD UNIVERSITY LAP, 2013)....	54
FIGURE 3. 24 IMPACT DAMAGED COMPOSITE LAMINATES SUBJECT TO COMPRESSION AFTER IMPACT TEST: (A) 7 PLYS AND (B) 11 PLYS. ....	55
FIGURE 3. 25 COMPOSITE LAMINATES SUBJECT TO COMPRESSION AFTER IMPACT TEST: (A) 7 PLYS AND (B) 11 PLYS. ....	55
FIGURE 3. 26 FAILURE LOAD VERSUS DISPLACEMENT FOR UNDAMAGED AND DAMAGED 7 PLYS CFRP COMPOSITE LAMINATE. .....	57
FIGURE 3. 27 FAILURE LOAD VERSUS DISPLACEMENT FOR UNDAMAGED AND DAMAGED 11 PLYS CFRP COMPOSITE LAMINATE.....	58
FIGURE 3. 28 CAI FAILURE LOAD VERSUS IMPACT VELOCITY FOR DAMAGED 11 PLYS CFRP COMPOSITE LAMINATE. ....	58
FIGURE 3. 29 CAI FAILURE LOAD VERSUS IMPACT VELOCITY FOR DAMAGED 7 PLYS CFRP COMPOSITE LAMINATE. ....	59
FIGURE 4. 1 THREE DIMENSIONAL BODY IN LAGRANGIAN SPACE (LIVERMORE SOFTWARE TECHNOLOGY CORPORATION, 2006). ....	63
FIGURE 4. 2 FINITE ELEMENT MODEL OF A COMPOSITE LAMINATE (100X100MM <sup>2</sup> ) .....	81
FIGURE 4. 3 STRESS (MPA)-TIME (SEC) CURVES OF THE COMPOSITE LAMINATES FOR DIFFERENT MESH SIZE.....	83
FIGURE 4. 4 UNIAXIAL COMPRESSIVE LOAD.....	84
FIGURE 4. 5 FORCE-DISPLACEMENT (MM) CURVES OF THE COMPOSITE LAMINATES FOR DIFFERENT IMPERFECTION PERCENTAGE: (A) LAMINATE SIZE 200MM (B) LAMINATE SIZE 100MM. ....	85
FIGURE 4. 6 FINITE ELEMENT MODEL FOR COMPOSITE LAMINATE SUBJECT TO HIGH VELOCITY. ....	85
FIGURE 4. 7 FAILURE MODES IN COMPOSITE ADHESIVE STEPPED LAP JOINTS (ASTM D5573) .....	87
FIGURE 4. 8 THE SIMULATION GUIDELINE FOR REPAIRING STRATEGY OF IMPACT DAMAGE. ....	88
FIGURE 4. 9 STRESS LEVEL VS. STRAIN RESULTS OF THE ADHESIVES MATERIAL (KIM ET AL. 2006). ....	90
FIGURE 4. 10 SINGLE LAP JOINT MODEL. ....	90

FIGURE 4. 11 SIMULATION AND TEST LOAD–DISPLACEMENT CURVE FOR EA9309.3NA ADHESIVE MATERIAL (KIM ET AL. 2006). .....	91
FIGURE 4. 12 ADHESIVE ELEMENT SIZE. ....	91
FIGURE 4. 13 FORCE-DISPLACEMENT FOR DIFFERENT SIZED ELEMENT.....	92
FIGURE 4. 14 FORCE-DISPLACEMENT CURVE FOR TIEBREAK CONTACT AND TIED CONTACT. ....	92
FIGURE 4. 15 STRESS-ADHESIVE LENGTH CURVE FOR TIEBREAK CONTACT AND TIED CONTACT.....	93
FIGURE 4. 16 HEIGHT AND LENGTH OF EACH STEP (N=3). TOTAL REPAIRED COMPOSITE LAMINATE THICKNESS = 4.125MM, LENGTH (TALL) = 100 MM AND ADHESIVE THICKNESS (D) = 0.375MM. H1=1.125. ....	94
FIGURE 4. 17 CRITICAL POINTS IN EACH STEP. ....	95
FIGURE 4. 18 COMPLETE FE MODEL FOR THE PARENT PART (A) SIDE VIEW &( B) TOP VIEW.....	95
FIGURE 4. 19 STEP AREA INCLUDING JOINT AREA, ADHESIVE AREA AND PARENT AREA. ....	96
FIGURE 4. 20 SLIDING INTERFACE SURFACE. ....	97
FIGURE 4. 21 NUMBER OF STEPS (A); THREE STEPS; (B) FOUR STEPS.....	98
FIGURE 4. 22 BOUNDARY CONDITIONS OF THE CFRP COMPOSITE LAMINATE. ....	101
FIGURE 5. 1 PENETRATION OF 6 MM CFRP LAMINATE BY A 12MM DIAMETER STEEL SPHERE PROJECTILE WITH VELOCITY OF 354 M/S: (A) SIMULATION AND (B) EXPERIMENTAL (HAZELL ET AL., 2008).....	103
FIGURE 5. 2 THE KINETIC ENERGY OF THE STEEL SPHERE PROJECTILE AFTER IMPACT 16 LAYER LAMINATES WITH VELOCITY = 354E+3MM/S, SHOWING THE KINETIC ENERGY (J) VERSUS TIME(S).....	104
FIGURE 5. 3 THE CHANGE IN KINETIC ENERGY OF THE PROJECTILE AGAINST THE INITIAL IMPACT KINETIC ENERGY (120KJ=183M/S AND 485 KJ = 368M/s). ....	105
FIGURE 5. 4 THE CONICAL SHAPED HOLE FORMED ON 6 MM CFRP LAMINATE AFTER IMPACT BY A STEEL SPHERE PROJECTILE VELOCITY OF 305M/S: (A) EXPERIMENTAL RESULTS (HAZELL ET AL, 2008); (B) NUMERICAL RESULTS.....	105
FIGURE 5. 5 THE NUMERICAL RESIDUAL KINETIC ENERGY OF THE PROJECTILE AGAINST THE INITIAL IMPACT KINETIC ENERGY FOR COMPOSITE LAMINATES OF DIFFERENT THICKNESS (2.625MM AND 4.125 MM). (70J=140M/S AND 1180 J = 579M/s). ....	106
FIGURE 5. 6 PENETRATION OF 4.125 MM CFRP LAMINATE BY A 12MM DIAMETER STEEL SPHERE PROJECTILE WITH VELOCITY OF 200 M/S. ....	107
FIGURE 5. 7 IMPACT FAILURE OF 11 LAYERED CFRP WOVEN COMPOST LAMINATE IMPACTED AT 141 J (200 M/s), (A) REAR SURFACE AND (B) FRONT SURFACE. ....	108
FIGURE 5. 8 BOUNDARY CONDITIONS OF THE CFRP COMPOSITE LAMINATE A) FEM AND B) EXPERIMENT.....	109
FIGURE 5. 9 COMPRESSION AFTER IMPACT TEST OF THE 11 PLYES CFRP COMPOSITE LAMINATE (A) EXPERIMENTAL DAMAGED (B) NUMERICAL DAMAGE (C) NUMERICAL UNDAMAGED (D) EXPERIMENTAL UNDAMAGED.....	111
FIGURE 5. 10 FAILURE LOAD VERSUS DISPLACEMENT FOR UNDAMAGED AND DAMAGED CFRP COMPOSITE LAMINATE WITH 11 PLYES. ....	112
FIGURE 5. 11 NUMERICAL COMPRESSION AFTER IMPACT MODEL OF THE REPAIRED 11 PLYES CFRP COMPOSITE LAMINATE.....	112

FIGURE 5. 12 NUMERICAL ANALYSIS ON FAILURE LOAD VERSUS DISPLACEMENT FOR VARIOUS THREE STEPPED LAP JOINT FOR 11 PLYS CFRP COMPOSITE LAMINATE. ....	113
FIGURE 5. 13 NUMERICAL MODELLING ON COMPRESSIVE FAILURE LOAD VERSUS DISPLACEMENT FOR VARIOUS 4-STEPPED LAP JOINT WITH DIFFERENT OVERLAP LENGTH. ....	114
FIGURE 5. 14 STRESS ALONG THE PATH LINE OF MID-SURFACE OF THE STEPPED LAP JOINT.....	114
FIGURE 5. 15 COMPARISON BETWEEN UNDAMAGED AND DAMAGED MODEL WITH DIFFERENT STEPS FOR 11 PLYS CFRP COMPOSITE LAMINATE. ....	115
FIGURE 5. 16 FAILURE LOAD VERSUS DISPLACEMENT FOR UNDAMAGED AND DAMAGE OF CFRP COMPOSITE LAMINATE WITH 7 PLYS. ....	116
FIGURE 5. 17 NUMERICAL MODELLING ON COMPRESSIVE FAILURE LOAD VERSUS DISPLACEMENT FOR VARIOUS 4-STEPPED LAP JOINT WITH DIFFERENT OVERLAP LENGTH FOR 7 PLYS CFRP COMPOSITE LAMINATE. ....	117
FIGURE 5. 18 THE BEHAVIOUR OF A REPAIRED 7 PLYS CFRP COMPOSITE LAMINATE UNDER COMPRESSION LOADING.....	117

## List of Tables

TABLE 2.1 SOME DAMAGE EFFECTS FOR VARIOUS COMPONENTS (AUSTRALIAN TRANSPORT SAFETY BUREAU, 2007) .....	12
TABLE 3. 1 GEOMETRIC PARAMETERS FOR PROJECTILE, CHAMBER AND BARREL. ....	40
TABLE 3. 2 THEORETICAL PROJECTILE VELOCITY. ....	41
TABLE 3. 3 COMPRESSION BETWEEN THEORETICAL PROJECTILE VELOCITY AND EXPERIMENTAL PROJECTILE VELOCITY.....	42
TABLE 3. 4 THE SPECIMENS' PARAMETERS SUBJECT TO CAI TEST.....	56
TABLE 4. 1 COMPOSITE MATERIAL MODELS IN LSDYNA	71
TABLE 4. 2 THE FAILURE MODES FOR THE MAXIMUM STRESS FAILURE CRITERION, CHANG-CHANG CRITERION AND TSAI-WU CRITERION.	77
TABLE 4. 3 MATERIAL PARAMETERS FOR CFRP LAMINATES	82
TABLE 4. 4 MATERIAL PARAMETERS FOR ADHESIVES (KIM ET AL.2006).	89
TABLE 4. 5 THE CONFIGURATION OF THREE STEPS WITH DIFFERENT JOINT LENGTHS.	99
TABLE 4. 6 THE CONFIGURATION OF FOUR STEPS WITH DIFFERENT JOINT LENGTHS.	99
TABLE 4. 7 THE CONFIGURATION OF THREE STEPS WITH DIFFERENT JOINT LENGTHS.	100

## Nomenclature

$P_H$	An aircraft's susceptibility
$P_{K/H}$	An aircraft's vulnerability
$P_s$	An aircraft's survivability
CFRP	Carbon Fibre Reinforced Plastic
FOD	Foreign Object Damage
FRP	Fibre Reinforced Plastic
CAI	Compression After Impact
FEA	Finite Element Analysis
$X_\alpha$	Initial position in Cartesian coordinate system
$X_i$	current position in Cartesian coordinate system
$V_i$	Initial velocity
$t_i$	Forces per unit area
$S_t$	Outer surface
$V$	Whole volume
$\rho$	Density
$x$	Acceleration
$\sigma_{ij}$	Cauchy's stress tensor
$n_j$	Outward normal unit vector
$S_t$	Traction surface
$\delta x_i$	Virtual displacement
$V_m$	Volume of the element
$\delta x_{\alpha i}$	Virtual accelerations
$[M]$	Mass matrix
$\{\ddot{X}\}$	Acceleration vector
$\{F\}$	Vector summation of the internal and external Forces
$\Delta t_n$	Time step
$X_{n+1}$	Displacements
$\dot{X}_{n+1}$	Velocities
$\ddot{X}_{n+1}$	Accelerations
$A_{max}$	Area of the largest side of element
$E$	Young's modulus
$\nu$	Young's modulus
$XX_T$	longitudinal tensile strength
$XX_C$	longitudinal compressive strength
$YY_T$	Transverse tensile strength
$YY_C$	Transverse compressive strength
$S_{BA}$	In plane shear strength
$\sigma_1$	longitudinal stress
$\tau$	Ratio of the shear stress to the shear strength
$G_{12}$	In plane shear modulus
$\sigma_{12}$	Shear stress
$\sigma_2$	Transverse stress
FD	Dynamic friction



FS	Static friction
HGE	Hourglass Energy
IE	Internal Energy
KE	Kinetic Energy
$S_{CA}$	Transverse shear strength in CA
$S_{CB}$	Transverse shear strength in CB
$ZZ_T$	The tensile through thickness strengths
$ZZ_C$	The compression through thickness strengths
$L$	The length of steps
$n$	The number of steps
$r$	Radius of damage area
$h$	Step high
$TAD$	Total repaired composite laminates thickness
$Tall$	Total repaired composite laminate length
$D$	Adhesive thickness
TL	Overlap lengths
$dQ$	Heat
$dw$	The work
$du$	Internal energy
$P$	Pressure
$V$	Volume
$c_v$	Specific heat
$T$	Temperature
R	The gas constant
$\gamma$	The ratio of specific heats
$V_c$	Chamber (reservoir) volume
$P_c$	Chamber (reservoir) pressure
$V_T$	Total volume (chamber and barrel)
$P_T$	Total pressure (chamber and barrel)
$F$	Impact load
$A$	Specimen area
$E_T$	Transfer energy
$E_i$	Impact energy
$E_R$	Residual energy
$m_P$	Mass of the projectile
$v_i$	Impact velocity
$v_R$	Residual Velocity



# **Chapter 1**

## **Introduction**

## **1.1 Research background and context**

The polymer composite materials have many advantages and some disadvantage such as minimised production costs, high strength-to-weight and stiffness-to-weight ratios; aerodynamic smoothness; resistance to fatigue and corrosion; and ease of repair and maintenance. Moreover, these materials can be easily moulded into complex curved shapes necessary for use on aircraft. The disadvantages for these materials were the stiffness and strength properties that can be vary with impact, for example low resistance for impact damage.

Aerospace industries have been seeking ways to restore sufficient strength to the damaged composite structures to ensure continued safe operation by repair the damage. There are many parameters that affect engineering decisions concerning which type of repair used, such as aerodynamics, residual strength, the strength restoration requirement. Therefore, a wide variety of joints have been designed over the years such as overlap joint, scarf, and stepped-lap. Stepped-lap repairs are the preferred methods of repair when there is a requirement for high-strength recovery or a flush surface is needed to satisfy the aerodynamic requirements of a damaged composite aircraft structure.

## **1.2 Polymer Composite Material in Aircraft**

Polymer composite materials are a physical combination of two or more materials, generally consisting of fibre reinforcement and a matrix that both holds the fibres together and fills the voids between them (Dorworth et al., 2009). This matrix structure allows stress transfer between the fibres. The composite laminates formed from more than one plies, increasing strength and allowing the composite to be used as a structural material. The name of the composite usually identifies what the fibre and matrix materials are, e.g., glass/epoxy or carbon/epoxy.

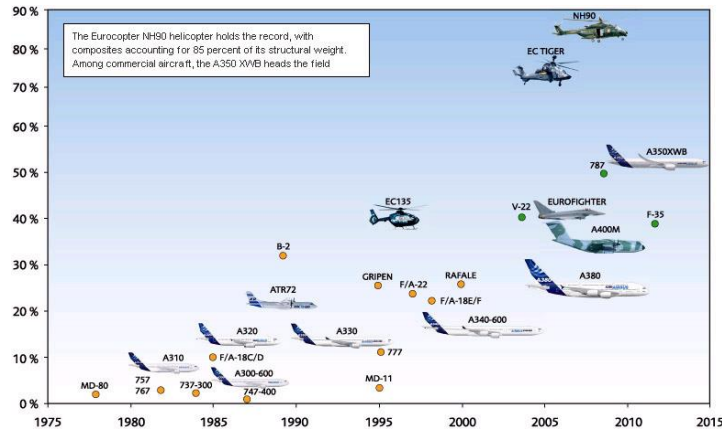


**Figure 1. 1 Timeline of Composite Introduction on Aircraft (Australian Transport Safety Bureau, 2007).**

Polymer composite materials are common in a variety of applications and have been used in the aerospace industry for the last thirty years for the structures of new generation aircraft, missiles, and satellites. These materials used in aircraft structures including primary and secondary structures such as the fuselage and wings has increased fairly regular. Moreover, there has been an increasing demand for composites in both the military and civilian aircraft industry. At least 50% of the next generation of military and civil aircraft structures are likely to be made from composites as described in the (Nayak, 2014), (Roeseler et al., 2007).

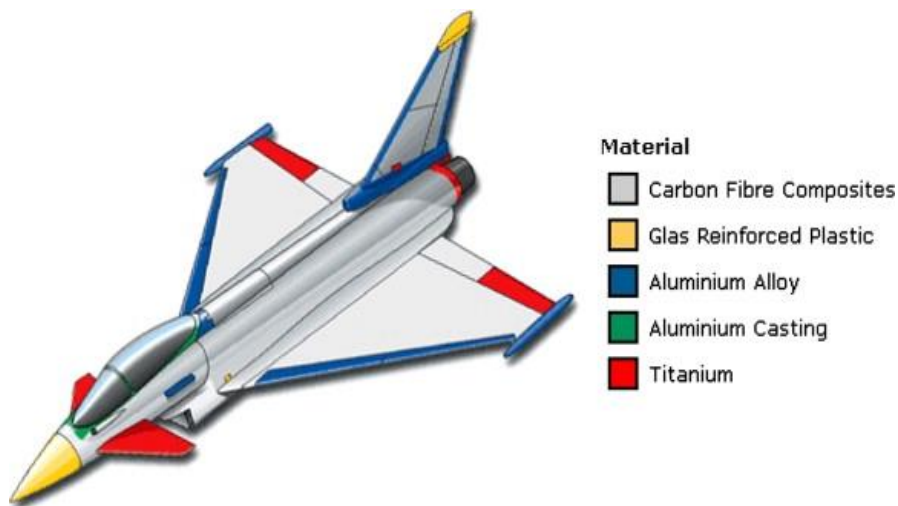
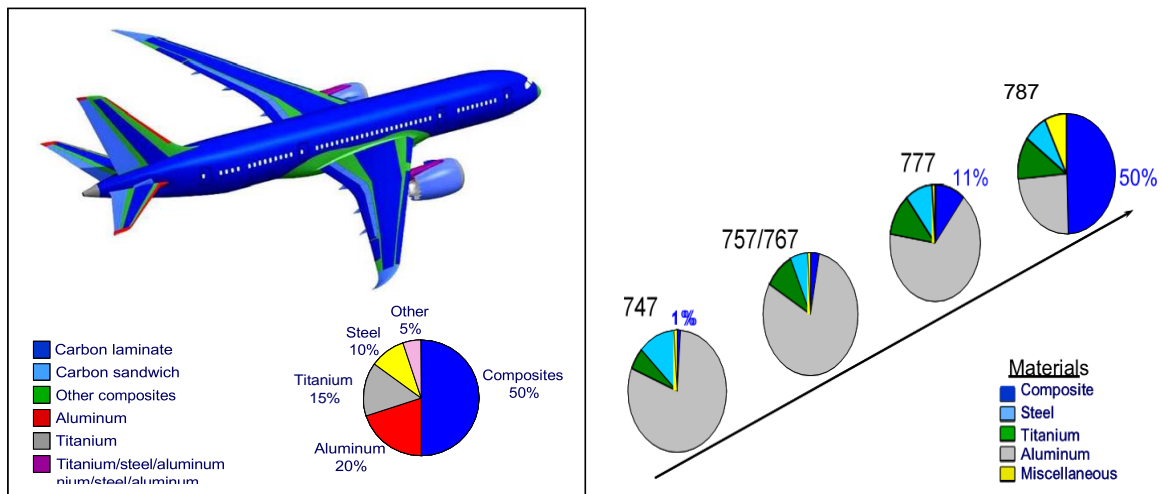


**Figure 1. 2 Eurofighter – Material selection (Dilger et al., 2009).**

The Australian Transport Safety Bureau (2007) lists the percentage of composites in different types of aircraft: Eurocopter (NH90) has approximately 85% of its structural weight built from composite materials, and the Eurofighter has approximately 40%, as shown in Figure 1.1. Aircraft structures usually contain one or more of the following composite materials: Carbon Fibre Reinforced Plastic (CFRP), Kevlar/epoxy, and glass fibre such as Eurofighter as shown in Figure 1.2



1.

**Figure 1. 3 Percentage of composite material of Boeing aircraft structural weight (Roeseler et al., 2007).**

(Baker et al., 2004), presented the 20% of F-18 fighter aircraft structure contain composites materials. (Nayak, 2014) highlighted the benefits of use the composite material in aerospace applications and the 50 % of Boeing 787 airplane manufacture from composites material. (Roeseler et al., 2007) presented the composite material started with military aircraft such as the AV-8B, B-2, F-18, Euro-fighter, and AH-66 and expanded to civilian airplane such as Boeing commercial aircraft. The Figure 1.3 illustrated the percentage of composite material of Boeing aircraft structural weight.

The total weight of composite materials on the 747 aircraft was about 1% and the 757 and 767 aircraft was approximately 3%. With additional introduction of composite material on structure the composite structural weight on 777 increase to 11%. The most progressive on composite structures today are the 787 was about 50% of the total aircraft structural weight. (Dorworth et al., 2009) presented the reasons of used the composite materials in aircraft such as minimised production costs, high strength-to-weight and stiffness-to-weight ratios; aerodynamic smoothness; resistance to fatigue and corrosion; and ease of repair and maintenance. These materials can also be easily moulded into complex curved shapes necessary for use on aircraft.

Composite materials have a few disadvantages such as the stiffness and strength properties that can be vary with impact, for example low resistance for impact damage. Impact can lead to damage in composite structures including matrix cracking, fibre failure, and delamination. Different types of damage can lead to significant strength reduction in composite materials. Therefore, from these facts many research questions raised such as:

- What the percentage of the aircraft structure strength can be restored after impact damage?
- How can proved the optimum repair joint with limited time and resource by using numerical method?

### **1.3 Survivability**

In the last three decades, the aircraft industry has developed technology that will increase aircraft survivability for both military and civil aircraft. Ball (1985) defines survivability as “the capability of an aircraft to avoid and/or withstand a man-made hostile environment.” Survivability is increased by addressing both aircraft susceptibility and vulnerability.

Aircraft susceptibility is defined as the capability of an aircraft to avoid different types of hostile (threat) environments. The environment can be man-made, for example, an enemy's air defences, or natural, such as lightning or crashes. An aircraft's susceptibility can be measured by the probability the aircraft is hit while on a mission:  $P_H$  (Ball et al., 1995). Low susceptibility is achieved by using susceptibility reduction concepts, such as electronic countermeasures equipment (noise jamming and deceiving) or threat suppression (eliminating/ degrading the enemy's air defence).

Vulnerability is the inability of an aircraft to withstand the hostile environment. An aircraft's vulnerability can be measured by the conditional probability of the aircraft's being hit:  $P_{K/H}$  (Ball et al., 1995). Low vulnerability is achieved by using vulnerability reduction technology, such as component redundancy (maintaining two engines) or active damage suppression (installing a fire detection and extinguishing system).

The survivability of an aircraft can be measured by the probability of survival,  $P_s$ , which depends on the aircraft's susceptibility and vulnerability. It can be expressed in the equation below:

$$P_s = 1 - P_H P_{K/H} \quad 1.1$$

Thus, survivability is increased when susceptibility and vulnerability are reduced. Indeed, there are many different ways to enhance an aircraft's survivability: one aspect of survivability is the ability to quickly repair damage in a minimum period. During operations and exercise, the repair time is a sensitive issue because the aircraft has to be operational ready within a short period. When any damage cannot be quickly repaired, the aircraft may not return to service quickly enough for other operational requirements and becomes a 'grounded' aircraft. Thus, the design of an aircraft should allow for quick damage repair, supporting survivability. This is not because doing so increases the survivability of an aircraft, but because it improves force survivability. With respect to increasing survivability, composite materials present the best opportunity for mechanics to use to quickly repair damage as compared with other materials.



## 1.4 Aims and Objectives of Study

The main aims of the study as follows:

- The use of composites laminates for the application in aircraft components was the motivation for the study.
- Investigate on compression after impact performance on repair and unrepaired composite at two thicknesses and various impact velocity on the composite laminates subjected to high velocity impact.
- Only the testing can be prohibitively expensive due to the large number of specimens needed to verify every geometry. Loading, environment and failure mode. Therefore, developments of reliable analysis tools/model to assess and the prediction high velocity impact response and CAI are very important in order to assess and improve the reliability of composite structure for use in aircraft.

In order to achieve the overall aims, the objectives are outlined as follows:

- Provide further understanding of the behaviour of CFRPs subject to high velocity impact by using experimental and numerical method. The change of kinetic energy and damage formulation were used to compare the simulation results with the related experimental results.
- Provide finite element models that can predict the nonlinear mechanical behaviour of repaired CFRPs composites under compression load.
- Establish a numerical methodology to defined the optimum repair joint to restore sufficient strength of damaged aircraft composite structures during some operations and exercise activities with limited resources
- Predict the non-linear mechanical response of repaired CFRP composites under compression load.

- Utilise the design of experiments method to the conducting numerical analysis to optimise the strength and compression failure load of a repaired composite laminate.

## **1.5 Proposed Contributions to Knowledge**

The main contributions to knowledge in the study is Establish a numerical methodology to defined the optimum repair joint to restore sufficient strength of damaged aircraft composite structures during some operations and exercise activities with limited resources.

## **1.6 Thesis Layout**

This thesis has divided into six chapters.

Chapter 1: introduction. The first chapter included the polymer composite materials are common in a variety of applications and have been used in the aerospace industry for the last thirty years. The composite have many advantages and some disadvantage such as minimised production costs, high strength-to-weight and stiffness-to-weight ratios; aerodynamic smoothness. It also includes the research questions, aims and objective of the study and the contributions to knowledge of the study.

Chapter 2: Literature review. The second chapter presented the previous studies in the numerical modelling and Finite Element Analyses (LS-DYNA) of composite laminate subject to high velocity impact; Repair composite laminate, which focuses on stepped lap joint and compression after impact.

Chapter 3: Experimental studies. The third chapter presents the design of the Gas Gun test device, used to determine failure characteristics, e.g., residual velocities, and the size of damage for CFRP composite laminate. Compression after impact test used to determine the compressive failure load for undamaged, damaged and repaired composite laminate to define the optimum stepped lap joints. The parameters affected in the study were step length, step height, layup

angel, and avoidance levels in adhesive material. These experiments have been used to validate a finite-element model.

Chapter 4: Numerical methodology. The fourth chapter describes the numerical methodology used to model CFRP laminates subject to high velocity impact and model stepped lap joint to repair CFRP composite laminate under compression load. This chapter provides a background of the main functions used in LS-DYNA explicit finite element code, and then compares different types of composite advance material modelled within LS-DYNA. It also details a number of failure criteria used in LS-DYNA (material model 059) to model impact damage behaviour of CFRP composite structure. The material parameters of projectile and composite laminate have been definite to modelling both of them. The author has also created a quasi-static numerical simulation for single element and a simplified composite laminate to better understand the behaviour of composite material when the failure occurs. Lastly, a numerical impact simulation for different types of composite laminates is performed. Moreover, a numerical compression after impact simulation for undamaged, damaged and repaired two types of composite laminate used to defend the optimum stepped lap joint.

Chapter 5: Result and Discussions. The fifth chapter provide the discussion of the result of impact damage experiments and numerical simulation of CFRP composite laminates subject to high velocity impact and the result of compression after impact experiments and numerical simulation of unrepaired CFRP composite laminate included damaged (impact damage) and undamaged. Also discuss the optimum joint to repair the damaged (impact damage) CFRP composite laminate.

Chapter 6: Conclusion and future. The sixth chapter summarises the contributions to the knowledge covered in this thesis, and includes the conclusion of this study and suggestions for future work.

# **Chapter 2**

# **Literature Review**

## **2.1 background and context**

The use of composite materials in modern military and civil aircraft structures is a continuous increase. At least 50% of the next generation of military and civil aircraft structures are likely to be made from composite materials as presented by (Nayak, 2014), (Roeseler et al., 2007) and (Australian Transport Safety Bureau, 2007). Composite materials are used in aircraft because they offer good properties, such as high strength to weight ratio, low capacity to absorb kinetic energy and easy of repair. However, they have low resistance to impact damage caused by threats such as dropped tools or runway debris and this damage can lead to significant strength reductions which affects the aircraft survivability. However, this study has accounted an assessment of the ability of a damaged structure to be repaired quickly as parts of aircraft survivability assessment.

## **2.2 Impact Damage**

Composite materials in aircraft are very susceptible to impact damage caused by projectiles, such as dropping a tool during maintenance, bird strikes, debris impact, bullets, or foreign object damage (FOD). Damages such as these are the main cause of strength reduction in composite material.

Williams et al. (1995) investigated the percentage decrease of the compressive strength reduction in this material and found it to be about 70%. Therefore, to recover the compressive strength reduction in a damaged aircraft structure, need to be understanding the damage mechanisms, behaviour of the damaged material, possess the ability to make estimations of residual strengths and repairs of damage.

There are many parameters effects on types of damages such as location of damage, type of material, and components. Some damage effects for various components are listed in Table 2.1.

**Table 2.1 Some Damage Effects for Various Components (Australian Transport Safety Bureau, 2007)**

COMPONENTS	DAMAGE EFFECT
Structure	Loss of load carrying ability
Aerodynamic surfaces	Failure to perform aerodynamic function
Mechanical components	Crack, jamming
Engine components	Engine failure, fuel leakage and fire
Fluid or pressure containers	Leakage, hydraulic ram damage, engine ingestion, fire and explosion
Avionics components	Loss of signal or function, fire and explosion
Propellants and explosives	Fire and explosion
Crew members	Loss of ability to function

The damage is a complicated phenomenon due to a range of physical effects that can take place simultaneously. The following parameters have a significant influence on an impact event: impact velocity, projectile properties, material properties of the target, target geometry, and boundary condition, among others. Much research exists on the damage mechanisms and behaviour of laminated composite materials that have been subject to impacts.

The behaviour of composite structures under impact loading is one of the major concerns in aerospace industry (Abrate, 2007). (Olsson et. al., 2000) found that impact response is dependent on the projectiles' velocities. (Cantwell et.al., 1989) presented low and high velocity impact tests to investigate the initiation and development of damage in a number of CFRP laminates. (Zukas, 1989) published a book (High Velocity Impact Dynamics) dealing with experimental, analytical, and numerical aspects of the behaviour of materials subjected to high velocity impact.

(Abrate,1998; Silva, 1999; Choi et. al., 1991b; Choi et. al., 1991a; Choi et. al., 1992) studied the damage mechanisms and behaviour of laminated composite materials that have been subject to impacts.

(Fujii et. al., 2002) performed several kinds of CFRP laminate specimens, which were subjected to impact damage by a steel sphere having the range of the velocities between 500–1230m/s. (Tanabe et. al., 2003) analysed the effects of interfacial strength and properties on the fracture behaviour of the CFRPs and used the energy absorption measurement and the size, shape, and structure observation to defend these effects. (Hammond et. al., 2004) studied high velocity fibre impact on CFRPs with extensive work to measure in-plane and out-of-plane deformation of the sample during impact, residual velocity of the projectile, as well as microscopic and macroscopic damage. From above literature review of the behaviour of CFRPs subject to high velocity impact was understood.

### **2.3 Classification of Impacts**

There are many ways to classify impact behaviour, including boundary-controlled, wave-controlled, impact velocity. However, projectile velocity is the most widely cited categorisation used in the literature, with impacts categorised into hypervelocity impact, high-velocity impact and low-velocity impact. Olsson (2000) found that impact response is dependent on the projectiles' velocities. Hypervelocity (ballistic) impact involves projectiles moving at extremely high velocities, i.e., exceeding the speed of sound; the Hyper velocity impact response is shown in Figure 2.1(a).

The impact response shown in Figure 2.1(b) is related to high-velocity impacts. These types of impact usually are characterised by a small projectile mass (runway debris) and short contact duration. The loading induces a localised form where most of the energy is dissipated over a very small zone instant to the point of impact. The high velocity impact was focus on this study, with a projectile velocity of (100-500 m/s).

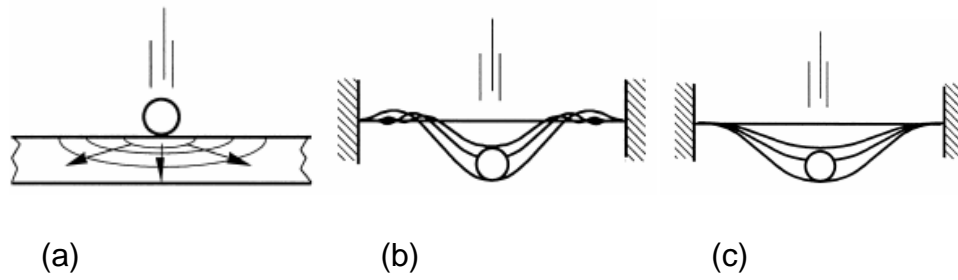


**Figure 2. 1 (a) Hypervelocity impact; (b) High-velocity impact; and (c) Low-velocity impact (Olsson, 2000)**

In low-velocity impacts, the projectile usually has a large mass (dropped tool on composite structure), and the contact duration between the target and projectile is much longer than the time it takes for the waves to reach the structure boundaries. Therefore, the deflection and load will have similar relations in a static loading such that the resulting response will be quasi-static. The impact response on this velocity is bending, as shown in Figure 2.1(c).

Cantwell et al. (1989) used optical micrographs and ultrasonic C-scans to examine the low- and high-velocity impact responses of a number of (CFRP). The main impact response under low-velocity impact of a more flexible structure was bending; the high-velocity impact response is governed by flexure and shear waves, as shown in Figure 2.2.

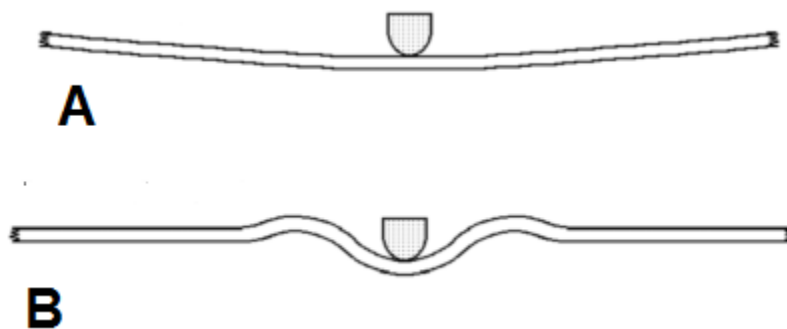


**Figure 2. 2 Schematic Representation of the Impact Response Under (a) Low-velocity Impact and (b) High-velocity Impact (Cantwell et al., 1989).**



## 2.4 Failure Mechanisms

Impact energy is absorbed through various fracture processes, including matrix cracking, delamination, shear plugging and fibre failure. These types of damage mechanisms for impact loading have been investigated in a variety of studies (Cantwell et. al., 1985; Cantwell et. al., 1990; Cantwell et. al., 1991; Choi et. al., 1992). Fibre failure in tension, shear, and compression are both the most important and the simplest failure mechanisms to identify and quantify. In the case of tension, failure occurs due to the growth of fibre cracks within plies, while with compression, the failure occurs due to micro buckling and the formation of kink bands.

CFRP composite materials present various failure mechanisms according to their complex structures. Properties of CFRP play the main role in creating the failure and damage mechanisms. There are many parameters affected by these properties; for example, the geometry of the target (size, orientation and shape), its matrix and mode of reinforcement, together with projectile parameters such as size, shape, velocity, and impact angle. Therefore, for the purposes of evaluation, the composite material is considered as a structure rather than as a material.

Under low velocity impact loading, the structural geometry determines the target's impact response; however, geometrical parameters such as the width and length of the target appear to have very little effect on the impact response when the CFRP is under conditions of high velocity impact loading. When modelling high velocity impact, damage behaviours need to be investigated for different types of failure modes. Woodward (1990) has demonstrated various failure mechanisms for targets subject to impact, as shown in Figure 2.3.

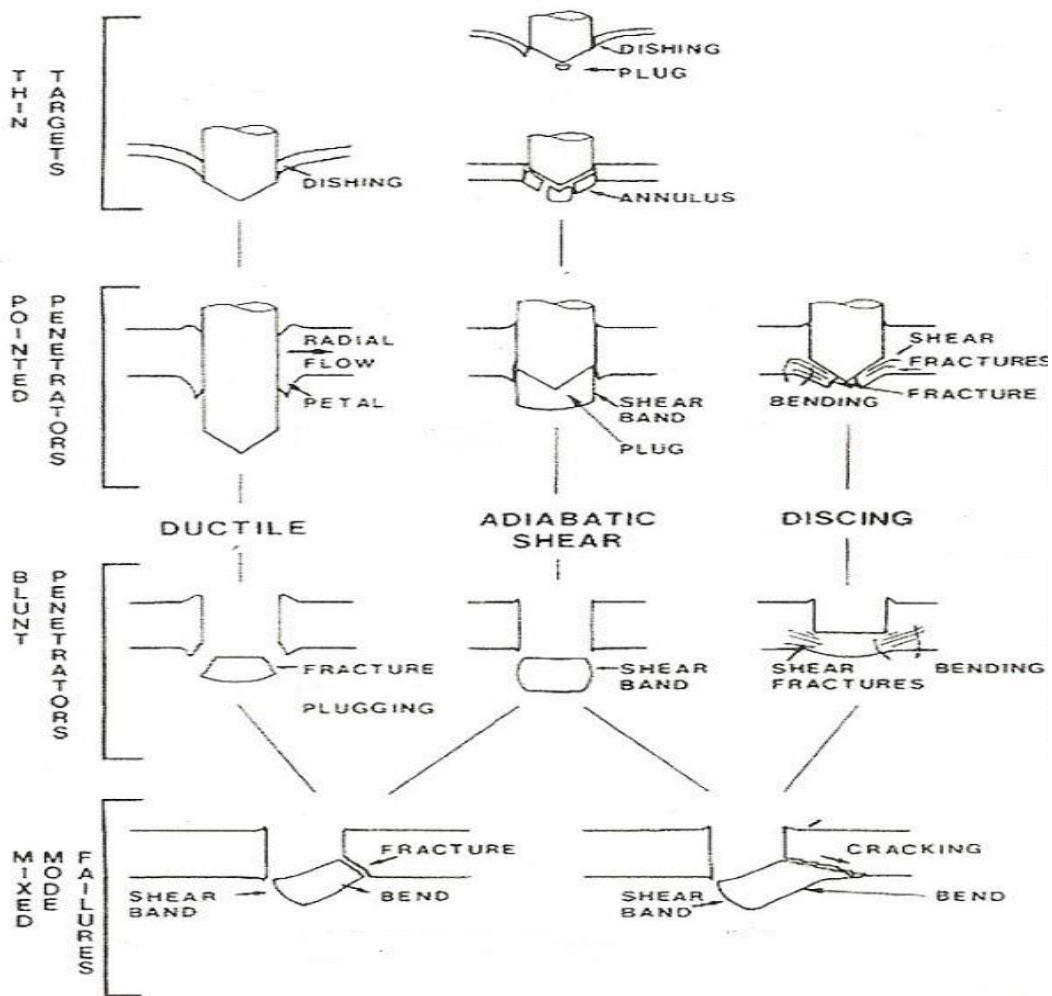
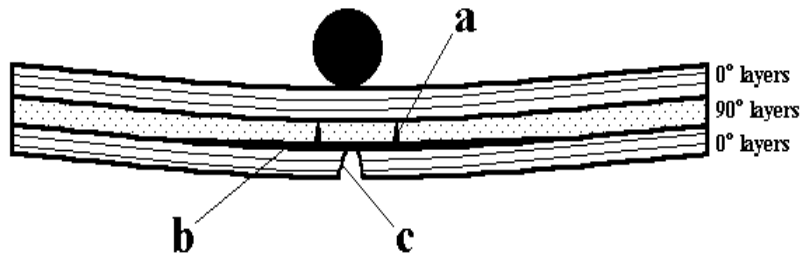


Figure 2. 3 Categorisation of failure modes (Woodward 1990).

(Cantwell et. al., 1985) have presented a schematic of the three principal damage mechanisms for impact: a) matrix cracking; b) delamination; and c) fibre failure, as shown in Figure 2.4. Low impact velocities produce high tensile stresses in the lowest ply. These tensile stresses produce matrix cracks that are deflected at the laminate interface to form a delamination.



**Figure 2. 4 Schematic demonstrating the three principal damage mechanisms for impact: a) matrix cracking, b) delamination, c) fibre failure. (Cantwell et. al., 1985).**

The damage process is initiated by matrix cracks, followed by delamination. In thick laminates, the matrix cracks begin in the first layer impacted by the projectile, because damage from the high, localised contact stresses progresses from the top, resulting in a pain tree pattern Figure 2.5(a). For thin laminates, bending stress in the rear side of the laminates introduces matrix cracking in the lowest layer, which again starts a pattern of matrix cracks and delamination and leads to a reversed pain tree pattern, as shown in Figure 2.5(b)

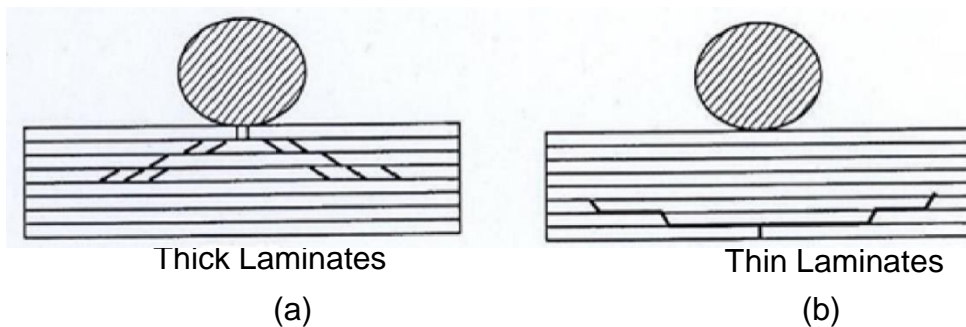


**Figure 2. 5 Schematic representations of damage patterns: (a) pin tree and (b) reversed pain tree (Abrate, 1998).**

Abrate (1998) has reviewed the shear plug failure mode during penetration, noting that failure occurs due to the high stresses created at the point of impact: the element near the impacted side is sheared and pushed forward, causing a hole or “plug”, and the rear surface of the laminate starts to penetrate, as shown in Figure 2.6. Following this, failure occurs by tensile fibre fracture, and delamination occurs near the exit.

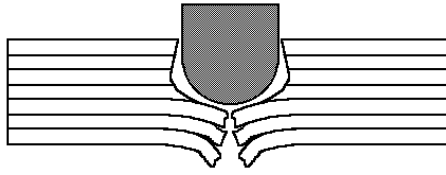


**Figure 2. 6 Shear plug failure mechanism (Abrate, 1998).**

Abrate (1998) describes this hole as being shaped as a truncated cone; the overall size of its front face is equal to the size of the projectile, and increases as it penetrates the composite with a  $45^\circ$  half angle, as shown in Figure 2.7. The fibre failure becomes critical when cracks propagate in the direction normal to the fibres, completing the separation of the laminate.

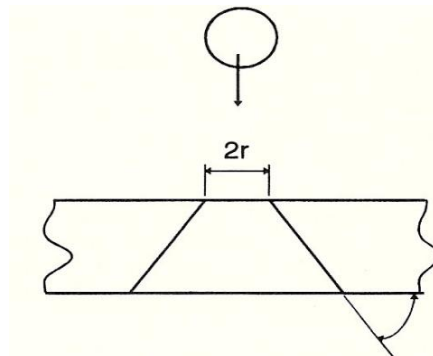


**Figure 2. 7 Fibre failure mode (Abrate, 1998).**

Failure modelling of composite materials under impact loading by the finite element method (FEM) has been the subject of numerous studies. (Bland et. al., 2001) performed a wide set of experiments with projectiles impacting CFRP composite, and analysed different types of failures. (Abrate, 1991; Abrate, 1994) comprehensively reviewed the ballistic impact of laminated composite materials. Detailed penetration process and damage progressions were simulated with graphite/epoxy laminates impacted by a steel projectile and compared with the experimental results (Chen et. al., 1997).

## 2.5 Numerical Simulation of Composite Laminates under High-Velocity Impact

The finite-element method (FEM) is a powerful numerical tool for the analysis of composite structures subjected to impact by a projectile. Zukas (1990) identifies the description of the material deformation and failure behaviour as a major determining factor in modelling the high velocity impact of composite laminates.

### 2.5.1 Impact Model

Abrate (1998, 2001) has presented various types of numerical models used in the analysis of the behaviour of composite structures subject to impact, such as the Spring Mass Model, Energy Balance Model and Complete Model.

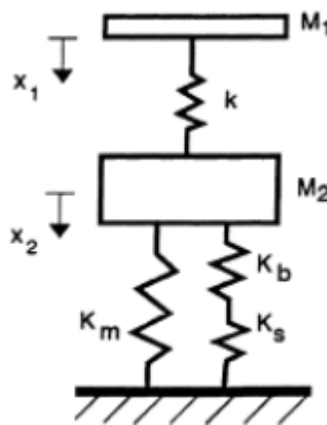


Figure 2. 8 Spring-mass Model (Abrate, 1998).

The spring-mass model is the most suitable way to model some types of impact, particularly when the size of specimens is small, yet this method is more complex than the energy balance model. The spring-mass model predicts the complete force history. As shown in Figure 2.8,  $M_1$  and  $M_2$  represent the projectile and target mass, respectively. The two springs  $K_s$  and  $K_b$  represent the linear stiffness of structure, and the second spring ( $K_m$ ) represents the nonlinear membrane stiffness. This model has two degree of freedom; however, when the initial condition is applied, the model can be simplified to a single degree of freedom.

The energy balance model considers the balance of energy in the system. This balance of energy is based on a comparison of the impactor's kinetic energy to the sum of the energy resulting from contact, deformation, bending and penetration of the structure. In cases of low velocity impact, when the composite plate does not penetrate, quasi-static behaviour applies on this structure. Therefore, all of the projectile's initial kinetic energy has been used to deform the structure, and when the deflection reaches maximum value, the velocity of projectile becomes zero. However, in cases of high velocity impact the velocity of the projectile, or impactor, will not become zero. Therefore, the balance of energy will include the residual energy of the projectile after it has penetrated the plate. This model accurately predicts the maximum impact force.

The high velocity impact of a projectile on aircraft structures of composite materials has been investigated based on experimental techniques and numerical simulation (Sun et. al., 1996; Lopez et. al., 2002; Lopez et. al., 2003; Hosur et. al., 2004; Lopez et. al., 2007; Garcia-Castillo et. al., 2009; Varas et. al., 2013; Cantwell et. al., 1986; Abrate et. al., 2001) to understand and improve the impact response of composite materials and structures. (Aambur et. al., 2001) presented a comparison of LS-DYNA numerical simulations and experimental results for a complete penetration test of the thin plates by small fragment impactors.

(Chan et. al., 2007) presented an experimental programme and a computational model in LS-DYNA to determine the ballistic limits of CFRP laminates in various stacking sequences. (López-Puente et. al., 2008) used a finite element numerical model for carbon/epoxy composite to predict both residual velocity and damaged area when subjected to high impact velocity. (Varas et al., 2013) analysed the high velocity impact of steel cylinders on thin carbon/epoxy woven laminates. The inter-lamina failure prediction was achieved by means of the use of cohesive elements.

(Pernas-Sánchez et. al., 2014) predicted the behaviour of unidirectional composite plates when impacted at high velocity by a steel sphere projectile. The residual velocity in case of penetration and the damaged area in the laminate were the variables chosen to validate the results obtained in their proposed numerical methodology. (Muslim et. al., 2016) presented a numerical investigation of penetration and perforation behaviour of FRP composite plates under impact. (Xin and Wen, 2015) studied the impact behaviour of composite plate by experimental impact test and results were validated with theoretical model in terms of ballistic limit and residual velocity.

## **2.6 Repair Composite laminate**

As mentioned earlier, composite materials are vulnerable to damage due to impact loading, such as from runway debris, tool drops, or ballistics. The impact damage can reduce the mechanical properties including compressive strength and levels of load failure of laminated composite structures. Therefore, aerospace industries have been seeking ways to restore sufficient strength to the damaged composite structures to ensure continued safe operation.

Depending on the level of damage, a decision has to be made to replace the parts or repair them. However, when users have limited resources or time, replacing the damaged item is not the best solution. In such a situation, repairing the damage is the most suitable solution. There are two types of aircraft repair: field (temporary) repair and depot (permanent) repair. The field repair is usually undertaken when the operational limitations are severe, and include limitations on resources, the environment, and time. For example, during some operations and exercise activities, there are limitations on use of portable tools, materials, and time, mainly in that repairs must be completed within a specific time limit (typically within two hours). Therefore, this type of repair has been used in this study due to the need to simulate reality.

For decades, designers used bolted (mechanical) joints to repair aerospace structures. However, the development of bond technologies has led to bonded patches becoming more structurally efficient, which minimises damage to the

structure (Ratwani, 1979; Rose, 1981; Baker, 1993). Bonded repairs to aircraft structures offer many advantages compared with a mechanical repair method. Advantages include minimal shape change, extra uniform stress distributions, no significant weight increase, and a reduction in maintenance costs (Matthews, 1982). In the past, bonded repairs were regularly applied to secondary structures, but now the designer introduces this technology in primary structures.

Aerospace industries have been seeking ways to restore sufficient strength to the damaged composite structures to ensure continued safe operation by repair the damage. There are many parameters that affect engineering decisions concerning which type of repair used, such as aerodynamics, residual strength, the strength restoration requirement and time. Therefore, a wide variety of bond patches have been designed over the years. Examples include the overlap joint, the scarf, and the stepped-lap which is presented by (Gunnion et al. 2006), as shown in Figure 2.9 (Gunnion et. al., 2006). (Megueni et. al., 1997) found that strength restoration up to 80% of the ultimate allowable amount is sufficient for most repair geometries by change the joints geometric.

Several studies have been published regarding composite repairs and the development of bond technologies which have led to bonded patches becoming more structurally efficient, which minimises damage to the structure which some of these studies were conducted on repaired aircraft structures (Baker. 1997; Megueni, 2008; Campilho et. al. 2009). It is important to increase repair effectiveness, which further increases the residual strength of the repaired structures. Several techniques, such as geometric changes of the joints, are useful in achieving this objective.



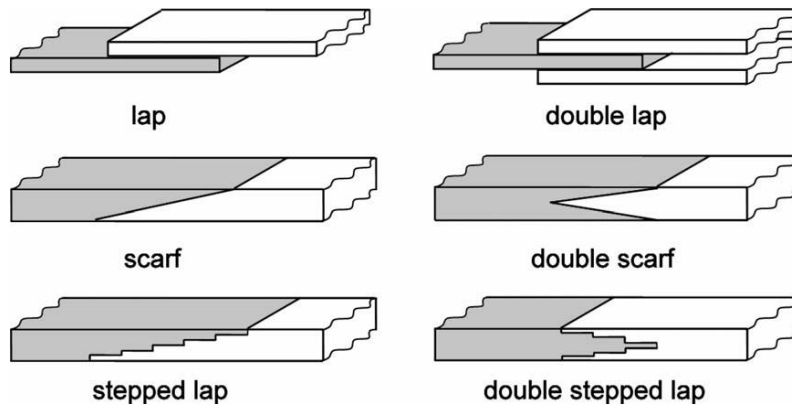


**Figure 2. 9 Common Bonded Joints (Gunnion et al., 2006).**

### 2.6.1 Repair Geometries

The effectiveness of the composite adhesive joint of composite structures is mainly dependent on joint type used and the property of adhesive (Matthews, 1982). (Gunnion and Herszberg, 2006) present many examples of joint geometries including the overlap, scarf, and stepped-lap joints.

The failure load and strength of joints depends on the joint geometry and the mechanical properties of adherends and adhesives. These factors affect the stress distribution - a combination of normal and shear stress - within the joint. The stress display at the overlapping ends of the adhesive layers may negatively affect the strength of the joint. Therefore, a geometry joint design is used to strengthen the joints.

Single and double-lap repairs are easily executable and cost little. However, a full-strength recovery is not usually possible with these types of repairs. When structures are highly stressed, these types of joint repairs are not advisable. Scarf and stepped-lap repairs are the preferred methods of repair when there is a requirement for high-strength recovery or a flush surface is needed to satisfy the aerodynamic requirements of a damaged composite aircraft structure.

An optimally designed scarf or stepped-lap joint is significantly stronger than an optimum lap joint and high failure-load capacity; compare with other lap joint, as illustrated in Figure 2.10 (Hart- Smith, 1986). However, designing an optimum

scarf repair for composite structures is complex due to the large number of material and geometric parameters that influence the joint performance.

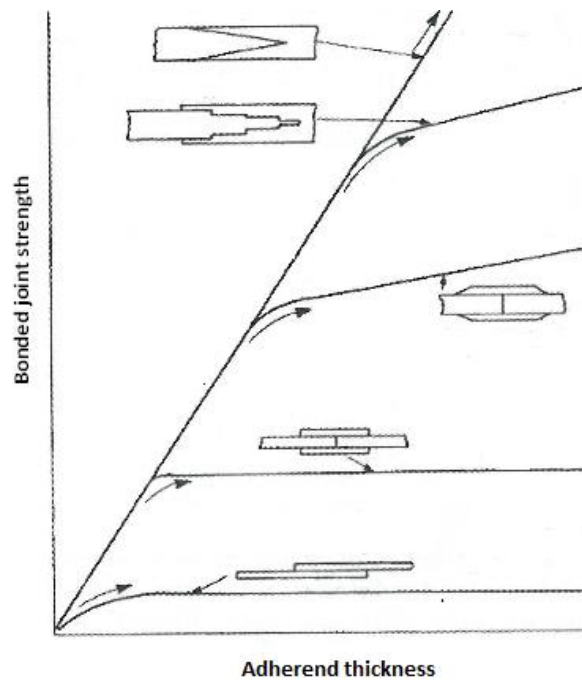


**Figure 2. 10 Joint type versus bond joint strength (Hart-Smith, 1986).**

The stepped joint consists of more than one single lap joint, whereas the scarf joint is more than one stepped joint (Matthews et al.,1982; Kim et al. 1995; Lchikawa, 2008; Sawa, 2010 ). This design allows the stepped lap joint to share similar joining efficiencies and mechanical properties with scarf joints, such as levels of joint strength and fatigue characteristics. In addition to the positives concerning the design, the stepped joint is easier to manufacture than the scarf joint, and uses a simple tooling system without the weighty manufacturing cost.

Stepped-lap repairs are the preferred methods of repair when there is a requirement for high-strength recovery or a flush surface is needed to satisfy the aerodynamic requirements of a damaged composite aircraft structure. There are different studies investigating the effect of adhesively bonded stepped-lap joints on the strength of joint (Kimiaeifar et. al. 2013; Kim et. al. 1995; Li D et. al., 2011; Kim, 1995). (Ichikawa et. al, 2008) studied the behaviour of a stepped-lap joint subject to tensile loading by experimental and numerical finite analysis. This

study presented the edge of the adhesive which contains the highest value of the maximum principal stress.

In the latest study, (Salih, 2014) presented the behaviours of single lap joint, one step lap joint and three step lap joint by using experimental and numerical methods. It was observed that the three-step lap produces the lowest stress concentration at the edges of the bond line compared with one-step lap and single lap joint. (Hart-Smith, 1973) performed an analytical models to investigate stepped-lap and scarf joints which considered adherend stiffness. (Bendmra et al. 2015) studied the effect of joint parameters on stresses in stepped-lap and scarf repairs. In their work numerical models of stepped-lap and scarf joints compared the stresses for different joint configurations such as overlap lap length, stacking sequence and overlap layup.

The compressive failure loads is a critical concern in the design of repaired composite structure because the greatest reduction in after impact loading is observed in compression. (Abrate, 1998; Cantwell et al., 1986; Prichard et al., 1990) presented the maximum percentage of strength reduction in damaged composite laminate is up to 40% to 60% of an undamaged composite laminate. Compression after Impact (CAI) tests are widely used in the industry to assess residual strength and failure load performance of different composite combined by various fibre and matrix (Bendemra et al., 2015; Sanchez-Saez et al., 2005; Williams et al., 2009; Prichard et al., 1990). Therefore, The CAI tests has been performed to assess the optimal design of repaired composite laminates by comparing the residual strength and failure load.

Therefore, this study will discuss the best experimental design needed to create the optimal stepped-lap joint, which can maximise the compressive failure load and strength for repaired CFRP composite laminate.

# **Chapter 3**

# **Experimental Studies**

### 3.1 Introduction

The experimental method used to validate the numerical methodology to find the optimum joint to repaired damaged composite laminates. Therefore, the damaged laminates were produced from high velocity impact tests used to performed the compression after impact test and used the results to validate the compression after impact model, then extend this model to modelling the optimum joint to repaired damaged laminates.

The first step, the study used the Hizell experimental results (Hizell, 2008) to validated the numerical modelling by determine the failure characteristics, e.g. residual velocities and the size of damage which is detailed the result in chapter 4. However, to obtain more accurate results to validate the simulation results, a high velocity impact test rig was designed. The architecture and operational principle behind the gas gun dictated that the utilisation of a modular design approach. The modular design in (Cranfiel University lap, 2011) gives the gas gun the advantage of allowing easy repair, replacement, trouble -shooting or change of components without affecting other parts of the product. The gas gun test rig was designed employing a process of problem definition, team assembly, concept development, final concept review, prototype development and testing.



Figure 3. 1 Gas Gun Test Rig (Cranfiel University lap, 2011).

## 3.2 Gas Gun Test Rig

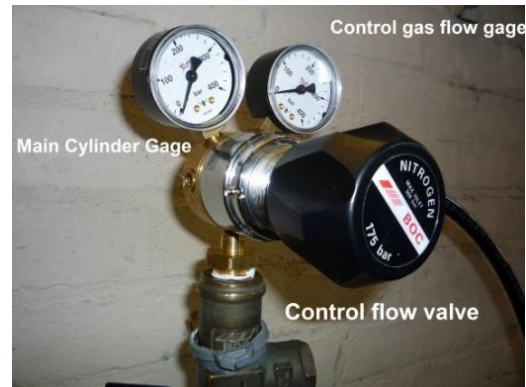
The gas gun test rig, shown in Figure 3.1, utilises a variety of systems, including the gas system, gun system, support system and the velocity measurement system. The gas gun test rig was designed employing a process of problem definition, team assembly, concept development, final concept review, prototype development and testing.

### 3.2.1 Gas System

The gas system has been used as a single stage pressure system, which includes the main cylinder, gage and valves, as shown in Figure 3.2 (a).



(a)



(b)

**Figure 3. 2 Gas system: (a) Main Gas Cylinder; (b) Gages and Control flow valve.**

The main cylinder is used to contain the gas (Figure 3.2(a)). Different types of gases can be used for this kind of test, such as helium and nitrogen. For this study, nitrogen was chosen because it is relatively safe to handle, it is highly compressible (produces high energy during expansion), it is inflammable, and it is an inert gas that does not react to material. The criteria used to decide the capacity of the cylinder were the number of tests required per cylinder and the capacity of the pressure reservoir.

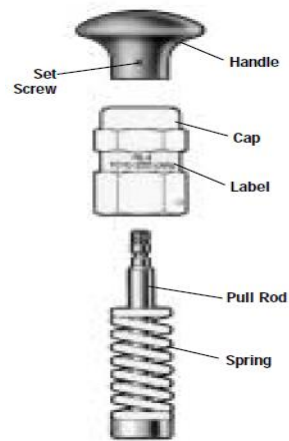
There are two gauges used in the gas system (Figure 3.2(b)): a cylinder pressure gauge to read the pressure in the cylinder and a control gas flow gauge to read

the output pressure from cylinder, which controls the level of pressure used to launch the projectile. The pressure gauge's specification was 40 MPa as maximum pressure.

There are three type of valves used in this system, including a main switch valve used to cut off the gas flow when the experimental complete, and a control flow valve used to control the gas flow rate that depends on the required velocity (Figure 3.2(b)). The specification of this valve is 17.5 MPa as maximum outlet pressure. Thirdly, the low pressure relief valve (Figure 3.3) is used to prevent overpressure and to maintain the pressure value in the chamber. The maximum pressure in this valve was 5MPa.



(a)



(b)

**Figure 3. 3 Low Pressure Relief Valve: (a) valve during experimental phase; (b) disassembled layout.**

The gas system is connected to the gun system by a 3m long hose. The gun system contains many parts, such as gauge, valves, chamber and barrel.

### 3.2.2 Gun System

The main function of the Gun system is to release the pressure to launch the projectile at the required velocity both efficiently and safely. In order to achieve

this objective, several components are needed: gauge; valves; chamber; barrel; gas release device; separate sabot; sabot and impact chamber box.

### 3.2.3 Chamber Gauge

The objective of using the chamber gauge in gun systems (Figure 3.4) is to account for the pressure used to launch the projectile at a certain velocity. Therefore, the reading pressure in this gauge is the pressure in the chamber. The gauge specification is 5.5 MPa as maximum pressure.

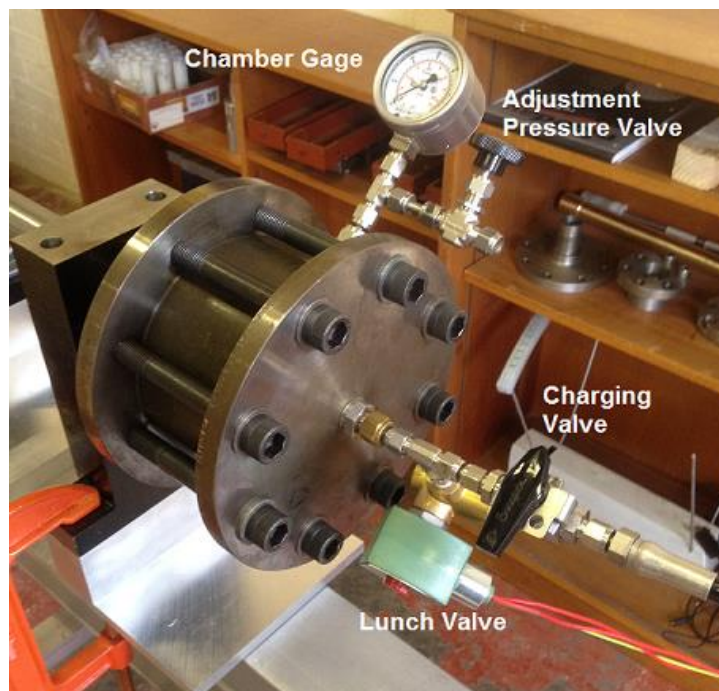


Figure 3. 4 Gauge and Valves in gun system.

#### 3.2.3.1 Valves

There are three types of valves in this system (Figure 3.4). The first valve (charging valve) rotates the plunger/diaphragm open or closed, which increases the pressure in the chamber. The second valve (adjustment pressure valve) opens (if needed) to decrease the pressure in chamber, and should be closed before opening the first valve. When the pressure in the chamber reaches the targeted level, the third valve (lunch valve) opens to launch the projectile.



### 3.2.3.2 Reservoir (chamber)

The reservoir (chamber) is a metallic device made in the form of a cylinder, with a maximum pressure of 5 MPa and a capacity of  $9.4 \times 10^{-4} \text{ m}^3$ . This device was designed to make the sabot and O-ring easily replaceable to prevent pressure leaks (Figure 3.5(b)). Other specifications include a reservoir volume of  $9.4 \times 10^{-4} \text{ m}^3$ , an equivalent reservoir diameter of 0.1355 m and an equivalent reservoir length of 0.06534 m.

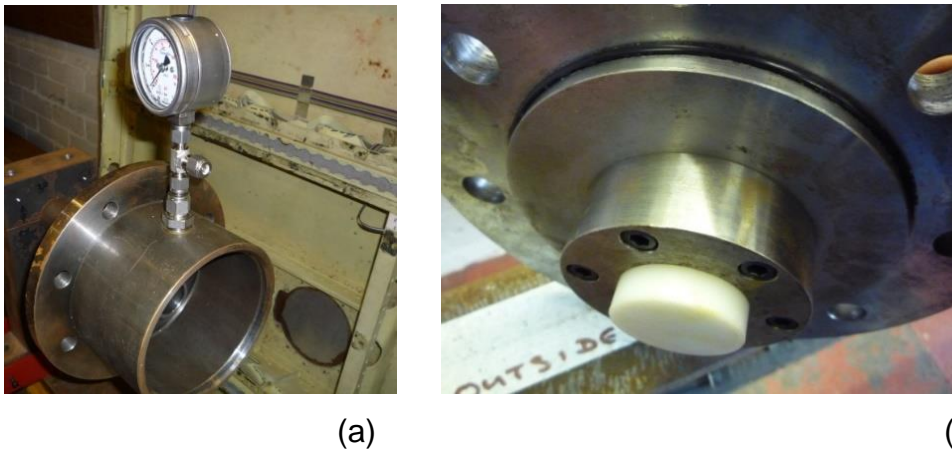
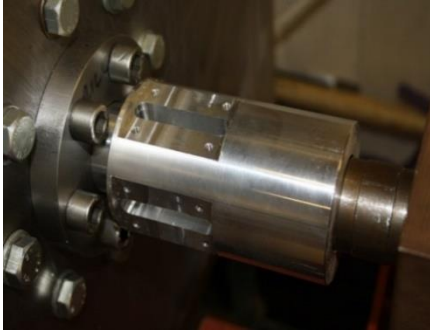


**Figure 3. 5 The gun system reservoir (chamber): (a) cylinder with sabot; (b) cylinder cover with O ring.**

### 3.2.3.3 Barrel

The barrel consists of one meter of piping that the projectile will come across. The inner diameter for the barrel measures 0.032m and its outer diameter is 0.035 m. The barrel commands the accurate acceleration of the projectile before it becomes airborne. One function of the barrel is to ensure that the projectile impacts on the laminate exactly. As shown in Figure 3.6(b), the barrel has a length of 1m and an inner diameter equal to 0.032m. The major specifications of the barrel should not be affected by high pressure, temperature and projectile friction.



(a)



(b)

**Figure 3. 6 Gun system devices: (a) gas release device; (b) barrel device.**

#### **3.2.3.4 Gas release device**

A major problem discovered during the design phase and first trial test concerned the sabot fragments, which are produced when the sabot hits the separate (stopping) sabot devices, when, due to the second stage of pressure (after launching the sabot), fragments flow the projectile. The gas release device was introduced to eliminate this problem. This device has four slots with an inner diameter equal to 0.032m (Figure 3.6(a)), which are used to reduce the pressure in the second stage. This design has not solved the problem completely, however. Therefore, this problem will be subject to future work.

#### **3.2.4 Impact chamber box**

The impact chamber box is an important component of a gas gun test because it hosts the major devices used in this test, such as the sabot stopping device, velocity measurement devices and projectile host device (Figure 3.7). One of the most important functions of the impact chamber is to make the environmental work safe by hosting the projectile after launch and during impact. Therefore, the box was made from thick iron metal and designed to include a host velocity measurement device. The projectile host device is used to hold the projectile after impact, and uses material such as a piece of cloth or paper to reduce the speed of the projectile.

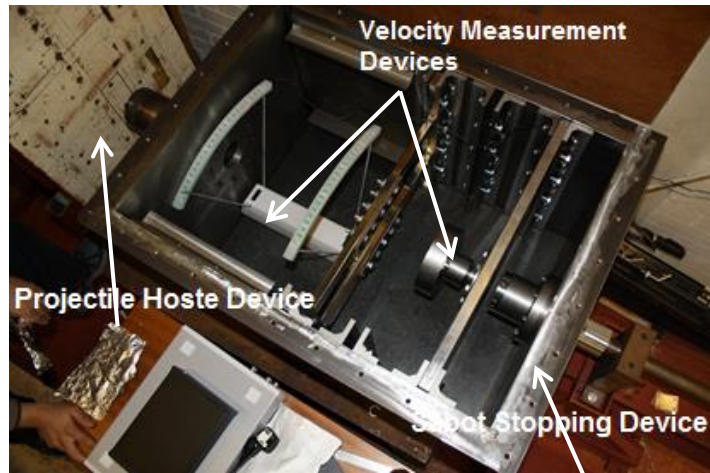


Figure 3. 7 Impact chamber box

### 3.2.4.1 Sabot Stopping Device

The sabot stopping device is a stopping mechanism for the sabot at the end of the gas gun (Figure 3.8). The projectile is adhered to the sabot, and therefore loses adhesion once the sabot is stopped and the projectile is pushed forward. This design produced fragments from sabot. To reduce these fragments, the sabot stopping device will later be redesigned to incorporate a cone separator mechanism.

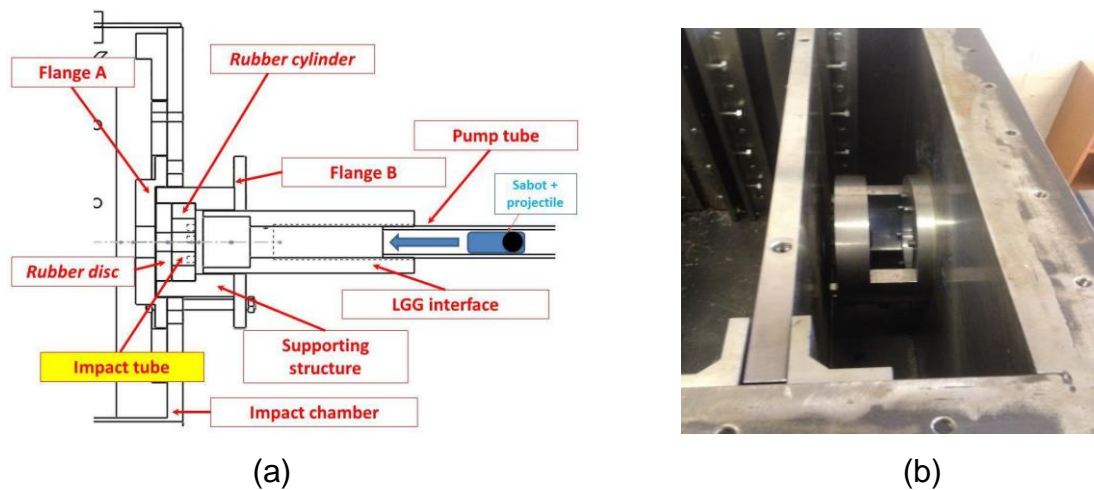
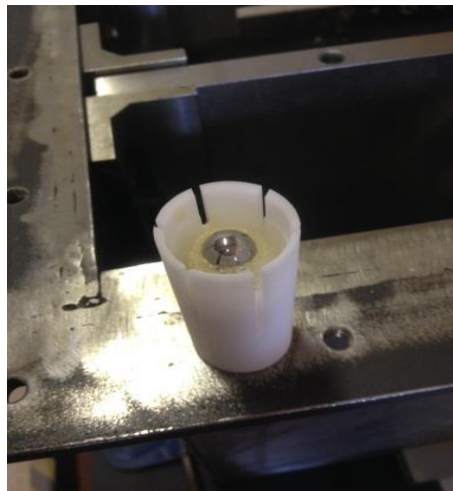


Figure 3. 8 Sabot stopping device in the gun system: (a) Schematic illustration; (b) overview of the device.

### 3.2.5 Sabot

A sabot is designed to carry the projectile until it reaches the sabot stopping device, at which point the projectile pushes forward. Together, the sabot and projectile constitute the launch package (Figure 3.9). The geometric specifications of this package (sabot + projectile) include a length of 0.04 m, a diameter of 0.031m, and a mass of 57 g.



**Figure 3. 9 Sabot with spherical stainless steel projectile.**

### 3.2.6 Velocity Measurement Systems

Velocity measurement devices measure a projectile speed at the barrel exit. Various methods had been developed to measure the velocity, including ProChrono Digital Chronograph and Optoelectronic devices.

#### 3.2.6.1 ProChrono Digital Chronograph Device

The ProChrono Digital Chronograph device operates on the principle of measuring the time it takes for a projectile travel from the first sensor to the second sensor, then dividing this time by the fixed distance between the two sensors. These sensors are mounted internally in the case and gather light through the two rectangular openings at the top of the case.



(a)



(b)

**Figure 3. 10 Sabot with spherical stainless steel projectile.**

When a projectile travels through the two rectangular openings, the light will be blocked. This change in light intensity is detected by the sensor, and then converted to a signal. The chronograph device measures the projectile's travel time between the two sensors. It then converts this time into velocity and displays it on front LCD screen (Figure 3.10).

The ProChrono Digital Chronograph device specifications include a velocity range of 7-2100 m/s, a temperature range of 0-37 degrees Celsius, dimensions of 0.4 x 0.1 x 0.025 meters, with the minimum time between shots of 250 – 500 msec and an accuracy of  $\pm 1\%$  measured velocity.

### **3.2.6.2 Optoelectronic device**

Optoelectronic devices are electronic components that produce and detect optical energy (Figure 3.11(a)). A detector is a photodiode sensor that detects the optical energy, and a light-producing diode (LED) is a producer. In Figure 3.11(b), the two holes contain the producer (light-producing diode (LED)). The minimum response time is 1 nanosecond; however, increasing the response time will increase the device's accuracy for measuring projectile velocity. Measuring the projectile velocity using this concept is calculated by using the equation (3.1).

$$V = \frac{D}{t}; \quad (3.1)$$

where  $V$  represents the projectile velocity,  $D$  is the distance between hole (a) and hole (b) (Figure 3.11(b)), and  $t$  denotes the time it takes for the projectile to pass through the two holes.



**Figure 3. 11 Optoelectronic device: (a) overview; (b) two holes containing light-producing diode (LED).**

Optical energy from the light-producing diode (LED) passes across the path of the projectile, and this energy is then received onto a photodiode sensor (Figure 3.11(a)). The detector produces a voltage relative to the amount of light received by the detector.

As the projectile intercepts the Optical energy, it shadows the detector, causing a jump in voltage, which is recorded on the HAMEG (HM8123) for both sensors. By checking the front laminate of the HAMEG (HM8123), the time it takes the projectile to travel between the two sensors can be easily determined. Since the distance between these sensors is known, the projectile velocity can be calculated by using the above equation.

### **3.2.6.3 HAMEG (HM8123) specifications:**

- Measurement range: 0Hz - 3GHz.

- 2 measurement inputs DC 200MHz.
  - Input A/B: Input impedance 1M $\Omega$ /50 $\Omega$  (switchable), sensitivity 25mVrms
  - Input C: Input impedance 50 $\Omega$ , sensitivity 30mVrms
- 400MHz time base with 0.5ppm stability.
- 9-digit resolution at 1 second gate time.
- 9 measurement functions, external gate and arming.
- Input for external time base (10MHz).
- Display modes: numeric, histograms or trend plots.
- Standard: TCXO (temperature stability:  $\pm 0.5 \times 10^{-6}$ ).

As described in the above section, the gas gun test rig has many systems as a gas system and a gun system. However, to achieve the objective of this study, the design processes two activities: firstly, projectile velocity calibration; and secondly, alignment of the projectile path.

#### **3.2.6.4 Projectile Velocity Calibration**

The projectile velocity is dependent on the gas pressure in the system. Therefore, pressure analysis was applied to estimate the theoretical projectile velocities. The thermodynamic and ideal gas laws were used to complete this analysis.

In order to calculate the projectile velocities, some assumptions were applied: the amount of barrel friction is negligible; there is no air resistance inside the barrel (vacuum); the energy is conserved - all the energy released by the gas is transmitted into the projectile; and isothermal and adiabatic conditions occur in the system.

The first law of thermodynamics relates the heat ( $dQ$ ) added to the system to the work ( $dw$ ) done by a system and the change in internal energy ( $du$ ):

$$dQ = du + dw; \tag{3.2}$$

By definition, in an adiabatic process, the heat exchanged is expressed as  $dQ = 0$ . Substituting this in the first law and rearranging gives:

$$du = -dw; \quad (3.3)$$

$$dw = Pdv; \quad (3.4)$$

where  $dw$  is the work done by change in pressure ( $P$ ) and volume ( $dv$ ):

$$c_v = \frac{du}{dT} * \frac{1}{n}; \quad (3.5)$$

$$du = nc_v dT; \quad (3.6)$$

where  $c_v$  is the specific heat, and defined as the heat added ( $du$ ) per unit temperature ( $dT$ ) change per the number of moles ( $n$ ).

Substituting Equations (3.4) and (3.6) in Equation (3.3) yields:

$$nc_v dT = -Pdv; \quad (3.7)$$

The equation of an ideal gas is:

$$PV = nRT; \quad (3.8)$$

where  $R$  is the gas constant, derivatives Equation (4.8) become

$$PdV + VdP = nRdT; \quad (3.9)$$

$$dT = \frac{PdV + VdP}{nR}; \quad (3.10)$$

Substituting Equation (3.10) in Equation (3.7) yields:

$$c_v \frac{PdV + VdP}{R} = -Pdv; \quad (3.11)$$

$$c_v(PdV + VdP) = -RPdv; \quad (3.12)$$

$$c_v PdV + RPdv + c_v VdP = 0; \quad (3.13)$$

$$\frac{(c_v + R)}{c_v} PdV + VdP = 0; \quad (3.14)$$



Dividing equation (3.14) by  $P$  and  $V$  obtains this )result:

$$\left(\frac{c_v+R}{c_v}\right)\frac{dv}{V} + \frac{dP}{P} = 0 ; \quad (3.15)$$

When the gas is ideal and the pressure is constant, then Specific heat is expressed as  $c_p = c_v + R$ .

The ratio of specific heats is expressed as  $\gamma = \frac{c_p}{c_v}$

$$\gamma\frac{dv}{V} + \frac{dP}{P} = 0 ; \quad (3.16)$$

$$\gamma d(\ln V) + d(\ln P) = 0 ; \quad (3.17)$$

$$d(\ln PV^\gamma) = 0 ; \quad (3.18)$$

Therefore, for an adiabatic process in an ideal gas:

$$PV^\gamma = constant ; \quad (3.19)$$

When the gas expands under constant volume, the heat raises the internal energy and completes the work. For nitrogen,  $\gamma$  is about 1.4.

The gas gun principle included two stages. At the first stage, the volume comprises chamber (reservoir) volume ( $V_c$ ) and the pressure is a measure of chamber (reservoir) pressure ( $P_c$ ), while at the second stage, the volume includes total volume (chamber and barrel) ( $V_T$ ), and pressure is an expression of total pressure (chamber and barrel) ( $P_T$ ).

According to the Gas Gun principle and adiabatic process:

$$P_c V_c^\gamma = P_T V_T^\gamma ; \quad (3.20)$$

$$P_T = P_c \left(\frac{V_c}{V_T}\right)^\gamma ; \quad (3.21)$$

The work done by gas at Stage Two. Substituting equation 3.21 in Eq.3.4:

$$dw = P_c \left(\frac{V_c}{V_T}\right)^\gamma dv ; \quad (3.22)$$

$$dw = P_c V_c^\gamma V_T^{-\gamma} dv ; \quad (3.23)$$

Integrating the following:

$$w = P_c V_c^\gamma \int_{V_c}^{V_T} V_T^{-\gamma} dv ; \quad (3.24)$$

$$w = \frac{P_c V_c^\gamma}{(1-\gamma)} (V_T^{(1-\gamma)} - V_c^{(1-\gamma)}) ; \quad (3.25)$$

When the energy balance is applied, the work done by gas equals the kinetic energy ( $KE_p$ ) of the projectile, and then:

$$w = KE_p = \frac{1}{2} m_p V_p^2 ; \quad (3.26)$$

where  $m_p$  is projectile mass and  $V_p$  is projectile velocity.

$$w = \frac{1}{2} m_p V_p^2 = \frac{P_c V_c^\gamma}{(1-\gamma)} (V_T^{(1-\gamma)} - V_c^{(1-\gamma)}) ; \quad (3.27)$$

$$V_p = \sqrt{\frac{2P_c V_c^\gamma}{m_p(1-\gamma)} (V_T^{(1-\gamma)} - V_c^{(1-\gamma)})} ; \quad (3.28)$$

The velocity calibration method was processed by comparing the theoretical method and the experimental method. The theoretical projectile velocity was calculated by using Equation 3.28. This equation included many parameters related to gas, projectile, chamber and barrel (Table 3.1).

**Table 3. 1 Geometric parameters for projectile, chamber and barrel.**

Parameters	Value
Projectile mass ( $m_p$ )	0.057 (kg)
Chamber volume ( $V_c$ )	0.001124 (m <sup>3</sup> )
Total (chamber and barrel) volume ( $V_T$ )	0.0018787(m <sup>3</sup> )
Specific heat ( $\gamma$ )	1.4
Chamber pressure ( $P_c$ )	10*10 <sup>5</sup> -100* 10 <sup>5</sup> (Pa)

The gas gun test has limited pressure capacity. Therefore, the pressure used to calculate the velocity project was specified from 0.05 MPa to 5 MPa. Table 3.2 charts the theoretical projectile velocity, showing how the velocity increases gradually as the pressure increases.

**Table 3. 2 *Theoretical projectile velocity.***

Pressure (Bar)	Pressure (MPa)	Velocity (m/s)
0.5	0.05	30.26
1.0	0.1	42.80
2.0	0.2	60.52
3.0	0.3	74.12
4.0	0.4	85.59
5.0	0.5	95.69
6.0	0.6	104.83
7.0	0.7	113.23
8.0	0.8	121.04
9.0	0.9	128.39
10.0	1	135.33
15.0	1.5	165.75
20.0	2	191.39
25.0	2.5	213.98
30.0	3	234.40
35.0	3.5	253.18
40.0	4	270.66
46.0	4.6	290.00
50.0	5	302.61

The experimental method used the ProChrono Digital Chronograph device to measure projectile velocity. Due to availability and capability, two pressure data were used to calibrate the pressure system and velocity device.

**Table 3. 3 Compression between theoretical projectile velocity and experimental projectile velocity**

Pressure (MPa)	Theoretical Velocity (m/s)	Average Theoretical Velocity	Chronograph Velocity (m/s)	Average Chronograph Velocity	Average % error
4	270	270	190	191	30
4	270		182		
4	270		200		
4.6	290	290	195	203	30
4.6	290		200		
4.6	290		210		
4.6	290		207		

Table 3.3 and Figure 3.12 show the theoretical velocity as exceeding actual velocity (estimated velocity) by 30%, a difference due to many factors, such as losses (leaks) in the system, projectile fractional, and the use of a manual rather than electric mechanism for the release valve.

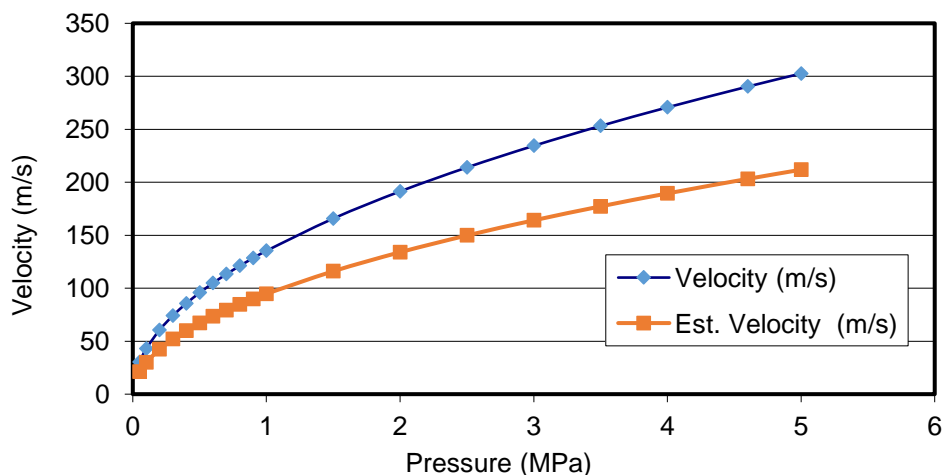


**Figure 3. 12 Theoretical projectile velocity and chamber pressure.**

Due to the specifications of available gas gun tests, this difference must be considered as a factor when calculating the input projectile velocity. For this study, the author calculated the input velocity by use the theoretical projectile velocity as described before instead of measuring it with the Optoelectronic device because the latter has problems with accuracy.

### 3.2.7 Support System

One of the main parts of a gas gun test is the support system. The objectives of the support frame design used in this study were to carry the impact load, be lightweight, and to be able to adjust and change the specimen with ease. The impact load transfers to the support frame when the projectile impacts the laminate. Therefore, to determine the best design for the support frame, one must calculate the impact load at maximum velocity. The maximum theoretical velocity in the gas gun system was 500 m/s at 5MPa. The impact load was calculated from the follow equation:

$$F = P * A; \quad (3.29)$$

Where F denotes the impact load, A is specimen area and P is pressure applied on specimen.

The support specifications include:

- A specimen size equal to 0.0225 m<sup>2</sup>.
- Pressure applied on the specimen equalling 5MPa.
- An impact load (F) of 5000000\*0.0225 = 112.5 kN.
- An estimated factor of safety of 3.
- An impact load of 337.5 kN.
- Required support frame dimensions: 0.63 x 0.5 x 0.02 m.

To apply these objectives and specification requirements to the support frame design, it was decided to use stainless steel and square tubing. The final design is shown in Figure 3.13:



**Figure 3. 13 Support frame with composite laminate in gun system.**

### **3.2.8 Gas Gun Test Alignment**

One of the major activities in gas gun practices is to align the barrel with the specimen in order to centralise the projectile in the centre of specimen. There are two methods used to align the gas gun, including the laser pointer device and the Leica Jogger 20 Automatic Level device.

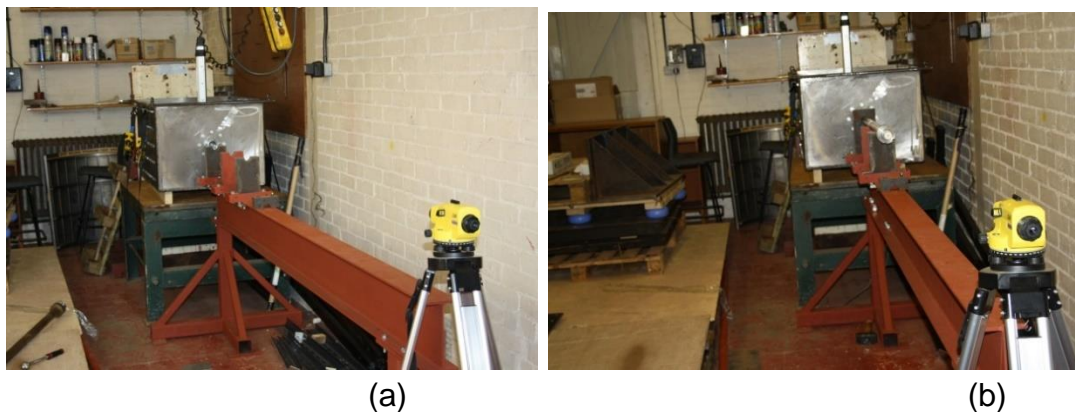


**Figure 3. 14 Aligning the barrel with the specimen: (a) adjustment with the position of the centre of the impact chamber; (b) adjusting the position of the barrel.**

The Leica Jogger 20 Automatic Level device has been used as the first step to complete the alignment process. In this step, the best level for the device is determined, then the device is adjusted with the position of the centre of the impact chamber by using a scalar (Figure 3.14(a)). The barrel is fitted onto the impact chamber, then the device is used to adjust the position of the barrel by changing its level (Figure 3.14 (b)).

The second step used the laser pointer device to adjust the centre of the composite laminate in the path of the projectile. To achieve this level of adjustment, the level of support frame was changed accordingly (Figure 3.15).



**Figure 3. 15 Adjusting the centre of composite laminate in the path of projectile.**

### **3.3 Experimental Procedure**

This study tested the response of two different thicknesses of woven CFRP laminates subjected to high velocity impact. The projectile range velocity used in the experiment between 100 m/s and 500 m/s. As noted, the first objective of this project was to better understand the behaviour of the woven CFRP laminates when subjected to high velocity impact. The second objective was assessing the energy transferred to the laminate when the composite laminate was completely penetrated by measuring the residual velocity and the impact velocity of the projectile.

### 3.3.1 Experiment Materials

The high velocity impact tests were conducted using a high-pressure (nitrogen) gas gun, as described in previous section. The first step of this process was the selection of the material, which was the woven composite laminate made of Hexcel G0926 Carbon Fabric 5 harness 6K, Areal Weight 370 gsm. The resin used was Hexcel RTM 6, cured for 1 hour 40 minutes at 180° C at a pressure of 100 psi, with an average thickness of 0.375mm.

As described previously, the first laminate was comprised of 11 layers, using the following stacking sequence: 0/90; ± 45; 0/90; ± 45; 0/90; ±45; 0/90; ± 45; 0/90; ±45; 0/90. The second pane had 7 layers, using the following stacking sequence: ± 45; 0/90; 0/90; ±45; 0/90; 0/90; ±45. The density of woven CFRP laminates was  $1.512\text{e-}3 \pm 1\text{e-}6 \text{ g/mm}^3$  (Hazell al et, 2008), using a Micrometrics Accupyc 1330 gas Pycnometer.

The dimensions of the specimens measured 100×150 mm with 4.125mm in thickness and 100×150 mm with a thickness of 2.625mm, respectively. The composite specimen was secured into the support frame by clamping the top and bottom edges and leaving the side edges free (Figure 3.16).

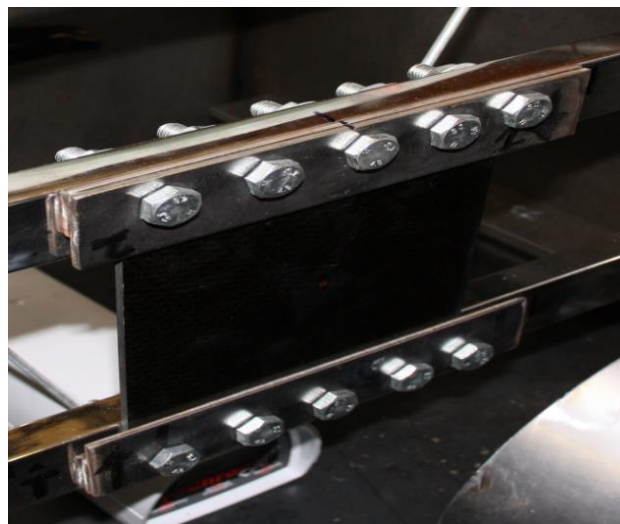


**Figure 3. 16 Boundary conditions of the support frame.**



The projectile used was spherical ( $11.97\text{mm} \pm 0.01\text{mm}$ ), with a mass of  $7.165\text{ g} \pm 1\text{e-}3\text{ g}$ , and it was constructed from a fully annealed stainless steel (SS304) with an ultimate tensile strength of 675 MPa and a yield strength of 450 MPa. Using this kind of hard material allows a better understanding of the mechanics of energy absorption by damage in the CFRP composite, since a sphere does not deform plastically, but only decreases the initial energy by slowing its velocity.

### **3.3.2 Impact Testing**

The projectile was fired from a single-stage gas gun: once the gas is released, it provides the force needed to accelerate a projectile, which then impacts onto the CFRP target to produce impact damage. To create this damage, the following test procedure needs to be completed:

- Read the main cylinder gauge, then open the main switch valve and open control flow valve. During gas refill, the reservoir (chamber) needs to be monitored so the control flow gauge does not exceed the limitations of the low pressure relief valve (5MPa).
- Open charge the valve in the chamber and close the launch valve and adjustment pressure valve, then monitor the chamber gauge. When the chamber pressure reaches the specific pressure, for example, 4.6 MPa, close the charging valve.
- Before starting the previous steps, one needs to prepare the velocity measurement devices (ProChrono Digital Chronograph and Optoelectronic devices) by following the procedures described in the previous section.
- The composite laminate and support frame are adjusted in the same path of projectile by using a laser pointer device as described in the alignment section.
- When all steps are completed and safety concerns are taken in account, use the launch valve to release the sabot, then the sabot crosses through the

barrel. When the sabot impacts the sabot stripper, the projectile releases and impacts the laminate.

- Record the velocity displayed on the ProChrono Digital Chronograph and Optoelectronic devices.

The range of velocities to consider includes 100 to 500 m/s according to the capability of the gas gun test. The change of projectile kinetic energy is used to assess the energy transferred to the composite laminate. Therefore, the energy transferred to the composite laminate is calculated by using residual velocity and the impact velocity. Then the transfer energy is calculated using:

$$E_T = E_i - E_R ; \quad (3.30)$$

Where ( $E_T$ ) is the transfer energy, ( $E_i$ ) is the impact energy and ( $E_R$ ) is the residual energy.

The impact energy ( $E_i$ ) was calculated using:

$$E_i = \frac{1}{2} m_p v_i^2 ; \quad (3.31)$$

Where  $m_p$  is the mass of the projectile and  $v_i$  is the impact velocity. The residual energy ( $E_R$ ) was calculated using:

$$E_R = \frac{1}{2} m_p v_R^2 ; \quad (3.32)$$

where,  $v_R$  is the Residual Velocity.

Substituting Equations 3.30 and 3.31 in Equation 4.29 yields:

$$E_T = \frac{1}{2} m_p v_i^2 - \frac{1}{2} m_p v_R^2 ; \quad (3.33)$$

### 3.4 Experimental Results and Validation

The transfer of projectile kinetic energy to target CFRP composite laminates is dependent on the thickness of the target. Figure 3.17 presents a comparison between two woven CFRP composite laminates of two different thicknesses

(4.125mm and 2.625mm) with different layering (11 layers and 7 layers) in both experimental and simulation methods.

The residual kinetic energy for both methods used in this study showed a slight difference of about 5 % between simulation and experimental results for the 7 layer versus the 11 layer laminates, as shown in Figure 3.17. This difference in the residual kinetic energy of the projectile is due to two possible reasons: the frictional energy of eroding elements surrounding the projectile during penetration was neglected; and/or the mesh size may not be refined enough for the penetration.

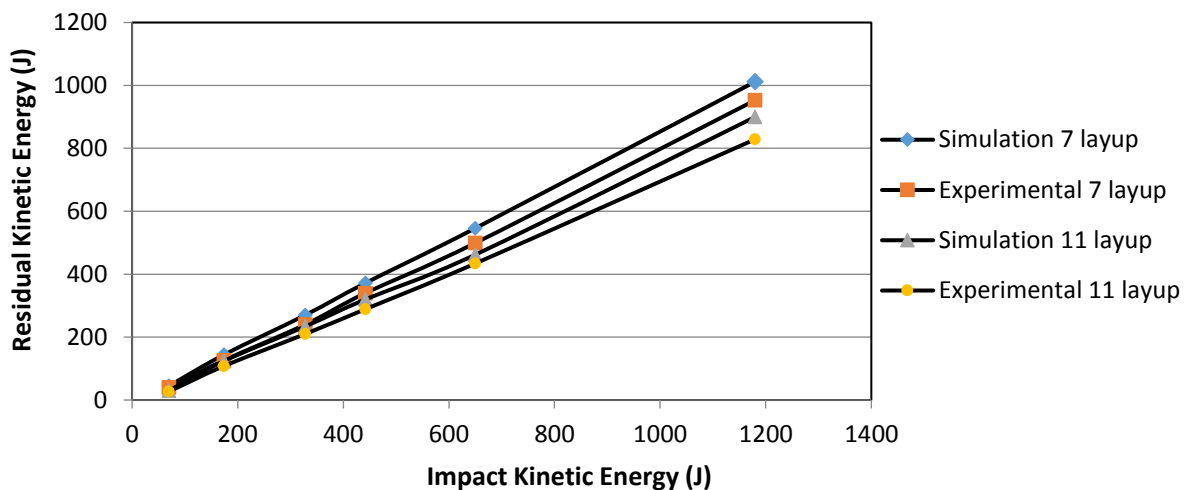
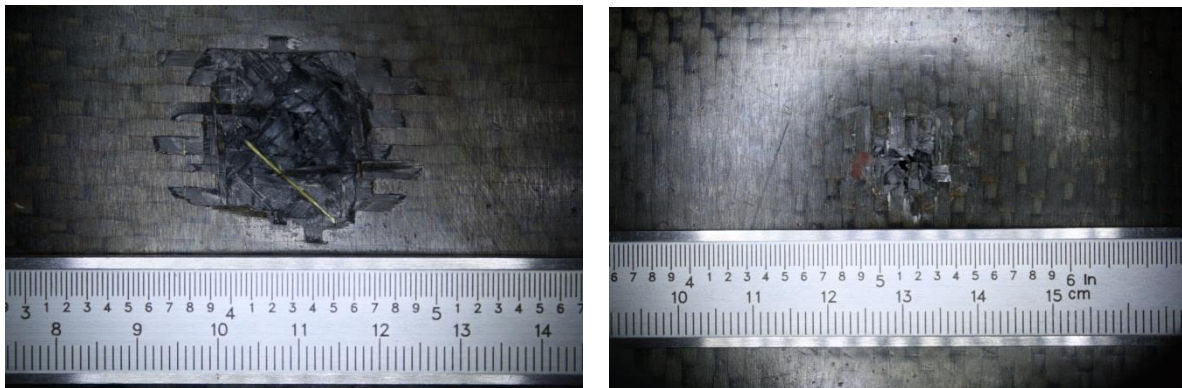


**Figure 3. 17 The residual kinetic energy of the projectile against the initial impact kinetic energy for two different thickness composite laminates: 2.625mm (7layers) and 4.125 mm (11 layers). (140m/s to 479m/s).**

This comparison shows the residual kinetic energy for the 7 layered CFRP composite laminate as higher than other laminate (11 layers), which is in line with expectations. The difference indicates that the 11 layered CFRP composite laminate provided better penetration resistance than the thinner, 7 layered laminate. This behaviour of CFRP composite laminates under high velocity impact shows the effect of the thickness of laminates on residual kinetic energy. The residual kinetic energy of a projectile increases with increasing initial impact

energy, which means the kinetic energy is absorbed by an increase in composite laminate layers (Lopez-Puente et al., 2008) .

Figures 3.18(a) and 3.18(b) show the failure behaviour of the 11 layered CFRP composite laminate subject to impact velocity 200 m/s by the steel sphere projectile. Figure 3.18(a) shows a damaged area with a diameter of about 24mm on the rear surface of the laminate. Figure 3.18(b) shows the front surface of the damaged laminate, where the diameter of the damaged area measures about 15 mm. These figures clearly show that the damaged area changed significantly with the projectile velocity through the composite laminate, with the damaged area on the front being smaller than the damaged area at the rear surface (Hazell, et. al., 2008), where a petalling or plug formation was apparent.



(a)

(b)

**Figure 3. 18 Impact failure of 11 layered CFRP woven composit laminate impacted at 141 J (200 m/s): (a) rear surface (b) front surface.**

The relationship between the penetration mechanism and projectile velocity has been discussed in previous studies, and is further clarified in this study. When the projectile velocity was less than 200 m/s, the failure (penetration) mechanism exhibited petalling (Figure 3.19), and when the velocity exceeded 200 m/s, the failure mechanism appeared as a plug formation.



**Figure 3. 19 Petalling formation failure of 11 layered CFRP woven compost laminate impacted at 141 J (200 m/s).**

Figure 3.20 presents a micrograph of the impact failure of the 7 layered CFRP woven compost laminate impacted at 141 J (200 m/s). The Figure 3.20 shows the plies relaxing and closing up after impact by a steel sphere projectile. The tensile and compressive failure in petalling formation can be easily observed.



**Figure 3. 20 Micrograph of impact failure of 7 layered CFRP woven compost laminate impacted at 141 J (200 m/s).**

On impact, different types of failure were exhibited, such as delamination and fibre breakage. The petalling failure was created by the following process: the projectile pushed the plies, then the plies relaxed, thus nearly closing up the penetration hole. During the impact event, some fragments were produced as part of plug formation.

The simulation results from this and the previous chapter were validated by using the experimental results for three different types of CFRP woven composite laminates: 7 layered; 11 layered and 16 layered. The results show the simulation programme can be utilised in the next step, which is to simulate the repaired (damaged) CFRP woven composite laminate and then applying compression after the impact test for undamaged, damaged and repaired CFRP woven composite laminates.

### **3.5 Compression after Impact**

The compression after impact (CAI) test (experimentally) used to determine the compressive failure load for damaged and non-damaged composite laminate and used to validate and assess the simulation results. The predicted of numerical undamaged failure load occurs at 150 KN for 11 plies specimens and 7 plies specimens is 80 KN as described in section 5.3. Therefore, compression after impact tests of the composite laminate were carried out on a hydraulic 250 KN INSTRON 8500 test rig as seen in Figure 3.21.



**Figure 3. 21 250 KN INSTRON 8500 test rig (Boeing standard 4ASTM D 7137).**

The test rig was run at velocity of 1 mm/min using the test fixture detailed in Boeing testing procedure (4ASTM D 7137) as shown in Figure 3.22. Boeing standard specimens (100mm × 150mm). Displacement and load signals from INSTRON tester were recorded by the data synchronization system (as a trigger box).

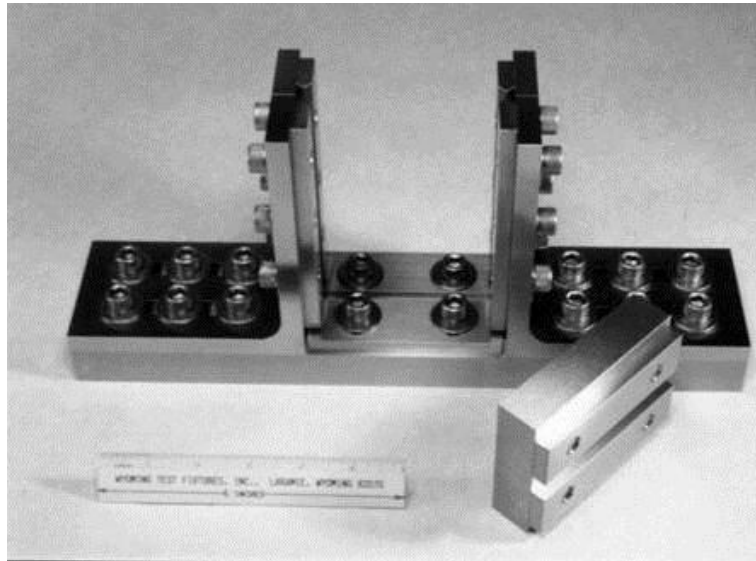


**Figure 3. 22 Boeing anti-buckling rig.**

The fixture used adjustable plates to provide simply support at the specimens' side edges to ensure the specimen is able to slide along the loading direction support the test specimens and the side supports are sharper edges, which provide the limited out of plane translation and prevent it from rotation. The specimens are clamped at both ends and the global bulking behaviour is limited during compression. The displacement-load measurements are performed during compressive loading of the undamaged, damaged and repaired specimens. The data synchronisation trigger box was used to monitor the displacement of the specimen during the compression test and then record the data on the computer to obtain the load-displacement curves.

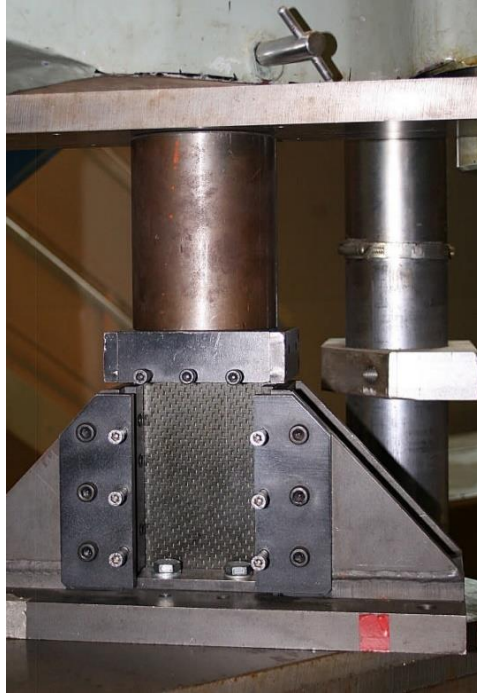


**Figure 3. 23 Experimental setup for compression After Impact (CAI) test (Cranfield University lap, 2013).**

### **3.5.1 Experimental test procedure**

The compressive test procedure was conducted as following:

Undamaged and damaged Compression-After-Impact (CAI) testing specimen with dimensions  $100.0 \pm 0.1$  mm  $150.0 \pm 0.1$  mm, 4.124-mm thick, CFRP laminate; 11 plies: (0/90), ( $\pm 45$ ), (0/90), ( $\pm 45$ , 0/90), ( $\pm 45$ ), (0/90), ( $\pm 45$ ), (0/90), ( $\pm 45$ ), (0/90) and 2.625 mm thick, CFRP laminate; 7 plies: ( $\pm 45$ ), (0/90), (0/90), ( $\pm 45$ ), (0/90), (0/90), ( $\pm 45$ ), were cut to meet the strict dimension requirement specified in ASTM D 7137, mounted into the compression fixture as shown in Figure 3.23 and the fixture was setup in correct position. Then pressed the start button on INSTRON control laminate and the fixture start to move which the specimen subjected to compression loading based on ASTM D 7137 specification at the rate of 1 mm/min. The INSTRON test rig automatically stop move when the specimen failed. Then the failure load and displacement were recorded and remove the specimen from the fixture.



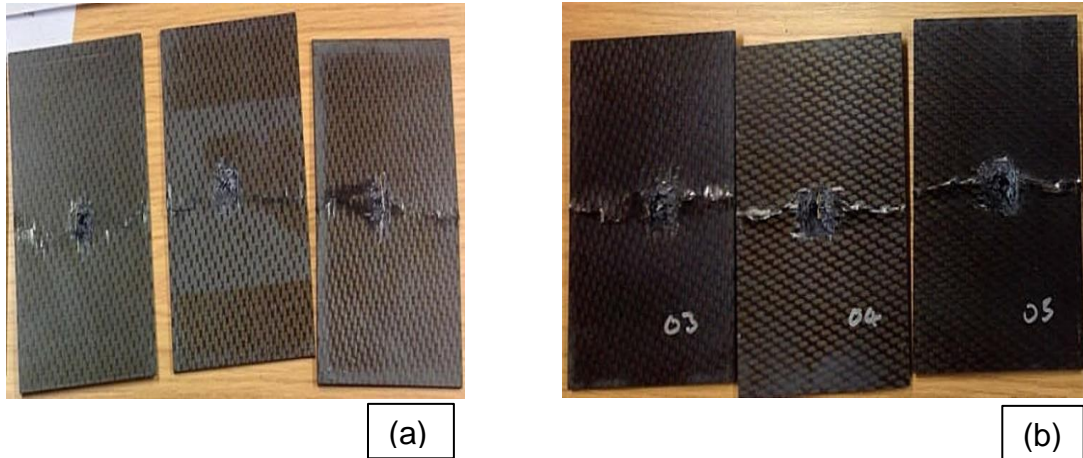


**Figure 3. 24 Impact damaged composite laminates subject to compression after impact test: (a) 7 Plies and (b) 11 Plies.**

Figure 3.24 (a) and (b) show that all the impact damaged specimens failed by delamination propagation due to local buckling that started at the impact damage location.

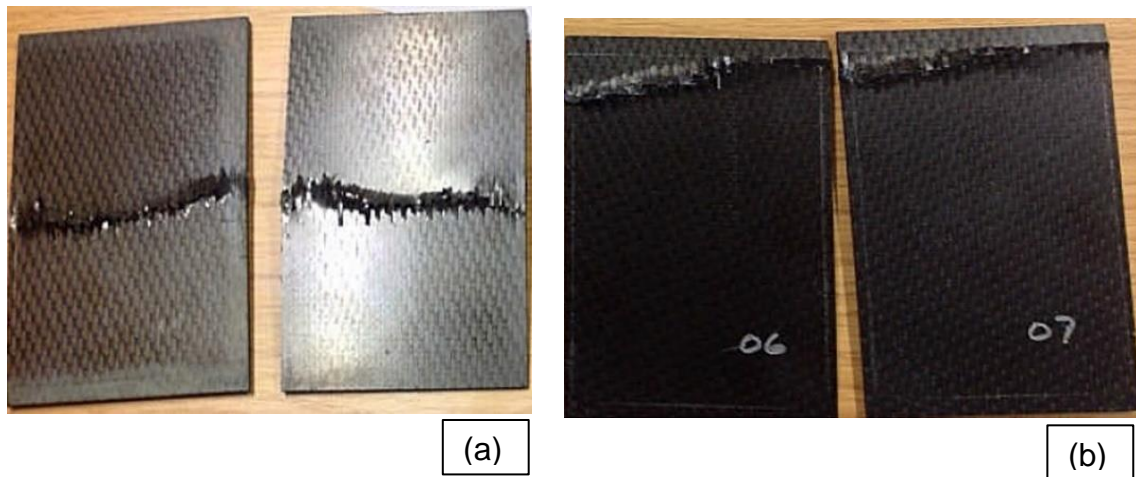


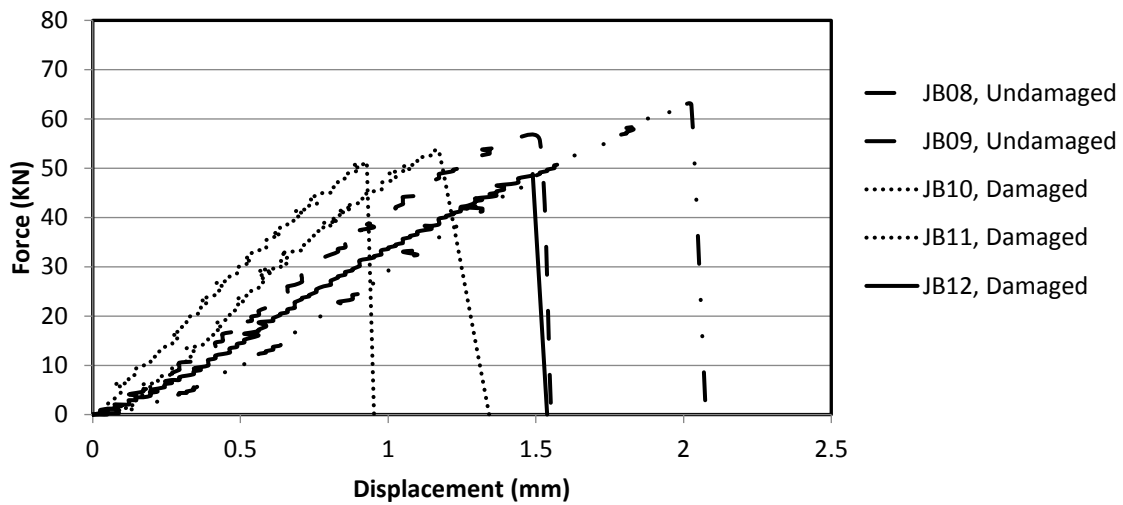
**Figure 3. 25 Composite laminates subject to compression after impact test: (a) 7 Plies and (b) 11 Plies.**

The Figure 3.25 (a) show the compression failure for 7 Plies specimen happened in the area between the clamped edge and the free supported edge, near to the middle of the specimen due to the local buckling. The Figure 3.25 (b) show the undamaged 11plies specimens failed by crushing brooming failure as presented in (Prichard et al., 1990; Liu et al., 1998).

**Table 3. 4 The specimens' parameters subject to CAI test.**

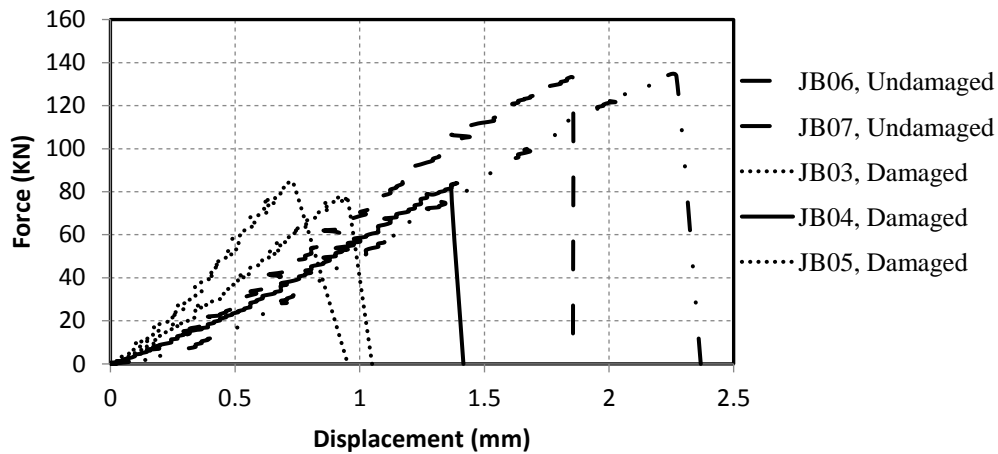
Plies	Job No.	Laminate status	Impact Velocity (m/s)	Failure Load (KN)
11	JB03	Damaged	266	76.4
	JB04	Damaged	260	83.9
	JB05	Damaged	245	84.7
	JB06	Undamaged		132.8
	JB07	Undamaged		133.7
7	JB08	Undamaged		55.5
	JB09	Undamaged		62.9
	JB10	Damaged	182	53.5
	JB11	Damaged	184	51.2
	JB12	Damaged	186	48.8

Table 3.4 presented all experimental results for the CRFP specimens were compressed to failure include two undamaged and three damage specimens for each thickness. The CFRP damaged specimens was subjected to various ranges of impact velocities (182m/s to 266 m/s).



**Figure 3. 26 Failure load versus displacement for undamaged and damaged 7 Plies CFRP composite laminate.**

The CAI tests show that the failure load was about 56-63 kN for the undamaged 7 plies CFRP specimens and 48-54 kN for the damaged 7 plies CFRP specimens as shown in Figure 3.26. Moreover, the 11 plies CFRP specimen was subject to CAI test and show that the failure load for undamaged specimen was about 132-133 kN and the damaged laminate failed about 76-85 kN as shown in Figure 3.27. Therefore, the CAI failure load of the undamaged specimen was higher than that of the damaged specimen. The undamaged 7 Plies CFRP composite laminate failed at approximately 23% higher CAI failure load than the damaged specimens. The undamaged 11 Plies CFRP composite laminate failed at approximately 40% higher CAI failure load than the damaged specimens.



**Figure 3. 27 Failure load versus displacement for undamaged and damaged 11 Plies CFRP composite laminate.**

In Figures 3.28 and 3.29 presented the relation between the compressive failure load and the impact velocity for damaged 11 plies and 7 plies CFRP composite laminate which shows that the compression failure load decreases linearly when the impact velocity increasing.

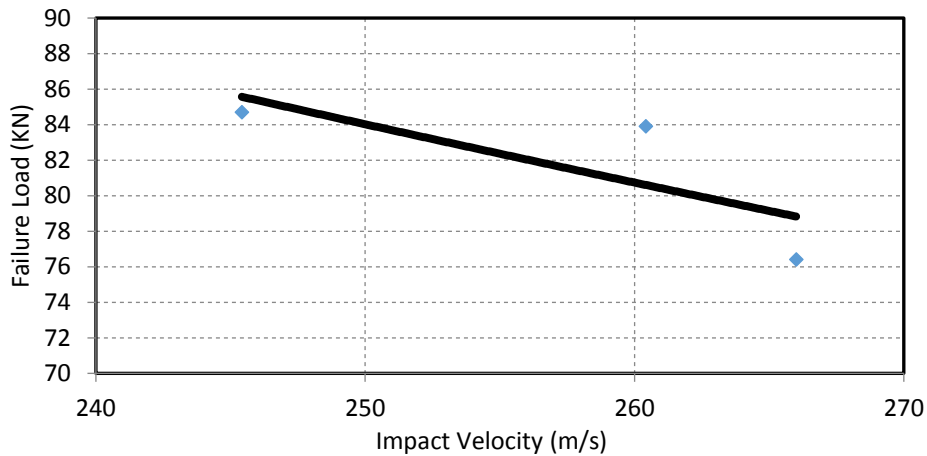


**Figure 3. 28 CAI failure load versus impact velocity for damaged 11 Plies CFRP composite laminate.**

Figure 3.28 shows the highest CAI compressive failure load (84 kN), although the impact velocity was (145 m/s) and lowest CAI compressive failure load was

(76 KN) even the impact velocity was the highest value (266m/s). The same concept shown in Figure 3.29 the failure of the specimen at highest impact velocity (187 m/s) leads to smallest compressive failure load (48.4 KN).

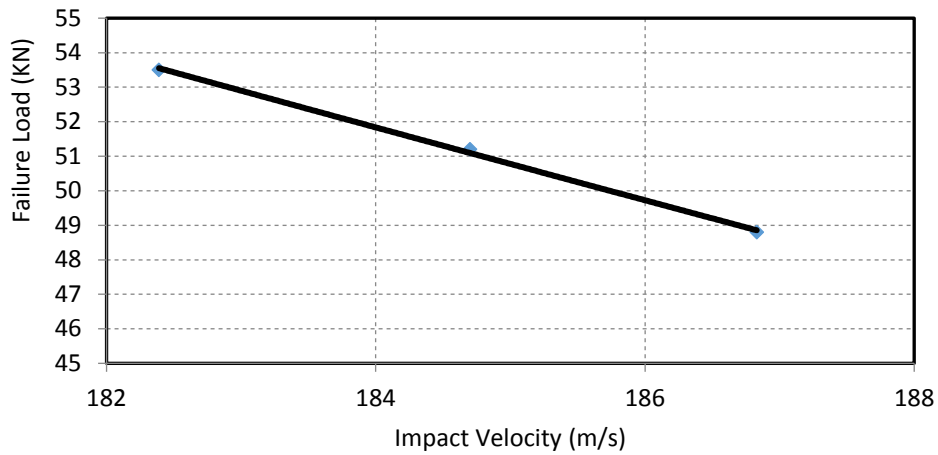


**Figure 3. 29 CAI failure load versus impact velocity for damaged 7 Plies CFRP composite laminate.**

Moreover, figures 3.28 and 3.29 shows that the CAI failure load is related to the impact velocity. It could be assumed that the increase impact velocity produced more delaminated area in the laminate and enhanced the material in the damaged area that can be decrease the CAI failure load.

# **Chapter 4**

## **Numerical Methodology**

#### **4.1 Practical numerical methodology to predict the best repair method after impact damage**

The study focussed on establish a practical numerical methodology to predict the optimum repair method to repair CFRP composite laminate was subject to high velocity impact damage. The work for this study was divided into two parts, the first part modelling the behaviour of Carbon-Fibre Reinforced Plastic (CFRP) composite laminates subject to high-velocity impact. The second part modelling the repaired and unrepaired composite laminates under compression load by using compression after impact test.

The simulation results were compared with the experimental data in a variety of ways: time histories of deformation; contact force and dissipated energy; hysteresis loops contained within force-deformation diagrams; etc. The delaminated and damaged areas from the experiments were also compared with the predictions of the numerical simulations.

#### **4.2 Finite Element Analysis**

Finite Element Analysis (FEA) can be used to simulate the behaviour of composite structures under impact damage. This subject of modelling has received extensive attention; for example, several FEA programs have been developed, such as Abaqus, LS-DYNA and Nastran, among others. FEA has proven to be an effective tool in measuring stress-strain distributions in complicated structures, which are impossible to record via conventional methods like strain gauging.

LS-DYNA is used in the analysis of the large deformation dynamic response of structures. This commercially available software has a large library of material options, such as composite materials, that have been widely used in the aerospace industries. Therefore, this code was chosen for use in the implementation of the numerical simulation and prediction of the impact response of the composite model.

This section first provides an overview of LS-DYNA, including aspects such as the explicit finite element method and time step calculation. Only the features that are relevant to this study are reviewed. Following the overview, a standalone explicit finite element code that was developed in order to better understand the LS-DYNA procedure will be described.

### **4.3 LS-DYNA**

Livermore Software Technology Corporation developed the LS-DYNA as a commercial tool. In the past decade of its development, considerable progress has been made, with hundreds of new features added, including material types and contact-impact algorithms, etc. LS-DYNA became a general-purpose finite element tool for large deformation dynamic response analysis of structures. LS-DYNA is used in the aircraft industry to assess crashworthiness and impact damage.

LS-DYNA is based on a Lagrange formulation and an explicit time integration scheme with a central difference algorithm (Hallquist, 2006). The explicit method evaluates local variables directly, without the need for global equilibrium calculations. LS-DYNA is primarily suited for performing impact and large deformation non-linear dynamic analysis. LS-DYNA has a wide variety of analysis capabilities, including a large number of material models, such as composite variety of contact and interface modelling algorithms, and a large library of element formulation, including two node beam elements, three and four node shell elements, rigid bodies and four node tetrahedron and eight node solid elements. A variety of element formulations is available for each element type.

#### **4.3.1 Lagrangian Formulation**

The finite element formulation used in LS-DYNA is derived from Lagrangian space, and most of the structural analysis problems are formulated in Lagrangian space (Livermore Software Technology Corporation, 2006). In order to solve a nonlinear three-dimensional dynamic problem, the deformed geometry of a body that is subjected to external forces needs to be calculated. To formulate this



problem, each point (P) in the body is defined initially at  $X_\alpha$  ( $\alpha=1, 2, 3$ ), where 1, 2, and 3 respectively represent the x, y, and z axes in the Cartesian coordinate system.

The current position of each point in the body  $x_i$  ( $i=1, 2, 3, \dots$ ) is expressed as a function of the point's initial coordinates, and time (t) in the same Cartesian coordinate system (Figure 4.1):

$$x_i = x_i(X_\alpha, t) ; \tag{4.1}$$

At time  $t=0$ , we have the initial conditions:

$$x_i(X_\alpha, 0) = X_\alpha ; \tag{4.2}$$

$$\dot{x}_i(X_\alpha, 0) = V_i(X_\alpha) ; \tag{4.3}$$

where  $V_i$  denotes the initial velocity.

### 4.3.2 Governing Equations

The next step to solving a nonlinear three-dimensional dynamic problem should find a solution to the momentum equation of that body which is located in a Lagrangian space, as shown in Figure 4.1. The body is subjected to traction forces ( $t_i(t)$  (forces per unit area)) over a part of its outer surface ( $S_t$ ), external body force ( $b_i(t)$  (force per unit volume)) over its whole volume ( $V$ ), and prescribed displacements ( $d_i(t)$ ) over the surface ( $S_d$ ):

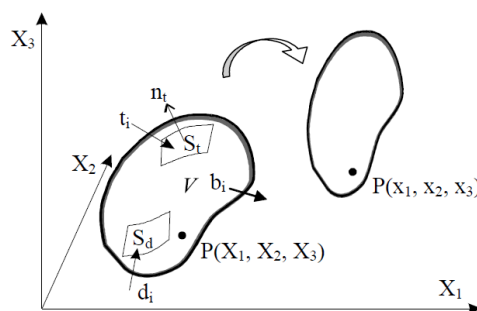


Figure 4. 1 Three dimensional body in Lagrangian space (Livermore Software Technology Corporation, 2006).

$$\sigma_{ij,j} + \rho P_i - \rho \ddot{x}_i = 0 ; \quad (4.4)$$

where  $\rho$  represents the material density,  $\ddot{x}$  is the acceleration and the comma denotes covariant differentiation.

Satisfying the traction boundary conditions

$$\sigma_{ij}n_j = f_i(t) ; \quad (4.5)$$

where  $\sigma_{ij}$  is Cauchy's stress tensor, and  $n_j$  is the outward normal unit vector to the traction surface  $S_t$ .

These equations are stating the problem in the strong form, which means they need to be satisfied at every point in the body or in the surface. To solve the problem numerically using the finite element method, the problem has to be defined in the weak form, in which the conditions have to be met only on an average or integral sense. In the weak form equation, an arbitrary virtual displacement,  $\delta x_i$ , that satisfies the displacement boundary condition in surface  $S_d$  is introduced. Multiplying Equation 4.4 by the virtual displacement and integrating over the volume of the body yields:

$$\int_V (\sigma_{ij,j} + \rho P_i - \rho \ddot{x}_i) \delta x_i dV = 0 ; \quad (4.6)$$

Note:

$$(\sigma_{ij}\delta x_i)_{,j} = \sigma_{ij,j}\delta x_i + \sigma_{ij}\delta x_{i,j} ; \quad (4.7)$$

Substituting for the first term in Equation 4.6 leads to:

$$\int_V ((\sigma_{ij}\delta x_i)_{,j} - \sigma_{ij}\delta x_{i,j} + \rho P_i\delta x_i - \rho \ddot{x}_i\delta x_i) dV = 0 ; \quad (4.8)$$

The first term in Equation 4.8 can be expressed over surface of the body as:

$$\int_V (\sigma_{ij}\delta x_i)_{,j} dV = \int_{S_t} (\sigma_{ij}\delta x_i)n_j dS ; \quad (4.9)$$

With the traction boundary in Equation 4.5, Equation 4.9 can be written as:

$$\int_V (\sigma_{ij}\delta x_i)_{,j} dV = \int_{S_t} f_i \delta x_i dS ; \quad (4.10)$$

With the traction boundary in Equation 4.10, Equation 4.8 can be written as:

$$\int_V \rho \ddot{x}_i \delta x_i dV + \int_V \sigma_{ij} \delta x_{i,j} dV - \int_V \rho P_i \delta x_i dV - \int_{S_t} f_i \delta x_i dS = 0 ; \quad (4.11)$$

It is a statement of the principle of virtual work for the general three-dimensional problem defined in Figure 4.2.

### 4.3.3 Spatial Discretisation

The next step in deriving the finite element equations is spatial discretisation. This is achieved by first superimposing a mesh of finite elements interconnected at nodal points, then shape functions are introduced to establish a relationship between the displacements at inner points in the elements and the displacements at the nodal points:

$$\delta x_i = \sum_{\alpha=1}^n N_{\alpha} \delta x_{\alpha i} ; \quad (4.12)$$

where  $\delta x_i$  are the displacements at a point inside the element,  $n$  represents the number of nodal points defining the element,  $N_{\alpha}$  denotes the shape function at node  $\alpha$ , and  $\delta x_{\alpha i}$  represent the displacements at node  $\alpha$ . Similar expressions can be written for the coordinates, velocities, and acceleration of a point inside the element.

The finite element equations are derived by discretising the virtual work Equation 4.11 in space as:

$$\sum_{m=1}^M \left\{ \int_{V_m} \rho \ddot{x}_i \delta x_i dV_m + \int_{V_m} \sigma_{ij} \delta x_{i,j} dV_m - \int_{V_m} \rho P_i \delta x_i dV_m - \int_{S_t} f_i \delta x_i dS_m \right\} = 0 ; \quad (4.13)$$

where  $M$  is the total number of elements in the system and  $V_m$  is the volume of the element. Replacing the virtual displacements  $\delta x_i$ , and the accelerations  $\delta x_{\alpha i}$  with the interpolations from Equations 4.12 and 4.13 gives:

where  $\delta x_i$  and  $\delta x_{\alpha i}$  represent the virtual displacement and the accelerations at the nodal points respectively. Equation 4.14 can be simplified to:

$$\sum_{m=1}^M \left\{ \int_{V_m} \rho \langle N_\beta \ddot{x}_{\beta i} \rangle \langle N_\alpha \delta x_{\alpha i} \rangle dV_m + \int_{V_m} \sigma_{ij} \langle N_{\alpha, j} \delta x_{\alpha i} \rangle dV_m - \int_{V_m} \rho P_i \langle N_\alpha \delta x_{\alpha i} \rangle dV_m - \int_{S_t} f_i \langle N_\alpha \delta x_{\alpha i} \rangle dS_m \right\} = 0 ; \quad (4.14)$$

$$\sum_{m=1}^M \left\{ \int_{V_m} \rho N_\alpha N_\beta \ddot{x}_{\beta i} dV_m + \int_{V_m} N_{\alpha, j} \sigma_{ij} dV_m - \int_{V_m} N_\alpha \rho P_i dV_m - \int_{S_t} f_i N_\alpha dS_m \right\} = 0 ; \quad (4.15)$$

Equation 4.15 can be rewritten as:

$$\sum_{m=1}^M \left\{ \int_{V_m} \rho N_\alpha N_\beta dV_m \right\} \ddot{x}_{\beta i} = \sum_{m=1}^M \int_{V_m} N_\alpha \rho P_i dV_m + \sum_{m=1}^M \int_{S_t} f_i N_\alpha dS_m - \sum_{m=1}^M \int_{V_m} N_{\alpha, j} \sigma_{ij} dV_m ; \quad (4.16)$$

In matrix form, Equation 4.16 becomes:

$$[M] \{ \ddot{X} \} = \{ F \} ; \quad (4.17)$$

where  $[M]$  is the mass matrix,  $\{ \ddot{X} \}$  represents the acceleration vector, and  $\{ F \}$  is the vector summation of all the internal and external forces. Equation 4.17 is the finite element equation that needs to be solved at each time step. The solution procedure consists of first computing all internal and external forces and summing them for each degree of freedom of the system. The accelerations are then determined by dividing these forces at the corresponding degree of freedom by the mass.

#### 4.3.4 Central Difference Method

The governing finite element Equation 4.17 needs to be solved at each time step. In order to do so, it is written in discrete form as:

$$[M]\{\ddot{X}\}_n = \{F\}_n ; \quad (4.18)$$

where  $\{\ddot{X}\}_n$  is the acceleration vector at time  $t_n$ , and  $\{F\}_n$  is the sum of all external and internal force vectors at time  $t_n$ .

The time interval between two successive points in time,  $t_{n-1}$  and  $t_n$ , is the time step  $\Delta t_n = t_n - t_{n-1}$ . LS-DYNA uses time steps varying with time. This is necessary in most practical calculations since the stable time step will change as the mesh deforms.

In numerical analysis, integration methods are classified according to the structure of the time difference equation. The difference formula is called “explicit” if the equation for the function at time step  $n$  only involves the derivatives at previous time steps. Explicit integration methods generally lead to solution schemes that do not require the solution of a coupled system of equations, provided that a lumped mass matrix is used instead of a consistent mass matrix.

In computational mechanics and physics, the central difference method is a popular explicit method. The formulation in LS-DYNA uses the central difference explicit method to discretise the finite element equation in time.

The displacement and acceleration vectors are computed at times  $t_1, \dots, t_n, t_{n+1}, \dots, t_f$  (where  $t_f$  is the end time) and the velocity vector is computed at times  $t_{1/2}, \dots, t_{n-1/2}, t_{n+1/2}, \dots, t_{f-1/2}$ .

The calculation is started with the initial values for the displacements and accelerations at time  $t_0$  and an approximation of the velocities at time  $t_{0-1/2}$  (half a time step before time  $t_0$ ). The solution is incremented using the central difference equations as:

$$\dot{X}_{n+1/2} = \dot{X}_{n-1/2} + \ddot{X}_n \Delta t_n ; \quad (4.19)$$

$$X_{n+1} = X_n + \dot{X}_{n+1/2} \Delta t_{n+1/2}; \quad (4.20)$$

$$\ddot{X}_{n+1} = M^{-1} F_{n+1}; \quad (4.21)$$

$$\Delta t_{n+1/2} = \frac{1}{2} (\Delta t_n + \Delta t_{n+1}); \quad (4.22)$$

From Equation 4.19, the velocity vector at is computed. This velocity vector is then used in Equation 4.20 to compute the displacement vector at  $t_{n+1}$ . With the strain-displacement relationship and constitutive equation, stresses can be calculated to obtain the internal forces on element nodes. The internal and external forces are summed at each nodal degree of freedom to assemble the force vector. Then the acceleration vector at time  $t_{n+1}$  can be determined with Equation 4.21. The final step is to update the time step  $\Delta t_{n+1/2}$  using Equation 4.22. The calculation of time step  $\Delta t_{n+1}$  will be explained in the next section.

#### 4.3.5 Time Step Control

The time step in an explicit analysis is defined as the minimum stable time step in any deformable element in the overall mesh. The time step size is determined by accounting the minimum value over all elements:

$$\Delta t_{n+1} = \alpha \cdot \min\{\Delta t_1, \Delta t_2, \dots \dots i \Delta t_N\}; \quad (4.23)$$

where  $N$  represents the number of elements. For stability reasons, the scale factor  $\alpha$  is typically set to a value of 0.9 or smaller value (0.9 is the default value in LS-DYNA).

The choice of the time step is critical in a dynamic analysis because a small time step can make the computation inefficient, while large time steps may produce unstable simulations. The critical time step has to be small enough such that the stress wave does not travel across more than one element at each time step. LS-DYNA will check all of the elements while determining the required time step in an analysis. The time step can be estimated roughly based on the following:

$$\Delta t_e = \frac{L}{c}; \quad (4.24)$$

where  $\Delta t_e$  is the critical time step of an element in the model,  $L$  is the characteristic length, and  $c$  is the sound speed in the body.

For 8 node solid elements, the characteristic length is determined by:

$$L = \frac{V}{A_{max}}; \quad (4.25)$$

where  $V$  is the element volume and  $A_{max}$  is the area of the largest side.

The sound speed  $c$  can be expressed as:

$$c = \sqrt{\frac{E(1-\nu)}{(1+\nu)(1-2\nu)\rho}}; \quad (4.26)$$

where  $E$  is Young's modulus,  $\rho$  is density and  $\nu$  is Young's modulus.

In order to model the high velocity impact, the overview of LS-DYNA theory, including aspects such as the explicit finite element method, and time step calculation was reviewed. The overview of the modelling process and LS-DYNA application is presented in the next section.

#### 4.4 Modelling Methodology

Modelling of composite laminate subject to high velocity impact is one of the most difficult problems for finite element application because this model should involving many parameters such as high velocity contact and material erosion failure. For CFRP, the failure mechanisms are further complicated, involving different types of damage and failure, including fibre breakage, matrix cracking, and/or delamination.

The modelling process follows multiple steps. Firstly, the contact event is detected, then the element contact force and deformation are calculated using the material stiffness and dynamic impact condition. When the element's stress or strain reaches a failure value, the element will be deleted. For simulation of

penetration, a material failure criterion was used for the elimination of failed elements.

The one of major objective of this research was to establish a modelling methodology to predicate impact damage behaviour in CFRP composite materials. This methodology are:

1. The parameters for the model were determined by direct experimental measurement or estimation.
2. Impact damage tests were simulated to validate the behaviour of material model.
3. The predicted kinetic energy components histories and damage modes were correlated with experimental results.

#### **4.4.1 Modelling Process**

The FEA modelling process consists of three steps:

##### ***Per-processing***

The model uses TrueGride (Version 2.1.0 XYZ Scientific Application, Inc.) to create a three dimensional (3D) mesh. The LS-PREPOST software was used to create the input files, which contained material properties and boundary conditions.

##### ***Solver***

The solver calculates the system of equations that describes the behaviour of the model. The solver used in this study is the commercial nonlinear LS-DYNA explicit finite element code (Livermore Software Tech. Corp., 2006). This code was developed at the Lawrence Livermore National Laboratory.

##### ***Post-processing***



The LS-PREPOST software was used for qualitative and quantitative analysis of the results obtained from the solver. These results were then validated against the experimental test.

#### 4.5 Composite Material Model in LS-DYNA

LS-DYNA includes various material models that support the analysis of composite material in elastic as well as non-linear failure regions. Some available composite material models in LS-DYNA (2007) are summarised as shown in Table 4.1:

**Table 4.1 Composite material models in LSDYNA**

Material Model	Solid Element	Shell Element	Damage	Shear	Strain rate	Failure Criteria
<b>MAT_022</b> ( Composite Damage)	√	√	√	√		<b>Chang-Chang</b>
<b>MAT_054</b> (Enhanced Composite Damage)		√	√	√		<b>Chang-Chang</b>
<b>MAT_055</b> (Enhanced Composite Damage)		√	√	√		<b>Tsai-Wu</b>
<b>MAT_058</b> (Laminated Composite Fabric)		√	√			<b>Hashin</b>
<b>MAT_059</b> (Composite Failure optional model)	√	√	√			<b>Tsai-Wu Chang-Chang</b>
<b>MAT_161/162</b> (Composite MSC)	√		√		√	<b>Hashin Delamination</b>

MAT\_022 (MAT\_COMPOSITE\_DAMAGE) is based on the Chang-Chang failure criteria with four failure modes: fibre and matrix tensile and compressive failure modes due to in-plane stresses in unidirectional lamina (*LS-DYNA3D Theoretical Manual*, 2007).

MAT\_054 and MAT\_055 (MAT\_ENHANCED\_COMPOSITE\_DAMAGE) use Chang–Chang failure criterion and Tsai–Wu failure to simulate composite failure. The advantageous feature of these materials models is that one can specify failure strains of matrix and fibre. These two material models do not assume tensile strength in fibre direction to equal compressive strength in fibre direction.

(Schweizerhof al et. 2005) studied various material models in LS-DYNA for composite material. The merits and limitations of all of the available composite material models in LS-DYNA for predicting complex crushing behaviour, including structures undergoing larger deformations, were studied using one element simulations. MAT\_54, MAT\_58a, MAT\_58b, MAT\_59a and MAT\_59b were used for the simulations.

MAT\_58 (MAT\_LAMINATED\_COMPOSITE\_FABRIC) is based on the Hashin criteria and continuum damage mechanics. This material model is used for a calibration of the reduction factors for tensile and compressive fibre strength after matrix compressive or tensile failure.

MAT\_161/162 (MAT\_COMPOSITE\_MSC) are based on the Hashin's failure criteria (1980) and the continuum damage mechanics (CDM) constitutive model (Matzenmiller, 1995), which describe the post-elastic growth of damage and strain softening after failure. This material model is able to simulate five failure modes: fibre fracture, fibre crush, through the thickness matrix failure and delamination (Livermore Software Tech. Corp., 2006). Furthermore, they are useful in simulating the progressive failure mode in composite material consisting of unidirectional composite laminates and woven fabric composite structures. However, the disadvantage of this materials model is that it needs quite a large number of material property input, which is not easily accessed by standard material tests, and requires a special license from MSC, which is not readily available.

MAT\_59 (MAT\_COMPOSITE\_FAILURE\_OPTIONAL\_MODEL) can be used for both shell and solid elements. This material model is close to MAT\_54. MAT\_59 will be used in this thesis, as it can simulate the progressive failure of composite

laminates during high velocity impact, which characterises the failure by decreasing the material stiffness. A detailed description of this material model is provided in the next section, and can be found in the LS-DYNA3D theoretical manual (2007).

The failure criteria used in material model 059 is based on the maximum stress failure criterion, which contains three failure criteria. The failure surface associated with MAT\_59 when hexahedral elements are used is similar to the Tsai-Wu interactive criterion (Tsai and Wu, 1971).

## **4.6 Failure Criteria**

This section is concerned with numerical modelling of failure in CFRP composite and a review of failure criteria. In the analysis of composite structures, several finite element analysis codes are used to obtain the condition of stress and strain of the target of a study of impact damage behaviour. The modelling of impact damage and damage progression can be achieved through the application of finite element analysis, such as LS-DYNA. Although most finite element codes in LS-DYNA follow approximately similar procedures for the calculation stresses, they differ in the failure criteria. Researchers have been developing the failure criteria for composite materials over three decades, and there are numerous of theories available in the literature. These criteria can be classified as being based on theories of fracture mechanics or stresses.

### **4.6.1 Fracture Mechanics**

A fracture mechanics approach would appear preferable for a study of damage behaviour including the crack propagation (growth) in the structure. Ruiz and Harding (2000) have explained the limitation of the fracture mechanics that can be applied for damage analysis of metals when the crack growth occurs at a continuous rate through the material, but the fracture mechanics are not valid to layered structures. Moreover, in quasi static problems, the lack of the data of high speed crack growth and strain rate sensitivity can limit the applicability of fracture

mechanics. However, delamination can be treated successfully by fracture mechanics.

#### 4.6.2 Stress Based Failure Criteria

Stress based failure criteria have been proposed for the prediction of the progression of all types of damage. The application of the stress approach is usually quite simple, and it is most commonly applied to define the damage initiation, and not the propagation of any existing damage. As explained previously, there are a number of failure criteria used in LS-DYNA finite element coding to model the impact damage behaviour of CFRP composite structures. These criteria are different from one material model to another, and in this study, the author used material model 059 to model the high velocity impact damage in composite material. This material model can be used to assess three types of failure criteria dependent to damage behaviour, as detailed in following:

##### 4.6.2.1. Maximum Stress Failure Criterion

The maximum stress failure criterion, which is based on maximum stress failure criterion, corresponds to the strength in fundamental failure modes. Wang and Bsrtholomeusz (2004) have used material model 59 in LS-DYNA to predict residual velocities and delamination areas, which are based on the maximum stress failure criterion. Others have also used material model 59 (Fawaz et al., 2004; Deka et al., 2008).

Four failure modes are possible in this criterion:

(a) *Tensile fibre failure*  $\sigma_1 \geq 0$

$$F_{fibre} = \left( \frac{\sigma_1}{\sigma_{XT}} \right)^2 - 1 \begin{cases} \geq 0 & \text{failed} \\ < 0 & \text{elastic} \end{cases} ; \quad (4.27)$$

When failed, the material is degraded through setting  $E_1 = E_2 = G_{12} = \nu_2 = \nu_1 = 0$ .

(b) *Compressive fibre failure*  $\sigma_1 < 0$

$$F_{fibre} = \left( \frac{\sigma_1}{XX_C} \right)^2 - 1 \begin{cases} \geq 0 & \text{failed} \\ < 0 & \text{elastic} \end{cases} ; \quad (3.28)$$

When failed, the material is degraded through  $E_1 = \nu_2 = \nu_1 = 0$

(c) *Tensile matrix failure*  $\sigma_2 < 0$

$$F_{matrix} = \left( \frac{\sigma_2}{YY_T} \right)^2 + \left( \frac{\sigma_{12}}{S_{BA}} \right)^2 - 1 \begin{cases} \geq 0 & \text{failed} \\ < 0 & \text{elastic} \end{cases} ; \quad (4.29)$$

When failed, the material is degraded through  $E_2 = \nu_1 = 0 \quad G_{12}=0$

(d) *Compressive matrix failure*

$$F_{matrix} = \left( \frac{\sigma_2}{2S_{BA}} \right)^2 + \frac{\sigma_2}{YY_C} \left[ \frac{YY_C^2}{4S_{AB}^2} - 1 \right] + \left( \frac{\sigma_{12}}{S_{BA}} \right)^2 - 1 \begin{cases} \geq 0 & \text{failed} \\ < 0 & \text{elastic} \end{cases} ; \quad (4.30)$$

When failed, the material is degraded through  $E_2 = \nu_2 = \nu_1 = G_{12}=0$

where  $XX_T$  is longitudinal tensile strength,  $XX_C$  represents longitudinal compressive strength,  $YY_T$  is transverse tensile strength,  $YY_C$  is transverse compressive strength, and  $S_{BA}$  is in plane shear strength.

#### 4.6.2.2. Chang–Chang Criterion

A significant amount of work has been done on modelling the failure mechanism of composites subjected to impact loading based on Chang–Chang criterion. Zeng et al., (2005) reported a computational model that uses material model 59, which is based on the methodology developed by Chang-Chang, to predict composite damage.

This methodology contains three failure modes of composite laminates (both unidirectional and plain weave laminates). This failure mode is a linear orthotropic constitutive law valid for composite with brittle failure. Three failure criteria are applicable in this criterion:

(a) *Fibre breakage*:

$$F_{fiber} = \left( \frac{\sigma_1}{XX_T} \right)^2 + \bar{\tau} \geq 1 ; \quad (4.31)$$

Where  $\sigma_1$  is longitudinal stress,  $XX_T$  is longitudinal tensile strength and  $\bar{\tau}$  is the ratio of the shear stress to the shear strength and can be expressed as:

$$\bar{\tau} = \frac{\frac{\sigma_{12}^2}{2G_{12}} + \frac{3}{4}\alpha\sigma_{12}^4}{\frac{S_{BA}^2}{2G_{12}} + \frac{3}{4}\alpha S_{BA}^4}; \quad (4.32)$$

$G_{12}$  represents in plane shear modulus,  $\sigma_{12}$  is shear stress,  $S_{BA}$  denotes plane shear strength and  $\alpha$  is a nonlinear shear stress parameter that is defined by material shear stress–strain measurements.

When fibres experience breakage, the material constants  $E_1$ ,  $E_2$ ,  $G_{12}$ ,  $v_1$  and  $v_2$  are set to zero.

(b) *Matrix cracking:*

$$F_{matrix} = \left(\frac{\sigma_2}{YY_T}\right)^2 + \bar{\tau} \geq 1; \quad (4.33)$$

Where  $\sigma_2$  is transverse stress and  $YY_T$  is transverse tensile strength. When the matrix failure happen the material constants  $E_2$ ,  $G_{12}$ ,  $v_1$  and  $v_2$  are set to zero.

(c) *Compressive failure:*

$$F_{comp} = \left(\frac{\sigma_2}{2S_{BA}}\right)^2 + \left[\left(\frac{YY_C}{2S_{BA}}\right)^2 - 1\right] \frac{\sigma_2}{YY_C} + \bar{\tau} \geq 1; \quad (4.34)$$

where  $YY_C$  denotes transverse compressive strength which is obtained from material strength measurement. When compressive failure occurs, the material constants  $G_{12}$ ,  $v_1$  and  $v_2$  are set to zero.

#### 4.6.2.3. Tsai-Wu Criterion

In the Tsai-Wu criterion, the tensile and compressive fibre modes are treated as Chang–Chang criterion. However, the failure criterion for the tensile and compressive matrix modes is given as:

$$F_{matrix} = \frac{\sigma_2^2}{YY_C YY_T} + \left(\frac{\sigma_{12}}{S_{BA}}\right)^2 + \frac{(YY_C - YY_T)\sigma_2}{YY_C YY_T} - 1 \begin{cases} \geq 0 & \text{failed} \\ < 0 & \text{elastic} \end{cases}; \quad (4.35)$$

Sriram et al (2006), as well as Azevdo and Alves (2007) have used material model 59 in LS-DYNA. This material model implements the Tsai-Wu failure criterion (Tsai and Wu, 1971).

The failure surface associated with MAT\_59 when hexahedral elements are used is similar with the Tsai-Wu (Tsai and Wu, 1971). The failure surface is then:

$$F_{surface} = \frac{4\left(\sigma_1 - \frac{XX_T - XX_C}{2}\right)^2}{(XX_T + XX_C)^2} + \frac{4\left(\sigma_2 - \frac{YY_T - YY_C}{2}\right)^2}{(YY_T + YY_C)^2} + \frac{\sigma_{12}^2}{S_{BA}^2} + \frac{\sigma_{13}^2}{S_{AC}^2} + \frac{\sigma_{23}^2}{S_{BC}^2}; \quad (4.36)$$

Table 4.2 describes the difference or similarity between the maximum stress failure criterion, Chang-Chang criterion and Tsai-Wu criterion:

**Table 4. 2 The failure modes for the maximum stress failure criterion, Chang-Chang criterion and Tsai-Wu criterion.**

	Tensile fibre	Compressive fibre	Tensile matrix	Compressive matrix	Failure surface	Fibre breakage	Matrix cracking	Compressive failure
Maximum stress failure	x	x	x	x				
Chang-Chang						x	X	x
Tsai-Wu	x	x	x	x	x			

This study used the maximum stress failure criterion, on the basis of which researchers can predict residual velocities, hole areas and delamination areas. Failure of a composite is deemed to occur when the combined stresses reach a critical value. When the stress in the fibre direction reaches the failure value, LS-DYNA deletes the element. However, in cases of shear stress or normal stresses in the matrix, or when through-thickness directions exceed the failure value, LS-DYNA reduces the element stiffness to a negligible value, but retains this element for the remainder of the calculations, and is only removed when fibre failure occurs.

This simplified failure model can yield good results, but causes numerical problems under large deformations. Therefore, an element erosion criterion was used to remove the elements when a strain failure criterion was reached. So as not to affect the performance of the model, a failure strain of 80% was chosen. Numerical modelling of high-velocity impact required care when defining the contact between projectile and target.

## **4.7 Contact Interfaces Modelling**

There are three ways in which LS-DYNA treats contact between bodies: the Kinematic Constraint method; the Penalty method and the Distributed Parameter method. Several types of contact interfaces can be defined in LS-DYNA, including surface to surface, nodes to surface, nodes tied to surface, and surface tied to surface contacts, among others. LS-DYNA currently contains approximately one hundred material constitutive models and ten equations-of-state to cover material behaviour ranging from the very simple elastic material to the elastic-plastic strain-rate-dependent material.

The most advantageous capability of LS-DYNA over other finite element codes is its contact algorithm. As noted, several types of contact interfaces can be defined in LS-DYNA. To account for the deletion of elements, \*CONTACT\_ERODING\_SINGLE\_SURFACE was used, which allows LS-DYNA to model subsequent contact between the projectile through thickness elements once deletion of the upper layers occurs.

Nodal mass and time step determine the contact stiffness at the interface where two nodal masses are separated by a spring. Negative contact energy is sometimes generated when parts slide relative to one another. This effect was minimised by controlling the initial node penetration and time step scale factor. The effect of frictional forces in interfaces is typically assumed to be negligible. The static friction (FS) is greater than the dynamic friction (FD). In this study, FD was considered to be 0.1 and FS to be 0.3.



### 4.7.1 Hourglass Control

In the dynamic simulation, hourglass energy (HGE) modes represent non-physical, zero-energy modes of deformation that produce zero strain and stress. An accurate simulation requires a very small hourglass, such as 10% of the peak of the internal energy (IE). High amounts of hourglass energy can cause modelling instability. For this study, mesh refinement and the HGE coefficient type 4 (QM = 0.1), which provides a stiffness-based control, thereby minimizing distortion of the elements, was used to reduce the hourglass energy.

### 4.7.2 Energy

The kinetic energy of the projectile is transferred to the CFRP plane and absorbed through the several failure mechanisms. This change of projectile kinetic energy can be expressed as:

$$\Delta E_{projectile} = E_{initial} - E_{End} ; \quad (4.38)$$

$$E_{End} = IE_{plane} + KE_{plane} + HGE_{plane} + KE_{erode} + IE_{erode} ; \quad (4.39)$$

The difference between the impact and residual velocities is calculated by first calculating the kinetic energy transferred from the projectile to the laminate due to the impact resistance, using the following formula:

$$E = \frac{1}{2} m_p v_i^2 - \frac{1}{2} m_p v_r^2 - \frac{1}{2} m_d v_r^2 \approx \frac{1}{2} m_p (v_i^2 - v_r^2) ; \quad (4.40)$$

## 4.8 Material Model

### 4.8.1 Projectile Model

The spherical steel projectile was modelled using \*MAT\_ELASTIC\_PLASTIC\_HYDRO, as no significant deformation of the projectile was observed during the experimental test. The projectile is assumed to be ELASTIC PLASTIC HYDRO compared to the composite due to the difference of mass and stiffness, and because the modulus of the projectile is large compared to the through-thickness modulus of the composite.

The projectile was spherical ( $11.97\text{mm} \pm 0.01\text{mm}$ ) and constructed from a fully annealed stainless steel with a mass of  $7.165\text{ gm} \pm 1\text{e-}3\text{ g}$ . Two material properties (Density =  $7.9200\text{E-}3\text{ g/mm}^3$ , young modulus  $E = 2.0000\text{E+}5\text{ MPa}$  and Poisson's ratio  $\nu = 0.3$ ) are required for this material model. This approximation reduced computational time and was very cost efficient. For the projectile, MAT\_ELASTIC\_PLASTIC\_HYDRO was used. A four-node Belytschko-Tsay element with one through-thickness integration point was used for the projectile.

#### **4.8.2 Composite Laminate Model**

The study includes three thickness of composite laminates, the first thickness 6 mm thick woven CFRP laminate was made from 16 layers which used to validity the numerical result with the Hizell experimental result, the second thickness 4.125 mm was made from 11 layers and third thickness 2.625 mm was made from 7 layers. All woven composite laminates were made of Hexcel G0926 Carbon Fabric 5 harness 6K, Areal Wt 370 gsm. The resin used was Hexcel RTM 6 cured for 1 hour and 40 minutes at  $180^\circ\text{ C}$  at a pressure of 100 psi. The laminate was square with 6mm in thickness and each side with a length of 100mm. The lay-out of the three thickness composite laminates was as follows: The laminate had 16 layers, using the following stacking sequence: [(0/90); ( $\pm 45$ ); ( $\pm 45$ ); (0/90); ( $\pm 45$ ); ( $\pm 45$ ); (0/90); (0/90); ( $\pm 45$ ); (0/90); ( $\pm 45$ ); (0/90); ( $\pm 45$ ); (0/90); ( $\pm 45$ ); (0/90)]. The laminate had 11 layers, using the following stacking sequence: [(0/90); ( $\pm 45$ ); (0/90); ( $\pm 45$ ); (0/90); ( $\pm 45$ ); (0/90); ( $\pm 45$ ); (0/90); ( $\pm 45$ ); (0/90)]. The laminate had 7 layers, using the following stacking sequence: [( $\pm 45$ ); (0/90); (0/90); ( $\pm 45$ ); (0/90); (0/90); ( $\pm 45$ )]. The density of the CFRP material was  $1.5129200\text{E-}3\text{ g/mm}^3 \pm 1.0\text{E-}5\text{ g/mm}^3$ .

The CFRP laminate was meshed with 111393 elements and 121380 nodes, whereby one solid element was used to represent the thickness of each individual ply, as shown in Figure 4.2. The steel sphere projectile was meshed with 1023 elements and 1240 nodes and assigned an initial velocity. The solid elements (8 node hexahedron element) used a single integration point (ELFORM =1) due to

its computational efficiency over fully integrated elements. In addition, symmetry planes were defined to reduce computational time.

Since it is a localised impact, the mesh of the plate under the projectile was much finer than other parts of the plane. Simply supported boundary conditions were applied along the edges of the plate, which is fixed in all directions. The above program takes about 15 hours of run time due to the size of mesh and time step.

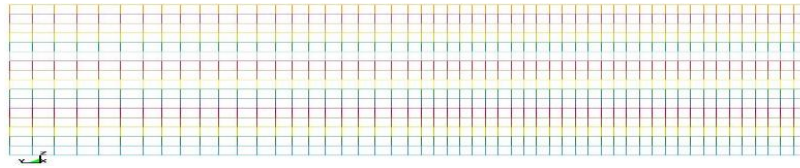


**Figure 4. 2 Finite element model of a composite laminate (100x100mm<sup>2</sup>)**

#### **4.8.2.1 Composite Laminate Parameters**

In \*MAT\_59, twenty material parameters are required to enable the predictive modelling of impact damage on composite laminate. These parameters can be obtained from different sources, including experimental characterisation, factory databases, handbooks, and open literature. Some material parameters need to be estimated and validated by applying iterative techniques.

The experimental data provided by Hazell (Hazell al et, 2008) as initial baseline values for the composite were implemented and tuned to provide a better correlation against experimental results. For this study, the change in kinetic energy was deemed to be a useful parameter, as approximating this value would ensure a representative stiffness of the overall plate, not only during initial failure, but also incorporating the resulting change in stiffness/element deletion for subsequent ply failures.

Elastic moduli, shear moduli and Poisson's ratio have been proposed based on previous projects completed by the Crashworthiness, Impact & Structure Mechanics (CISM) Group in Cranfield University. Characterising strength parameters is critical, as these parameters will affect the transfer of energy

between projectile and specimen, which for a shear plugging type failure are controlled by the transverse shear strength  $ca$  ( $S_{CA}$ ) and transverse shear strength  $cb$  ( $S_{CB}$ ). Therefore, the author used this characteristic to estimate the strength parameters by validating the numerical results using the change of kinetic energy against the experimental data.

Iterative techniques were employed to estimate the longitudinal tensile strength a-axis ( $XX_T$ ), transverse tensile strength b-axis ( $YY_T$ ), longitudinal compressive strength a-axis ( $XX_C$ ), transverse compressive strength b axis ( $YY_C$ ) and in-plane shear strength  $ba$  ( $S_{BA}$ ).

The process involved starting with initial strength values and keeping all other parameters constant. The first simulation results were compared with the experimental result. Then, the parameters were adjusted iteratively over several simulation runs until the simulation results were tuned to the experimental data. From this analysis, the values for the remaining parameters were determined.

**Table 4. 3 Material parameters for CFRP laminates**

$E_a$	$E_b$	$E_c$	$G_{ab}$	$G_{bc}$	$G_{ca}$	$\nu_{ba}$	$\nu_{bc}$	$\nu_{ca}$
72.2 GPa	72.2 GPa	1.12 GPa	6 GPa	6 GPa	6 GPa	0.04	0.04	4 E-4
$XX_T$	$YY_C$	$S_{BA}$	$XX_C$	$YY_T$	$S_{CB}$	$S_{CA}$	$ZZ_T$	$ZZ_C$
833 MPa	833 MPa	100 MPa	698 MPa	698 MPa	60 MPa	60 MPa	698 MPa	833 MPa

The resulting damage due to projectile impact was the next parameter to be validated against experimental data. The author found that the compression and tensile through thickness strengths,  $ZZ_T$  and  $ZZ_C$  respectively, can be used to control the behaviour of damage, and used the same iterative technique to tune the value of these strength parameters. All numerical parameters can be found in Table 4.3.

The next step was study the sensitivity analysis of the woven composite laminate because it is the starting point before conducting the impact damage simulations.

## 4.9 Sensitivity analysis

### 4.9.1 Mesh Sensitivity

A mesh sensitivity study was performed in order to determine a mesh density for the computational model that would appropriately capture the stress gradients produced by the projectile impact. This study was carried out on a model of a composite laminate fully clamped along two edges and impacted directly at the corner of the other two edges by the projectile at a velocity of  $305E+3$  mm/s. The position of the elements used in this study were along the through thickness of laminate at the corner, which is the same area impacted by the projectile.

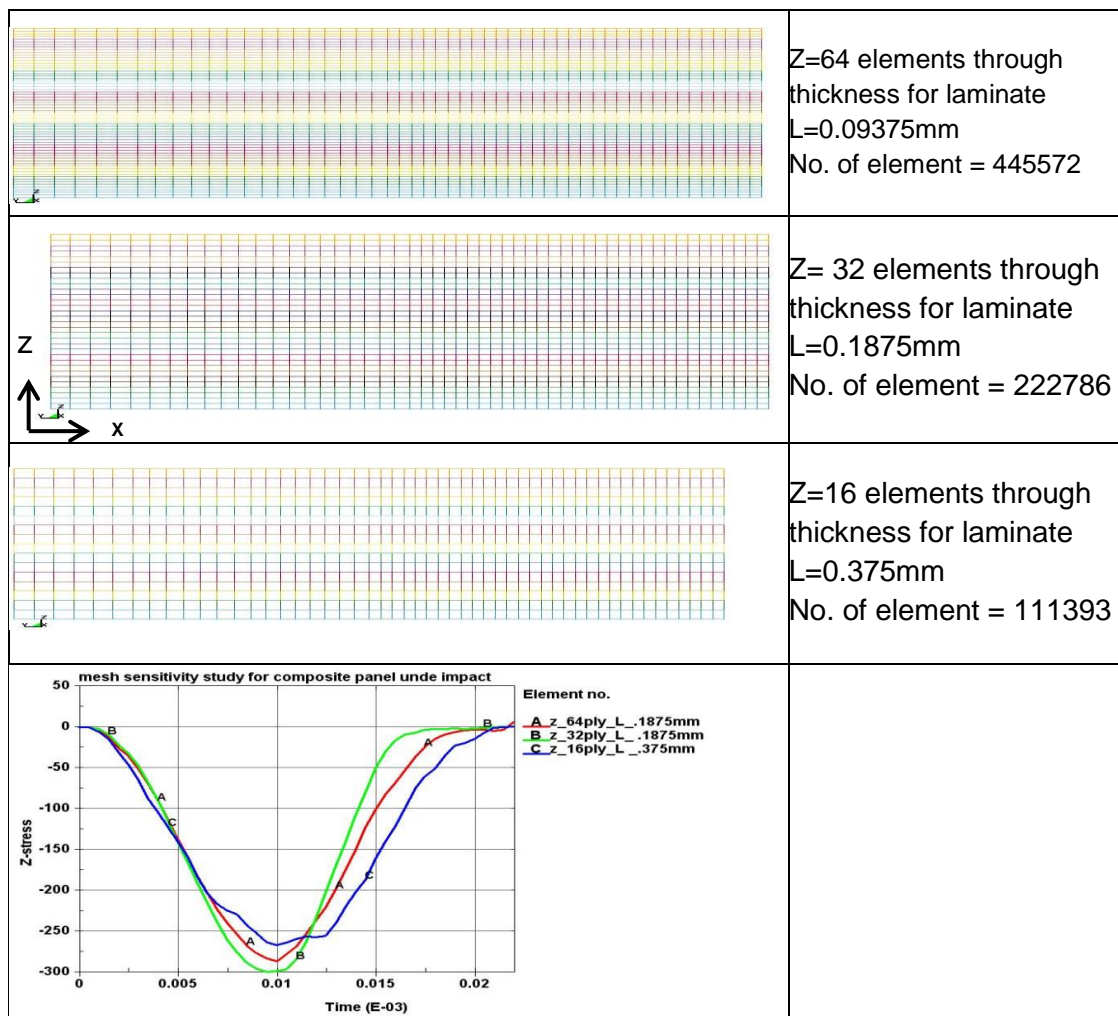
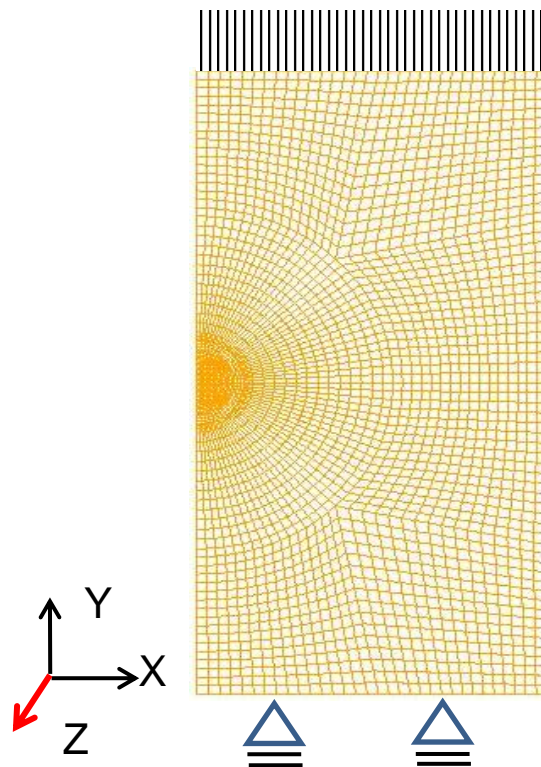


Figure 4. 3 Stress (MPa)-time (sec) curves of the composite laminates for different mesh size.

#### 4.9.2 Geometrical imperfection

Modelling of a composite laminate in numerical method is more accurate in theory than in reality. Therefore, when comparing the results of numerical simulation with the experimental data, some error can be created. To address this issue, the author applied geometrical imperfection analysis to clarify the numerical result. In this analysis, the position of the nodes in the XY-plane, as seen in Figure 4.4 will be changed by  $\pm 10$  percent of the element thickness in Z-direction. The element length in the Z-direction is constant. In this study, the percentage was presented as the No. of elements, which changed with the position over the total elements of the model.



**Figure 4. 4 Uniaxial compressive load.**

Figure 4.5(a) and 4.5(b) show the displacement-force curve obtained under compression loads for sample size 200mm and 100mm respectively. The Figure 4.5(a) and 4.5(b) show that there is not a significant effect of imperfection when changing from 0% to 90%.

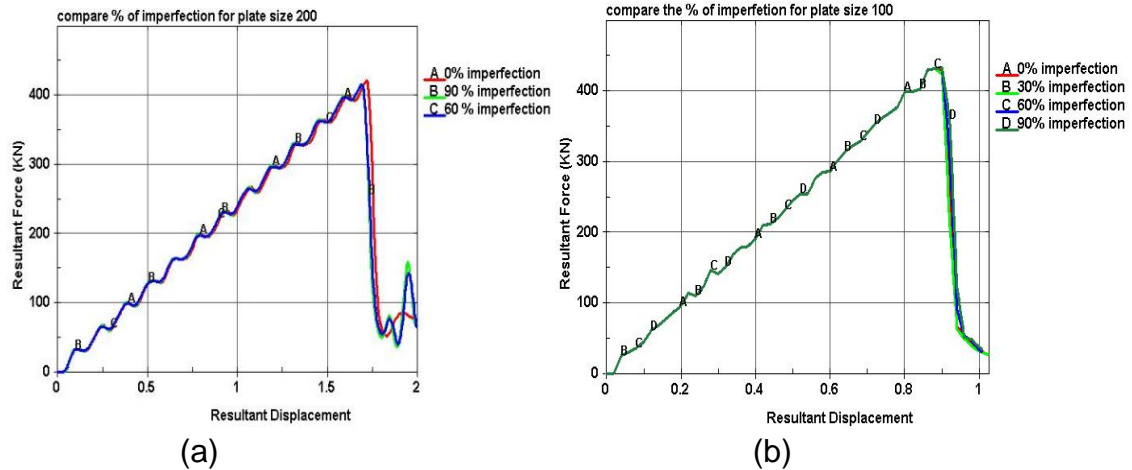


**Figure 4. 5 Force-displacement (mm) curves of the composite laminates for different imperfection percentage: (a) laminate size 200mm (b) laminate size 100mm.**

#### 4.10 Impact damage simulation

Simulations were performed for composite laminates subject to high velocity impact by spherical projectiles Figure 4.6. The range of projectile velocity is between 100-500 ms<sup>-1</sup>. The model performed well, as the intention of the simulation was not to predict crack propagation and detailed failure, but to produce an estimate of the size of the resulting damage. The results of this simulation which described in chapter 5 show the capability of the methodology to capture the material failure mechanisms during penetration.

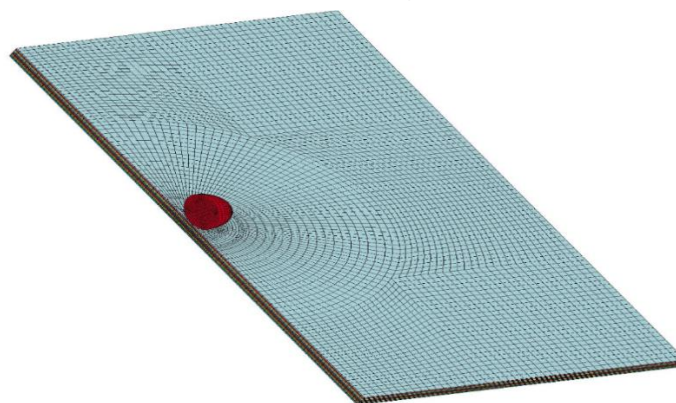


**Figure 4. 6 Finite element model for composite laminate subject to high velocity.**

## **4.11 Numerical Repair Model**

This section focussed on developing a practical numerical methodology to predict the optimum stepped lap joint to repair woven CFRP composite laminate subject to impact damage by using commercial tools. To achieve that a numerical model is developed to predict the compressive failure load of a undamaged, damaged and repaired CFRP composite laminate under static compressive loading. The numerical results of undamaged and damaged composite laminate were compared with the experimental data in to verify the numerical modelling. A stepped lap joint is one of the most efficient joining methods and has a high level of joint strength because the design reduces the stress concentration at the end of overlap. However, this joint affected by different types of failure modes.

### **4.11.1 Stepped Lap Joint Failure Modes**

Failure modes for stepped lap joints can be divided into two main groups, illustrated in Figure 4.7 by (ASTM D5573). The first groups consist of the adherends (composite) failures modes, such as matrix cracking, fibre cracking, or delamination, described in more detail in chapter three. The second group represents adhesive failure modes. The four main, distinct modes of failure of adhesive bond joints are:

- adhesive failure due to a peel load;
- adhesive failure due to a shear load;
- cohesive failure; and
- adherend failure.

Adhesives in a stepped lap joint are more susceptible to failure due to peel and shear stress. The combined normal (peel) and shear stress distributions display high stresses at the overlap ends of the stepped lap, which may negatively affect the strength of the joints. The shear stress of the adhesive controls the failure mode of the stepped lap joint and is principally caused by joint deflections,



rotations, and induced peel stresses, a failure more that often initiates in the adhesive layer at the interface of the adherend and adhesive.

Adhesive failure mode can also be referred to as cohesive failure, or bondline failure - containing either debonding or decohesion of the interface - or a mix of both. The strengths of the bondline for each type of failure mechanism are different and difficult to measure, especially the strength of the adhesive/ adherends interface. However, failure of the stepped lap joint can be minimised by changing the number of steps and adjusting joint length (Matthews et al., 1982; Belingardi et al., 2002; Lchikawa, 2008).

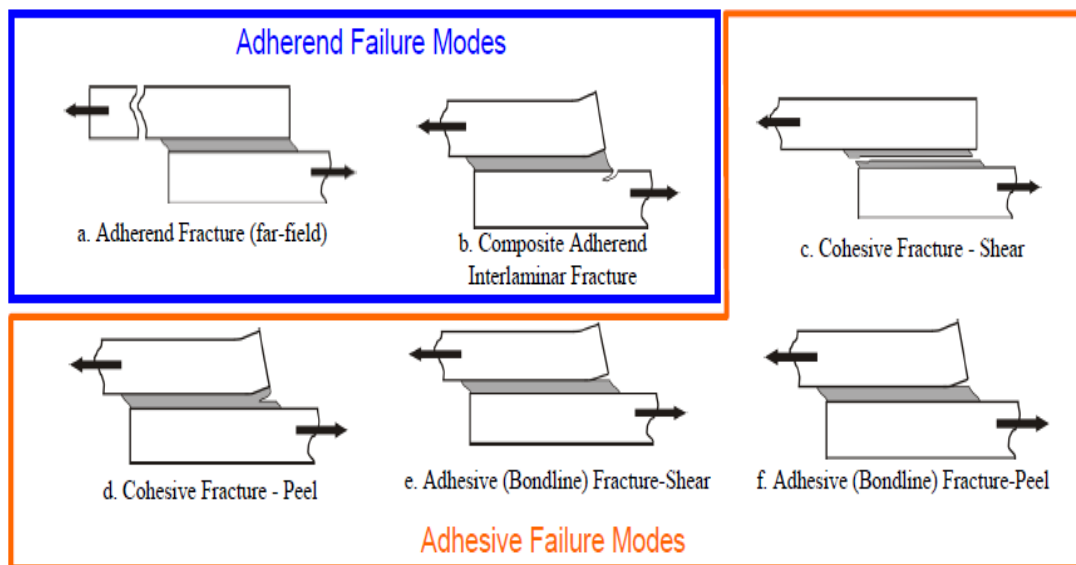


**Figure 4. 7 Failure modes in composite adhesive stepped lap joints (ASTM D5573)**

The stepped lap joints should be designed to minimize peel stress concentrations and maximize shear and compressive stresses, which mean increase the joints strength. Therefore, this study seeks to understand how to minimise steep lap joint failure. Therefore, this study will discuss the best experimental design needed to create the optimal stepped-lap joint by modified the number and lengths of steps on the joint, which can maximise the compressive failure load and compressive strength for repaired CFRP composite laminate.

Moreover, limited resources prevented this study from considering the effect of other parameters on stepped lap joint compressive failure load and strength. Therefore, only one type of adhesive was used, and all joints had the same condition for surface preparation.

In this section a numerical model is developed to predict the behaviour of a repaired CFRP composite laminate under static compressive loading. Thus, the main objective of this section was to create a general program that can be used to model the repaired composite laminates. A simulation guideline for repair of impact damage on composite laminates has been created in this research and includes many key factors as shown in Figure 4.8.

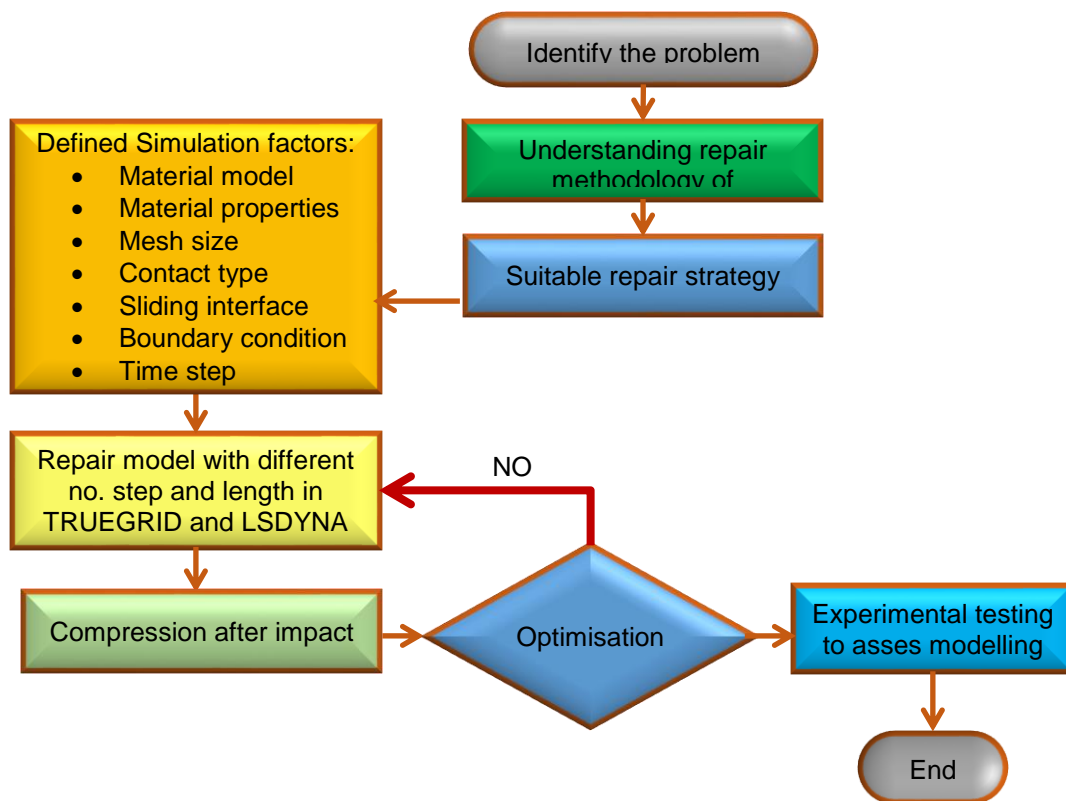


**Figure 4. 8 The simulation guideline for repairing strategy of impact damage.**

In this section, (LS-DYNA) and TrueGrid software were used as commercial tools to model and provide further understanding of the behaviour of repaired CFRP

composites under a compressive load. Failure mode, failure load, and strength of the repairs will be considered. A stress analysis will be performed to identify the critical regions of the repair structure that lead to damage initiation.

#### 4.11.2 Material properties

Different material models for different parts of the model that satisfy the behaviour of the materials were chosen. The parent and joint material properties used in this study were detailed in Chapter 3, Section 3.8.3. The 4.125mm and 2.625mm thick CFRP laminates were made from 11 plies and 7 plies, respectively, and Hexcel G0926 Carbon Fabric 5 harness 6K, Areal Wt 370 gsm. The resin used was Hexcel RTM 6, cured for 1 hour and 40 minutes at 180 C and at a pressure of 100 psi. The plate dimensions is 100X150mm for each side.

The first laminate had 11 layers, using the following stacking sequence: [(0/90); ( $\pm 45$ ); (0/90); ( $\pm 45$ ); (0/90); ( $\pm 45$ ); (0/90); ( $\pm 45$ ); (0/90); ( $\pm 45$ ); (0/90)], for a total thickness of 4.125 mm. The second pane had 7 layers, using the following stacking sequence: ( $\pm 45$ ); (0/90); (0/90); ( $\pm 45$ ); (0/90); (0/90); ( $\pm 45$ )], with a thickness of 2.625 mm. The density of the CFRP material was  $1.5129200E-3 \text{ g/mm}^3 \pm 1.0E-5 \text{ g/mm}^3$ . This adherend was modelled using MAT59 (\*MAT\_COMPOSITE\_FAILURE\_SOLID\_MODEL).

**Table 4. 4 Material parameters for adhesives (Kim et al.2006).**

Young Modulus (MPa)	2600
Yield strength (MPa)	40
Tangent strength (MPa)	50
Poisson's Ratio	0.38
Density (gm/mm <sup>3</sup> )	0.8790E-3

The adhesive material used in this study is Hysol EA9309.3NA because it has a higher load failure level, as shown in Figure 4.9. It was modelled using MAT24 (\*MAT\_PIECEWISE\_LINEAR\_PLASTICITY). The adhesive material thickness is approximately 0.375mm, and the adhesive properties are described in Table 4.4.

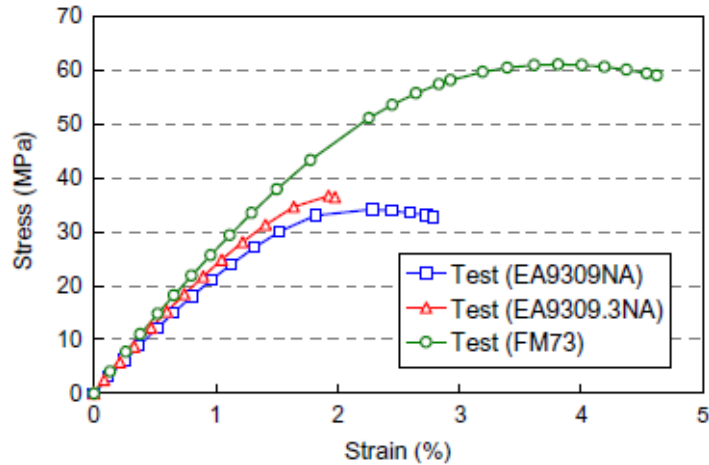


**Figure 4. 9 Stress level vs. strain results of the adhesives material (Kim et al. 2006).**

As has been stated, numerical modelling of adhesives with solid elements can provide a good prediction of the mechanical behaviour of adhesively bonded joints. The failure criterion for the adhesive is based on the maximum plastic strain. Adhesive material is the most critical aspect of this simulation. Therefore, to understand the joint and adhesive material behaviour, the single lap joints has been modelled as described in Kim et al. (2006) and shown in Figure 4.10.

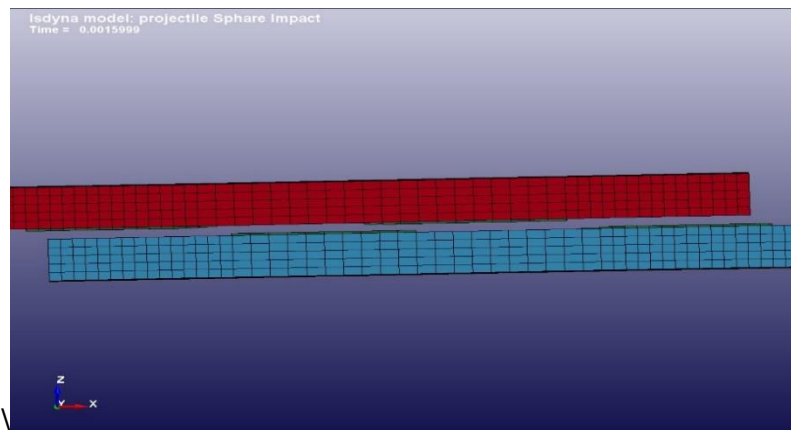


**Figure 4. 10 Single lap joint model.**

This model validates the experiment and results as shown in Figure 4.11. In the Figure 4.11, the simulation of the load displacement curve of a single lap joint has significant agreement with experimental result presented in Kim et al. (2006), as one can see by looking at how the load was raised to 13500N then sharply

decreased to zero. The failure load for adhesive material Hysol EA9309.3NA was 13.5 KN.

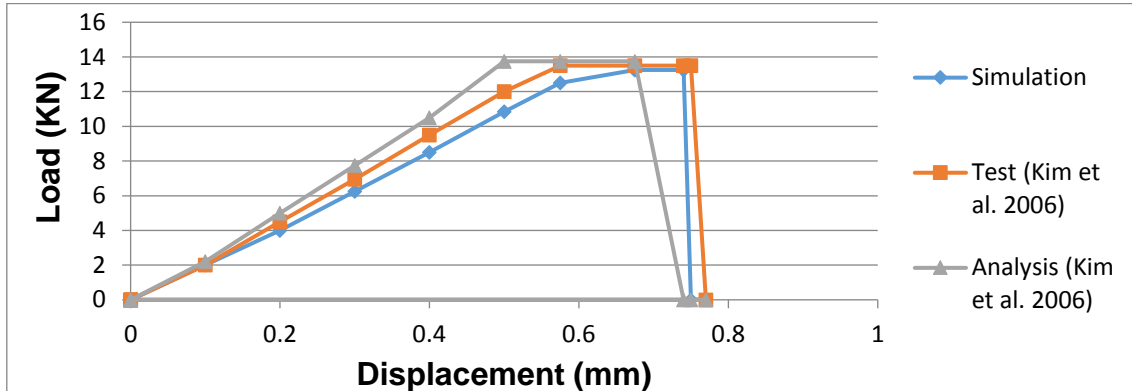


**Figure 4. 11 Simulation and test load–displacement curve for EA9309.3NA adhesive material (Kim et al. 2006).**

#### 4.11.3 Adhesive Mesh Sensitivity

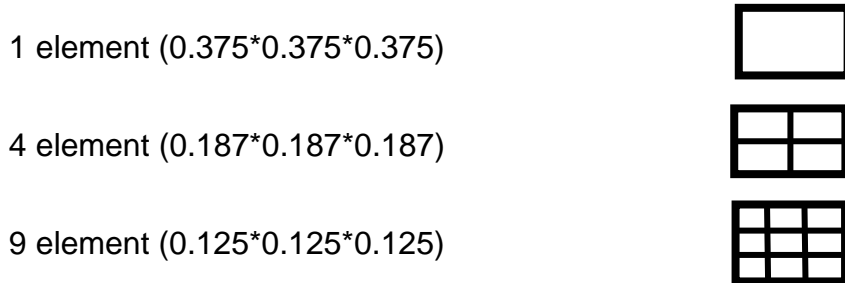


**Figure 4. 12 Adhesive element size.**

The second step of this study concerns an analysis of adhesive mesh sensitivity on the model, which started with one element size (0.375\*0.375\*0.375mm, respectively), and then decreased to (0.125\*0.125\*0.125) mm as shown in Figure 4.12. Figure 4.13 compares the load via displacement for different sizes of element, which were presented in a model with element size (0.187\*0.187\*0.187mm, respectively), which is more accurate and decreases time costs.

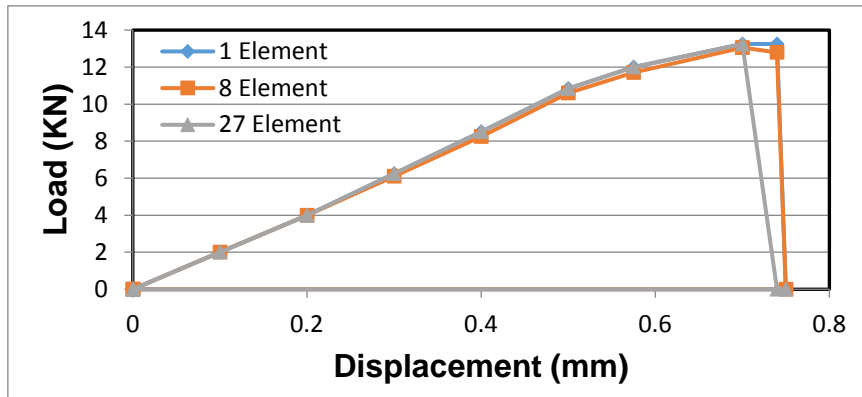


Figure 4. 13 Force-displacement for different sized element.

#### 4.11.4 Contact

The third step analysed the different types of contact between adhesives and joints. Figure 4.14 shows a force-displacement curve for tiebreak contact, tied contact and test Kim et al. (2006), can see that there are slightly different between the tiebreak model and the tied contact model.

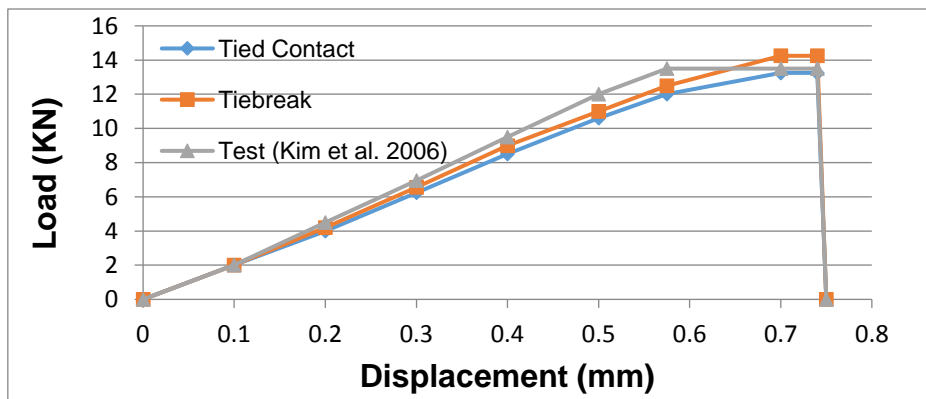
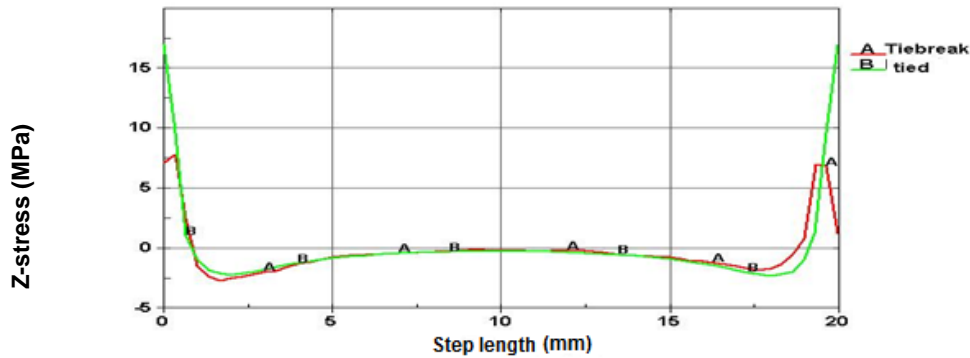


Figure 4. 14 Force-displacement curve for tiebreak contact and tied contact.

Figure 4.15 shows the behaviour of shear and peel stress along the bond line of a joint for both contact models, and shows the behaviour of tied contact and the tiebreak contact was similar. However, due to the number of properties necessary to create the tiebreak. In this model the adhesive and joint are connected by tied contact interfaces.



**Figure 4. 15 Stress-adhesive length curve for tiebreak contact and tied contact.**

The next step was modelling the complex model that goes into the repair of CFRP composites through the use of a stepped lap joint.

#### 4.11.5 Mesh and boundary conditions

The modelling of the geometry of repaired CFRP composite laminate was done via the TRUGRID program. This geometry model was modelled in three steps as detailed in Appendix (C): the first step modelled the outer repair area (parent part); the second step modelled the hole area (joint part); and the third step modelled the step area including the adhesive parts. The number of steps ( $n$ ) can be defined as the number of horizontal length of step; length of steps ( $L$ ) and hole radius ( $r$ ) are variables and remain parameters defined in below:

Step high ( $h$ ) for repaired composite laminate (4.125 mm)

( $n = 3$   $\rightarrow$   $h_1 = 1.125 \text{ mm}$ ,  $h_2 = 2.25 \text{ mm}$  and  $h_3 = 3.375 \text{ mm}$ ) and

( $n = 4$   $\rightarrow$   $h_1 = 0.75 \text{ mm}$ ,  $h_2 = 1.5 \text{ mm}$ ,  $h_3 = 2.25 \text{ mm}$  and  $h_4 = 3 \text{ mm}$ )

Step high ( $h$ ) for repaired composite laminate (2.625 mm)

( $n = 3$   $\rightarrow$   $h_1 = 0.375 \text{ mm}$ ,  $h_2 = 1.125 \text{ mm}$  and  $h_3 = 1.875 \text{ mm}$ ) and

( $n = 2$   $\rightarrow$   $h_1 = 0.75 \text{ mm}$ ,  $h_2 = 1.5 \text{ mm}$ )

Adhesive thickness ( $D$ ) = 0.375mm

Total repaired composite laminates thickness ( $TAD$ ) = 4.125 mm and 2.625 mm

Total repaired composite laminate length ( $Tall$ ) = 150 mm

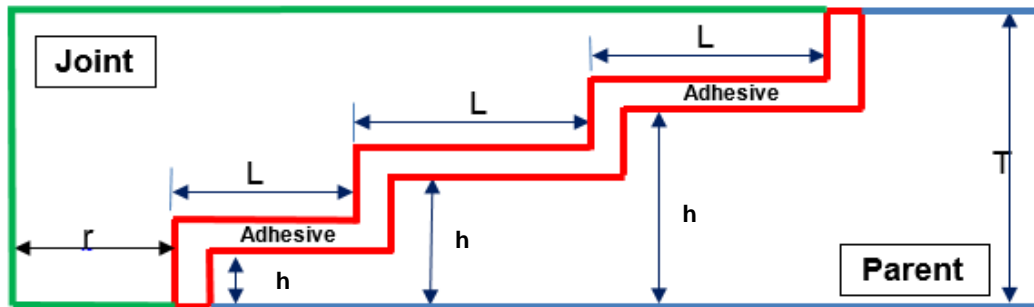


**Figure 4. 16 Height and length of each step (n=3). Total repaired composite laminate thickness = 4.125mm, length (Tall) = 100 mm and adhesive thickness (D) = 0.375mm. h1=1.125.**

Figure 4.16 describes the three step repaired laminate and represents the method used to define the heights and length of each step. The length of the steps depends on the radius of the damage area and number of steps, as shown in equations 4.41 and 4.42

$$TR1 = r * TR \quad (4.41)$$

$r$ : radiuses of damage area and  $TR = 1,2,3,\dots,5$

$$L_i = \frac{TR1}{n} \quad (4.42)$$

$L_i$ : Step length  $i = 1,2,3,\dots,n$  and  $n$ : number of steps

The height of each step was calculated by dividing total thickness of the laminate by the number of steps, as described in the following equation (4.43)

$$h_0 = 0$$

$$h_i = \left(\frac{TAD}{n+1}\right) + h_{(i-1)} \quad (4.43)$$

TAD : laminate thickness

$h_i$  = step high  $i = 1,2,3,\dots,n$

$n$  : number of steps



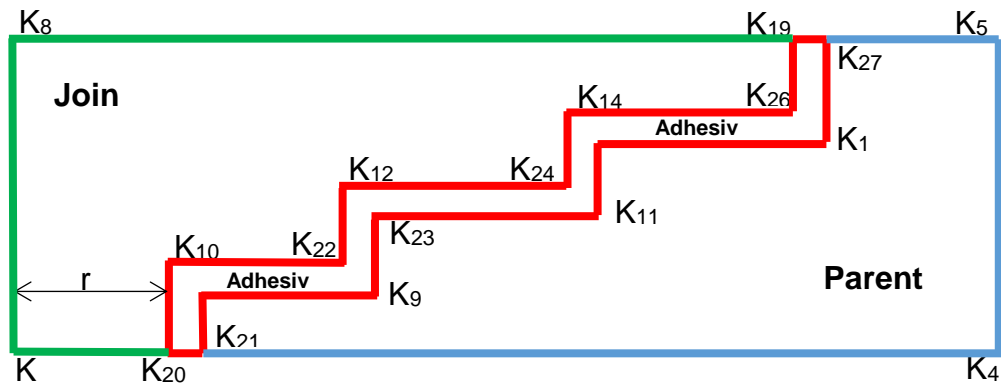


**Figure 4. 17 Critical points in each step.**

The outer boundary and tip of steps has been defined as critical points in this model as described in Figure (4.17). These points have been used to control length, height, and the number of steps. After defining the critical points the model used these points to modelling the composite laminate. However, to homogenise the mesh in applied load area, partition methodology was used.

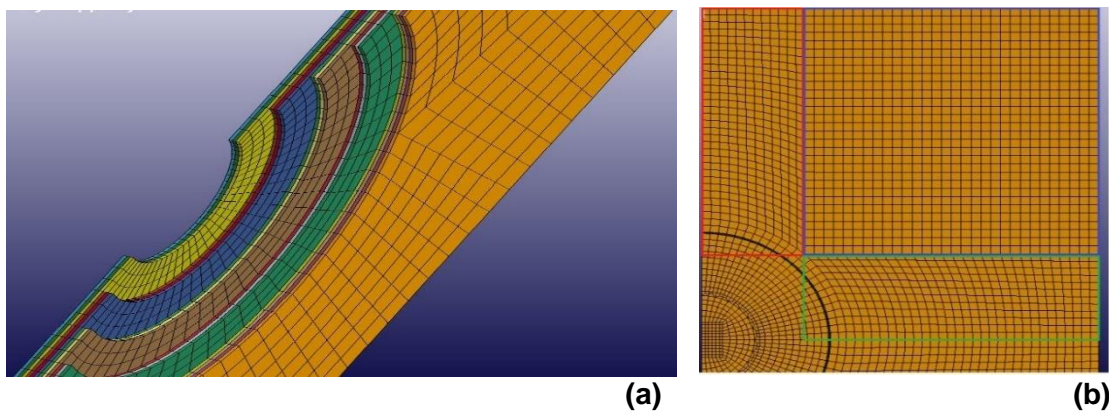


**Figure 4. 18 Complete FE model for the parent part (a) side view & (b) top view.**

This methodology divides the model area into a steps area and an outer damage area (outer hole area). The outer damage area was modelled in cylinder part (near to step) and three rectangle (block) parts (near to outer boundary) with a sphere projection method for the inside boundary of the block, as shown in Figure 4.18(a) and 4.18(b). However, the inside boundaries for the rectangle part (block) have been defined by used follow expression  $((K_{31} + 3) * \cos 45)$ , and were then projected onto the sphere. The main factor in this part of the model was

maintaining the aspect ratio for the element less than five. The step area was modelled using the sphere projection method and the transition block boundary interface technique (reduction element number), which reduced the number of elements to minimise the time cost. Figure 4.19 shows the quarter step area, including joint area, adhesive area and parent area, which is presented via the transition technique.

Steps area included different parts such as joint, parent and adhesive. These parts have been modelled by using cylinder part. The logic statement was choosing to model this area and the minimum and maximum steps high depended on the number of step. The step area was a critical area because most failure in repaired composite laminates occurs in the area between the adhesive and other material. Therefore a mesh sensitivity study for element size in this area and study suitable contact method between adhesive parts and other parts was described in the previous section. The results from these studies shown that the best element size is  $(0.187*0.187*0.532)$ , shown in Figure 4.19.

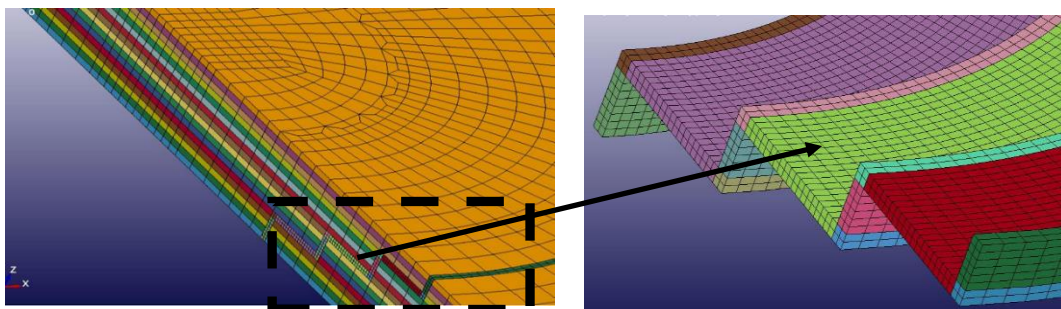


**Figure 4. 19 Step area including joint area, adhesive area and parent area.**

This model uses two methods to define the contact algorithm, the first method is tied contact, which is more realistic than other contact methods and applied between adhesive parts and other parts (joint and parent) due to differences in the mesh size. The second method used normal contact (normal merge) between all parts in the joint and parent area. Element size of both sides of the contact area in the joint and parent area was similar to avoid any errors in the methodology.

One of the most critical practises in this kind of contact is defined the sliding interface method. To define this method necessary to defined the surfaces in contact area. There are many methods can be used to defined that surfaces such as single surface for every contact or one surface for all contact. When applied the first method, the thirty eight surfaces need to be defined, which make the model complicated. Therefore, was decided to use the two surfaces method to make this model simple. The first surface defined as contact between adhesive area and parent area and the second surface defined as contact between adhesive area and joint area as shown in Figure (4.20). The adhesive surface sign as slave and other surfaces (joint and parent) sign as master.

This stage uses a completely geometric model of the repaired composite laminate. The Truegrid output file has been used in LSDYNA to create a LSDYNA input file, which includes geometry modelling, contact algorithm, boundary conditions, and parameters of joint, parent, and adhesive material. The number of elements in this model depends on the number of steps and the step length, in some cases nearly 181,000 elements.

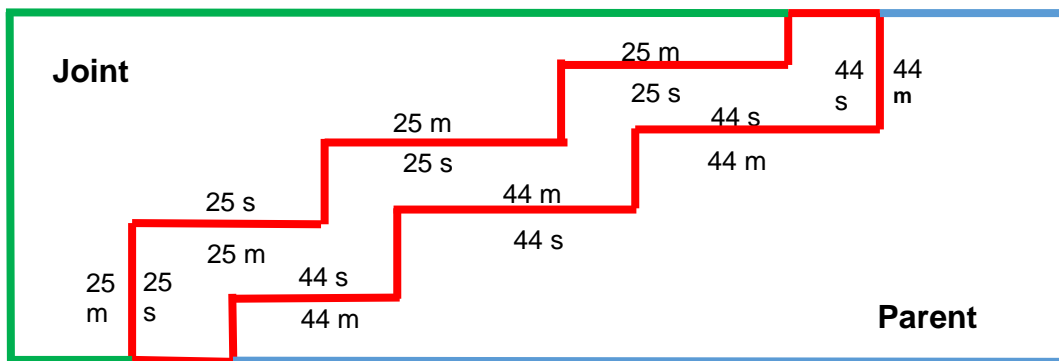


**Figure 4. 20 Sliding interface surface.**

Most of the parameters in the above LS-DYNA input file were described in previous sections. However, this chapter added tied contact (TIED\_SURFACE\_TO\_SURFACE) and new material model (MAT\_PIECEWISE\_LINEAR\_PLASTICITY) for adhesive material.

This study has used optimisation method in order to design optimal stepped lap joints for use in repairing CFRP composite laminates. The number of steps and step length have nominated as the most critical areas in stepped lap joints. Therefore, this study has used these parameters as main criteria in the optimisation method.

#### 4.12 Optimisation method

The optimisation method criteria applied in this study seeks to maintain the assumptions described in Chapter 1. The first CFRP composite laminate (thickness 4.125 mm) applied the following optimisation criteria: the number of steps must be considered in two levels. The first level has three steps and the second level has four steps, shown in Figure 4.21. The total overlap length was applied as a fourth level: the first level total overlap length equalled the radius of the damage area (12 mm); the second was 24 mm; the third level was 36 mm.

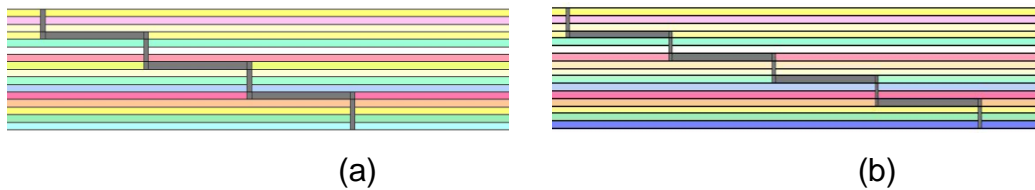


**Figure 4. 21 Number of steps (a); three steps; (b) four steps.**

The second CFRP composite laminate (thickness 2.625 mm) applied the following optimisation criteria: the number of step was considered in two levels; the first level has two steps and the second level has three steps, as shown in Figure 4.21. The total overlap length was applied as a three level: the first level total overlap length equalled the radius of the damage area (12 mm); the second was (24 mm) and the third level was (36 mm).

To design an optimal stepped lap joint in a repaired CFRP composite laminate, this study used the design of experiments. The automated method for design optimal stepped lap joint in repaired CFRP composite laminate will be part of future study. In this method has been study different case study and then

compare the load and strength results of these case studies to find the optimal stepped lap joint in repaired CFRP composite laminate.

#### 4.12.1 Design Experiments

In the cases of two different thickness repaired composite laminates studied, the number and length of steps have been considered as variable parameter in this method, as described in previous section.

##### 4.12.1.1 Repaired composite laminate (4.125 mm)

The numbers of steps are established according to the composite thickness, for practical manufacturing reasons. Therefore, the numbers of steps studied in this case were three and four. Table 4.5 presents the configuration of three steps with different joint lengths. Table 4.6 presents the configuration of four steps with different joint lengths.

**Table 4. 5 The configuration of three steps with different joint lengths.**

Number of Step	Case Number	H1	H2	H3	L1	L2	L3
3	L3TR1	1.125	2.25	3.375	4	4	4
	L3TR2	1.125	2.25	3.375	8	8	8
	L3TR3	1.125	2.25	3.375	12	12	12

**Table 4. 6 The configuration of four steps with different joint lengths.**

Number of Step	Case Number	H1	H2	H3	H4	L1	L2	L3	L4
4	L4TR1T4	0.75	1.5	2.25	3	3	3	3	3
	L4TR2 T4	0.75	1.5	2.25	3	6	6	6	6
	L4TR3 T4	0.75	1.5	2.25	3	9	9	9	9

#### 4.12.1.2 Repaired composite laminate (2.625 mm)

In this case, due to the thickness of the laminate and the manufacturing reasons, it was decided to study three steps in this type of laminate. Table 4.7 presents the configuration of three steps with different joint lengths.

**Table 4. 7 The configuration of three steps with different joint lengths.**

Number of Step	Case Number	H1	H2	H3	L1	L2	L3
3	L3TR1 T2	0.375	1.125	1.875	3	3	3
	L3TR2 T2	0.375	1.125	1.875	6	5	6
	L3TR3 T2	0.375	1.125	1.875	12	12	12

After modelling the repaired composite laminate with different numbers of step and overlap length, a non-linear static simulation (Compression after Impact) with an adopted model is performed using Lsdyna to define the optimal stepped lap joint in repaired composite laminates, which will be discussed in the next section.

#### 4.13 Compression after Impact

The numerical model for compression after impact (CAI) tests was performed to study the behaviour of undamaged, damaged and repaired composite laminates as shown in Figure 4.29. This model used to assess the failure load of composite laminates which have been impacted and repaired. The Compression after

impact simulations are performed with LSDYNA using an explicit solver. The 8-node solid elements were used in this model and due to the symmetry assumption the laminate was modelled as half specimen.

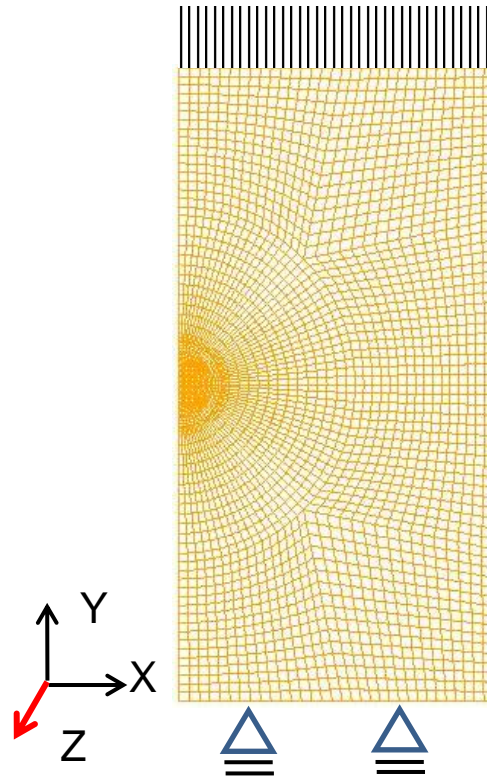


**Figure 4. 22 Boundary conditions of the CFRP composite laminate.**

The boundary condition of the model was clamped at one end and the load was applied to another end in y-direction as shown in Figure 4.22. To reduce time cost the velocity of applied force increased to 300 mm/sec. The geometries of stepped lap joint were modelling in previous section according to the case studies of Design Experiments method also considered in this analysis. The material parameters used in this simulation have been detailed in previous section.

# **Chapter 5**

## **Result and Discussion**

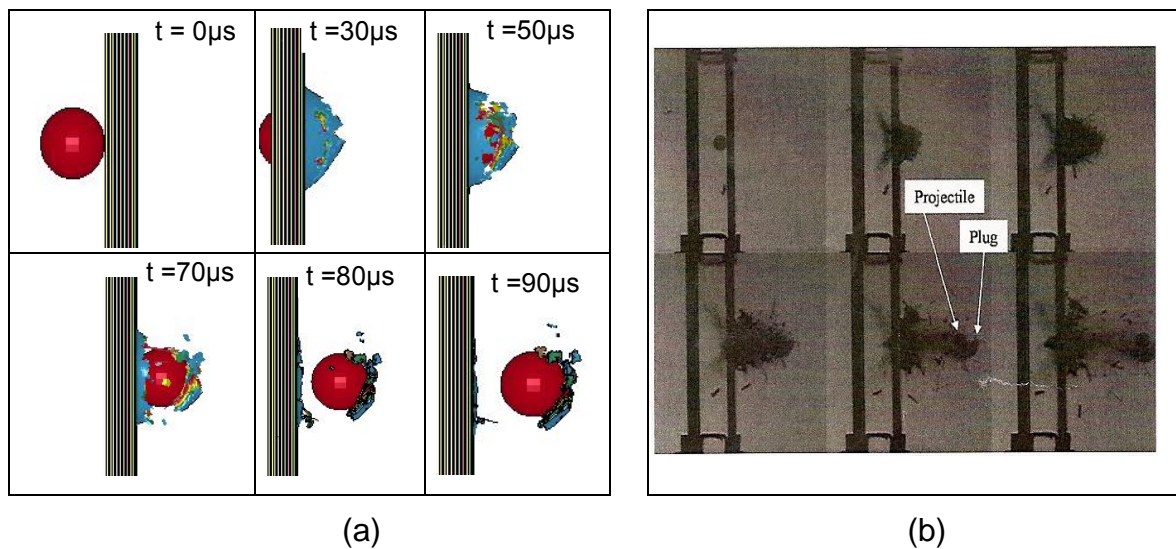


## 5.1 Introduction

Result of impact damage experiments and numerical simulation of CFRP composite laminates subject to high velocity impact and the result of compression after impact experiments and numerical simulation of unrepaired CFRP composite laminate included damaged (impact damage), undamaged and repaired CFRP composite laminate was described in this chapter in order to defined the optimum joint to repair the damaged (impact damage) CFRP composite laminate.

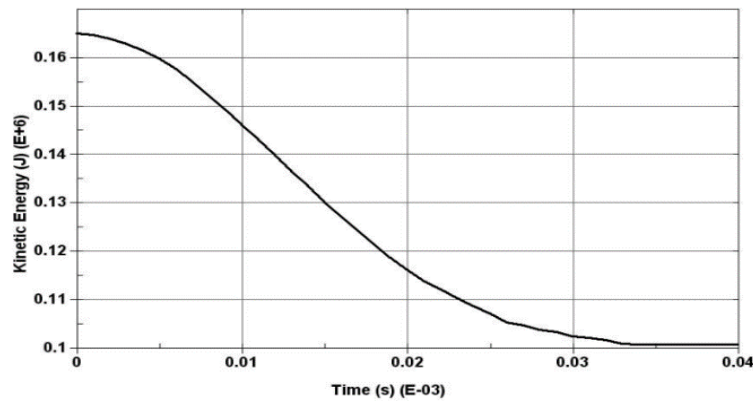
## 5.2 Impact damage simulation

Numerical modelling were performed for composite laminates subject to high velocity impact by spherical projectiles. The range of projectile velocity is between 100-500 m/s. When the projectile penetrates the laminate, significant damage occurs, including delamination, compression through thickness failure, out-of-plane shear failure and in-plane tensile failure of the fibres located at the rear surface, where high tensile stresses develop as shown in Figure 5.1 (a).



**Figure 5. 1 Penetration of 6 mm CFRP laminate by a 12mm diameter steel sphere projectile with velocity of 354 m/s: (a) simulation and (b) experimental (Hazell et al., 2008).**

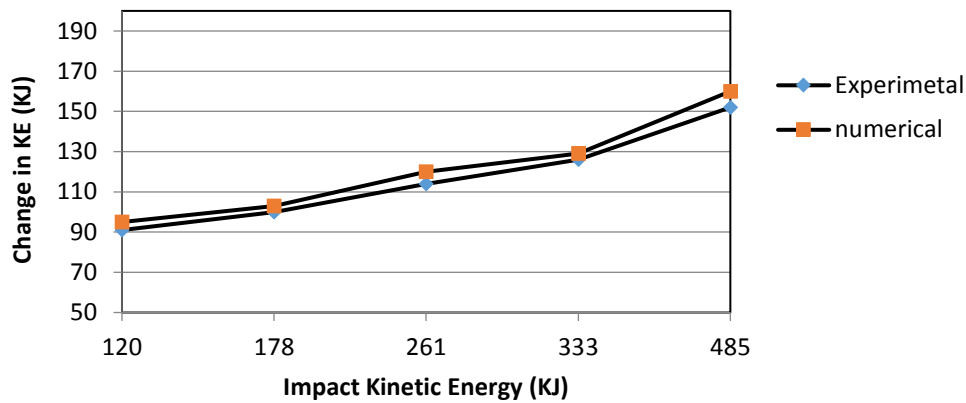
Figure 5.1 shows a comparison between the experimental and simulation results for the penetration of the specimen at an impact velocity of  $354E+3$  mm/s. As shown in Figure 5.1(a), once the projectile impacts the target, fractures initiate immediately in the composite laminate. These fractures occur within  $10\mu\text{s}$ , and the projectile reaches the end of the target after  $20\mu\text{s}$ . A plug is formed and ejected from the back surface at  $50\mu\text{s}$ , and the projectile completes the penetration after  $80\mu\text{s}$ .



**Figure 5. 2 The kinetic energy of the steel sphere projectile after impact 16 layer laminates with velocity =  $354E+3\text{mm/s}$ , showing the kinetic energy (J) versus time(s).**

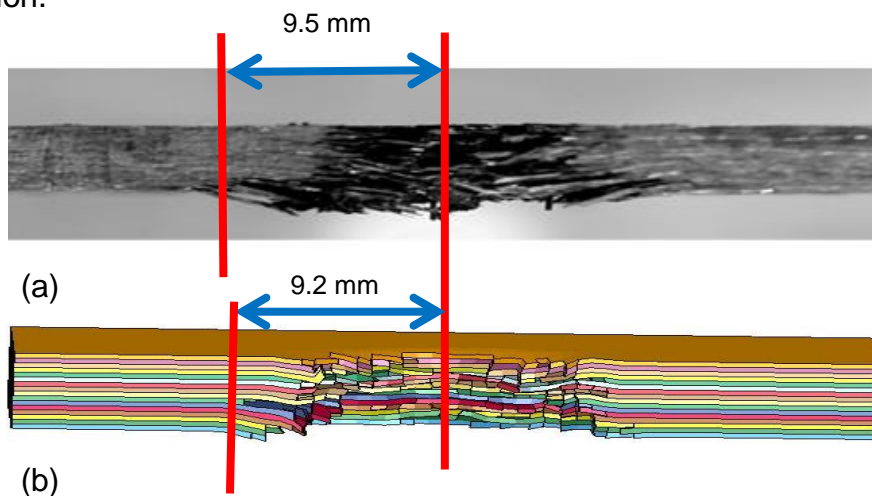
The kinetic energy of the projectile is transferred to the target. Therefore, as shown in Figure 5.2, the kinetic energy of the projectile will be reduced. Damage growth can be attributed to the combination of fibre failure modes. For example, the fibre crush provides high resistance to penetration, which is shown in Figure 4.8 as the resulting decrease of kinetic energy from 0 to  $0.035\text{s}$  (E-03). The period from  $0.035\text{s}$  (E-03) onward represents the complete penetration and formation of the plug, which then travels at a constant velocity. The Figure 5.2 represents half of the system energy due to the symmetry assumption.

Figure 5.3 shows the variation of the change in kinetic energy versus the initial impact kinetic energy. The Figure 5.3 also compares the experimental and the simulation results for the change in kinetic energy. It can be seen that the results significantly matched in all simulated cases and the absorbed energy was adequately captured.



**Figure 5. 3 The change in kinetic energy of the projectile against the initial impact Kinetic Energy (120KJ=183m/s and 485 KJ = 368m/s).**

The residual kinetic energy is 5.0 % larger than experimental data. This slight difference in the residual kinetic energy of the projectile can be attributed to neglect of the frictional energy of eroding elements surrounding the projectile during penetration, and/or the mesh size may not be refined enough for the penetration.



**Figure 5. 4 The conical shaped hole formed on 6 mm CFRP laminate after impact by a steel sphere projectile velocity of 305m/s: (a) experimental results (Hazell et al, 2008); (b) numerical results.**

The penetration mechanism of the projectile had a “plugging-type” (shear) failure. In this case, transverse shear strength is the predominant strength parameter. The hole that was formed after impact was conical in shape, as shown in Figure

5.4, and the cones that formed varied in size with the kinetic energy of the projectile.

As presented above, the simulation results were validated with experimental results, and the results were significantly similar. Therefore, the author extended the study and applied this simulation program to study the impact behaviour of two CFRP woven composite laminates with different thickness and layup. These woven composite laminates were made of Hexcel G0926 Carbon Fabric 5 harness 6K, Areal Wt 370 gsm. The resin used was Hexcel RTM 6, cured for 1 hour 40 minutes at 180° C at a pressure of 100 psi with an average thickness of 0.375mm.

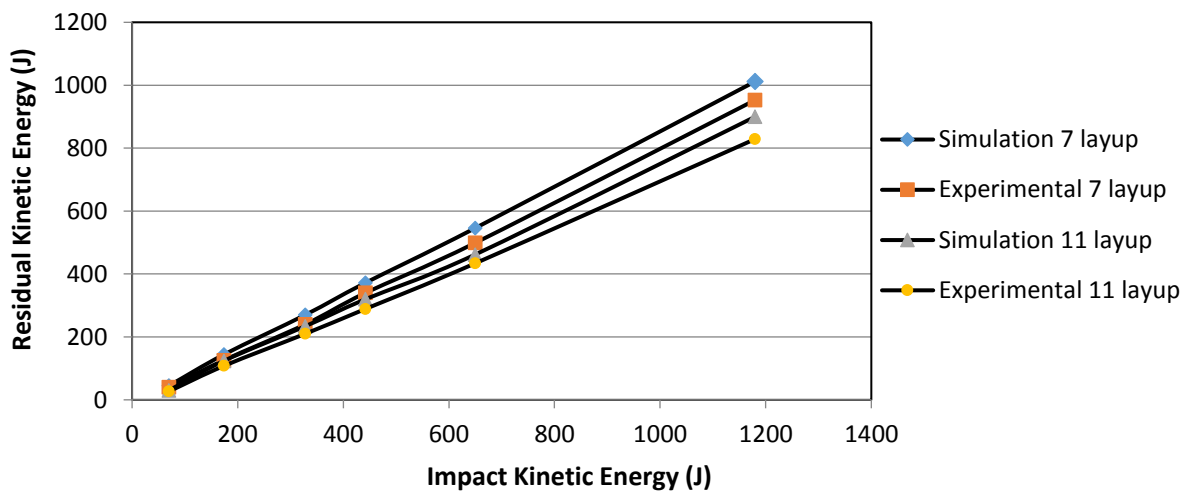


**Figure 5. 5 The numerical residual kinetic energy of the projectile against the initial impact kinetic energy for composite laminates of different thickness (2.625mm and 4.125 mm). (70J=140m/s and 1180 J = 579m/s).**

The first laminate had 11 layers, using the following stacking sequence: [(0/90); (±45); (0/90); (±45); (0/90); (±45); (0/90); (±45); (0/90); (±45); (0/90)], for a total thickness of 4.125 mm. The second pane had 7 layers, using the following stacking sequence: [(±45); (0/90); (0/90); (±45); (0/90); (0/90); (±45)], with a thickness of 2.625 mm. The density of woven CFRP laminates was  $1.512 \times 10^{-3} \pm 1 \times 10^{-6}$  g/mm<sup>3</sup> using a Micrometrics Accupyc 1330 gas Pycnometer (Hazell et al., 2008). The dimensions of the specimens measured 100×150 mm, with a

thickness of 4.125mm, and 100×150 mm by 2.625mm. The composite specimen was secured onto the support frame with clamping at the top and bottom, while the other two edges remained free.

According to the simulation results presented in Figure 5.5, the residual kinetic energy for the projectile after impacting a 2.625 mm CFRP composite laminate is higher than for a 4.125 mm laminate, suggesting that the thicker CFRP composite laminates have more capability to resist the impact energy and increase aircraft survivability.

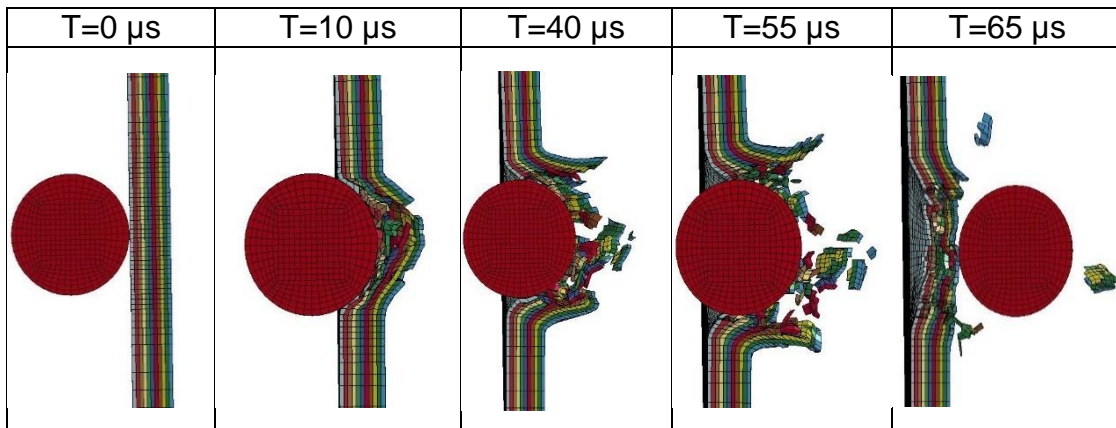


**Figure 5. 6 Penetration of 4.125 mm CFRP laminate by a 12mm diameter steel sphere projectile with velocity of 200 m/s.**

Figure 5.6 shows the numerical behaviour of 4.125 CFRP laminate subject to high velocity impact (200m/s) which show the penetration and fractures initiate in the composite laminate , once the projectile impacts the target. These fractures occur within 10μs, and plug is formed at 40μs, and the projectile completes the penetration after 65μs.

Figures 5.7(a) and 5.7(b) show the failure behaviour of the 11 layered CFRP composite laminate subject to impact energy of 141 J (200 m/s) by the steel sphere projectile. Figure 5.7(a) shows a damaged area with a diameter of about 24mm on the rear surface of the laminate. Figure 5.7(b) shows the front surface of the damaged laminate, where the diameter of the damaged area measures about 15 mm.

The Figures 5.7(a) and 5.7(b) clearly show that the damaged area changed significantly with the projectile velocity through the composite laminate, with the damaged area on the front being smaller than the damaged area at the rear surface (Hazell, et. al., 2008), where a petalling or plug formation was apparent. Moreover, the experimental result used to assess simulation result which shown in Figure 5.7(a) a damaged area with a diameter of about 20mm on the rear surface of the laminate. Figure 5.7(b) shows the front surface of the damaged laminate, where the diameter of the damaged area is about 14 mm.

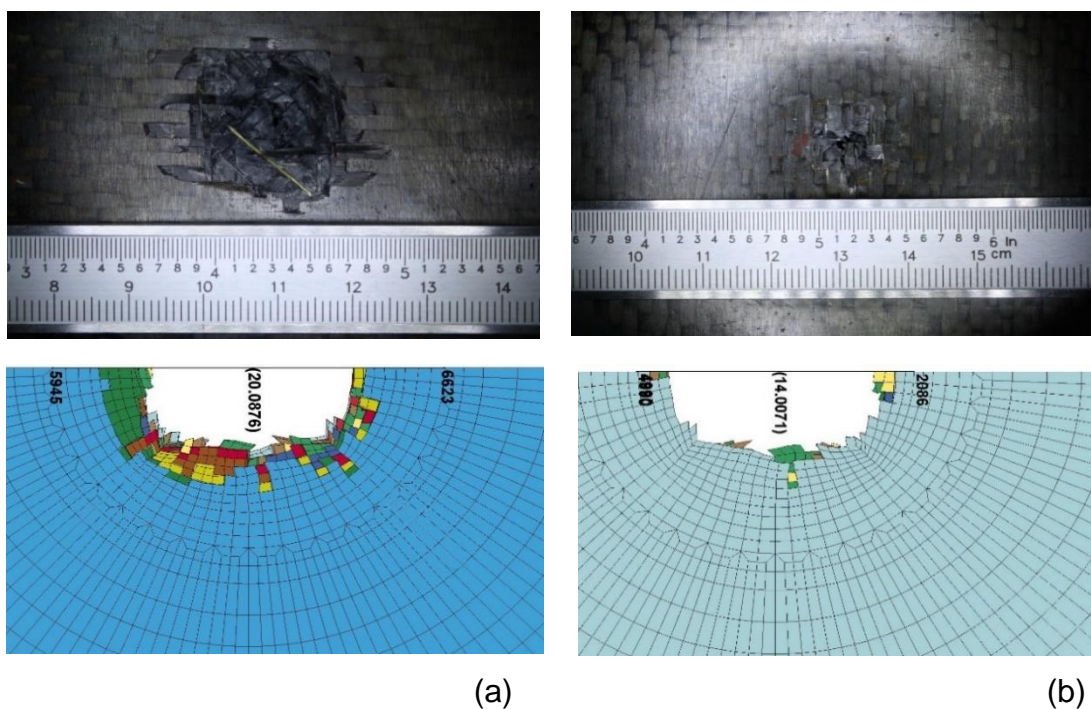


**Figure 5. 7 Impact failure of 11 layered CFRP woven composite laminate impacted at 141 J (200 m/s), (a) rear surface and (b) front surface.**

The numerical results of CFRP composite laminate subject to high velocity impact were validity by experiment test show the capability of the methodology to capture the material failure mechanisms during penetration. The model performed well, as the intention of the simulation was not to predict crack propagation and detailed failure, but to produce an estimate of the size of the resulting damage. Therefore, the next step was extending the numerical modelling to defined the optimum joint to repaired CFRP composite laminate subject to high velocity

impact. The numerical modelling for compression after impact test was performed to define the compressive failure load.

### 5.3 Compression after Impact

Impact damage can be reducing the compressive strength of a composite laminate. Therefore, the compression after-impact (CAI) behaviour of composite laminates is a main concern when restore the strength of composite structures subject to impact damage. Moreover, CAI tests carried out to avoids global buckling of the impacted laminate, so that failure happen as the delamination progresses with the local buckling of the composite laminates produced by impact.

The developed experimental and numerical procedure is used to investigate the behaviour of undamaged, damaged and repaired composite laminates during the compression after impact (CAI) tests as shown in Figure 5.9. This procedure is performed to assess the failure load and residual strength properties of composite laminates which have been impacted and repaired.

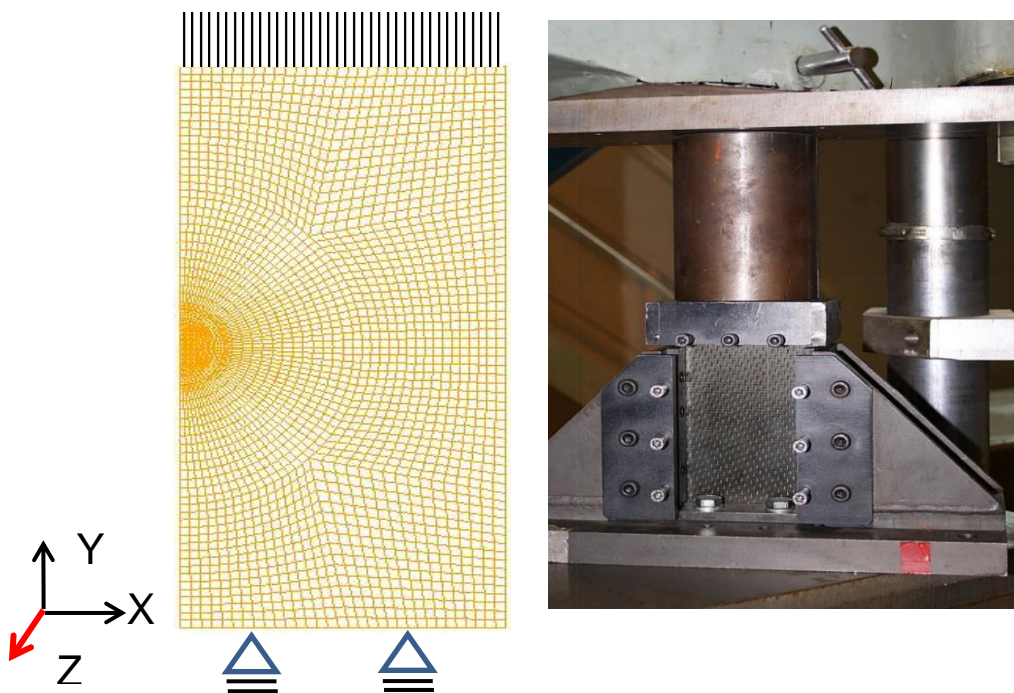


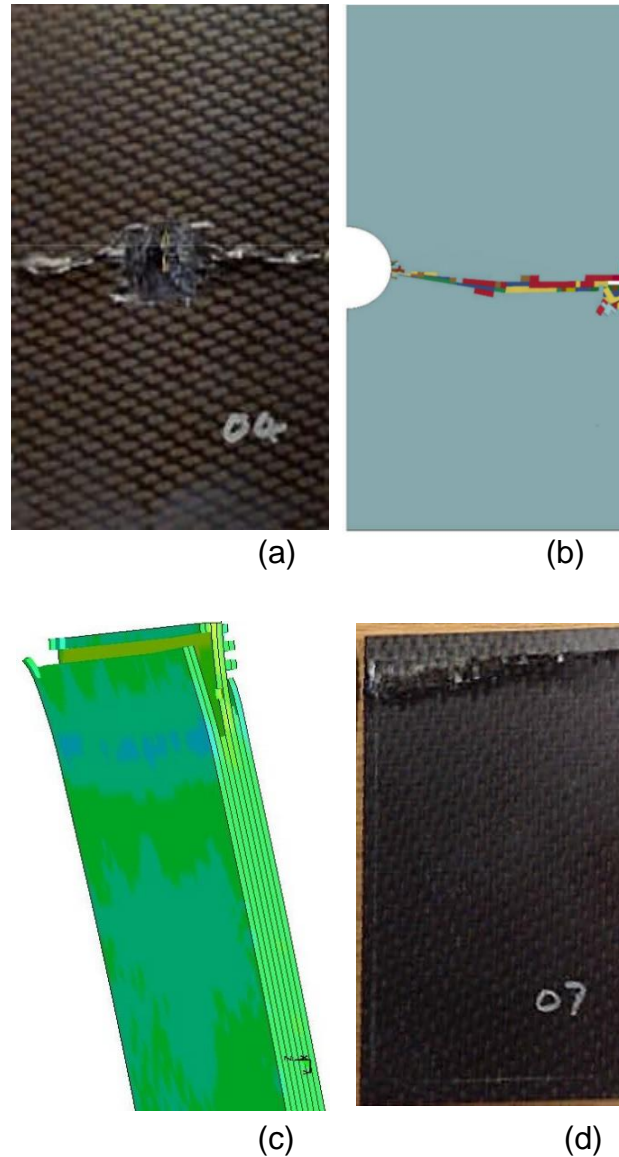
Figure 5. 8 Boundary conditions of the CFRP composite laminate a) FEM and b) Experiment.

The Compression after impact simulations are performed with LSDYNA using an explicit solver. The 8-node solid elements were used in this model and due to the symmetry assumption the laminate was modelled as half specimen. The boundary condition of the model was clamped at one end and the load was applied to another end in y-direction as shown in Figure 5.9. To reduce time cost the velocity of applied force increased to 300 mm/sec. The geometries of stepped lap joint were modelling in previous chapter according to the case studies of Design Experiments method also considered in this analysis. The material parameters used in this simulation have been detailed in previous section.

### **5.3.1 11 Plies CFRP composite laminate**

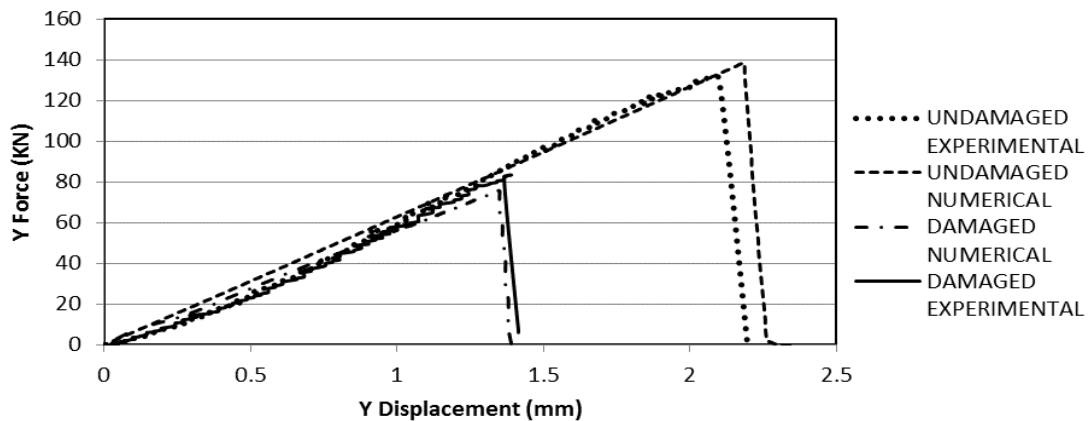
Figure 5.10 shows the failure behaviour of undamaged and damaged CFRP composite laminate with 11 layers. This failure behaviour was predicated because the failure for damaged specimen as seen in Figures 5.9(a) and 5.9(b) happens in the weakest area and simulation. Moreover, experimental undamaged laminate was failed in the same area. The simulation and experimental test for undamaged laminate specimen failed by crushing brooming and both were failed in the same area as shown in Figures 5.9(c) and 5.9(d). Matrix and fiber cracking in undamaged and damaged specimen is the experimentally and numerically detected and cause of final failure under compression loading as shown Figure 5.9





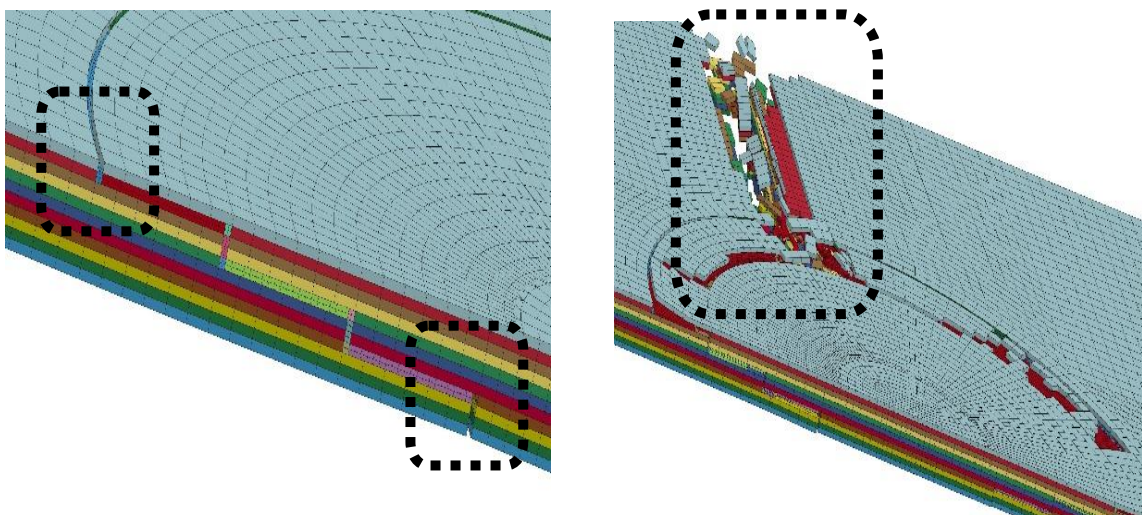
**Figure 5. 9 Compression after impact test of the 11 Plies CFRP composite laminate (a) experimental damaged (b) numerical damage (c) numerical undamaged (d) experimental undamaged.**

Figure 5.10 shows the failure load of undamaged and damaged CFRP composite laminate. The simulation and experimental result of undamaged laminate show the laminates failed at an average of 138 KN. However, damaged laminate failed at 80 KN which significantly reduce when compared to the undamaged panel. Therefore, the average reduction in peak load of 45%.



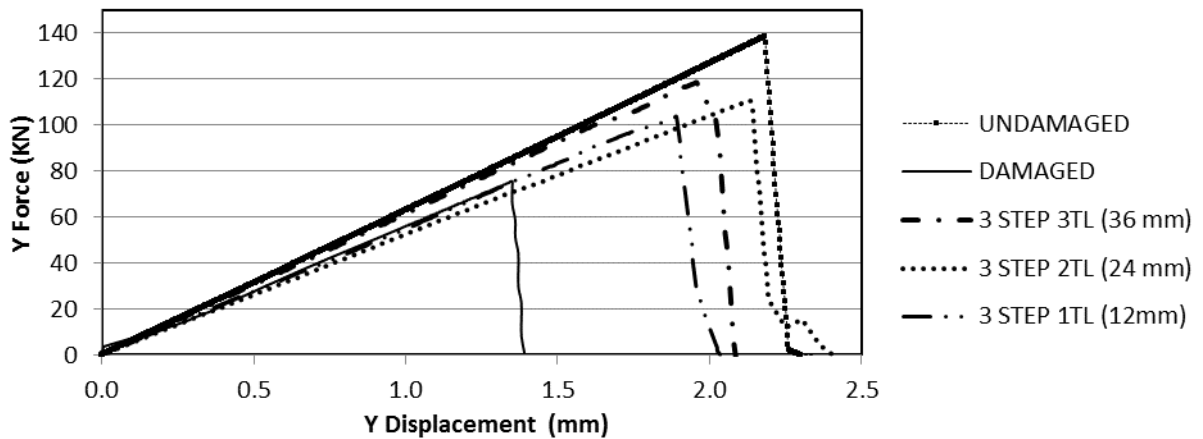
**Figure 5. 10 Failure load versus displacement for undamaged and damaged CFRP composite laminate with 11 plies.**

Figure 5.11 illustrates damage propagation in the stepped lap joint. Relatively the damage starts in the edge of lap joint at adhesive material and in the lower side of specimen which is expected because the stress level in the edge area is higher than other area. Then the delamination is constituent until loading level reaches the failure load. At this level, the fibre and matrix crack is observed around the repair zone and further propagates laterally toward the sides of the specimen which causes ultimate failure within the specimen, as shown in Figure 5.11.



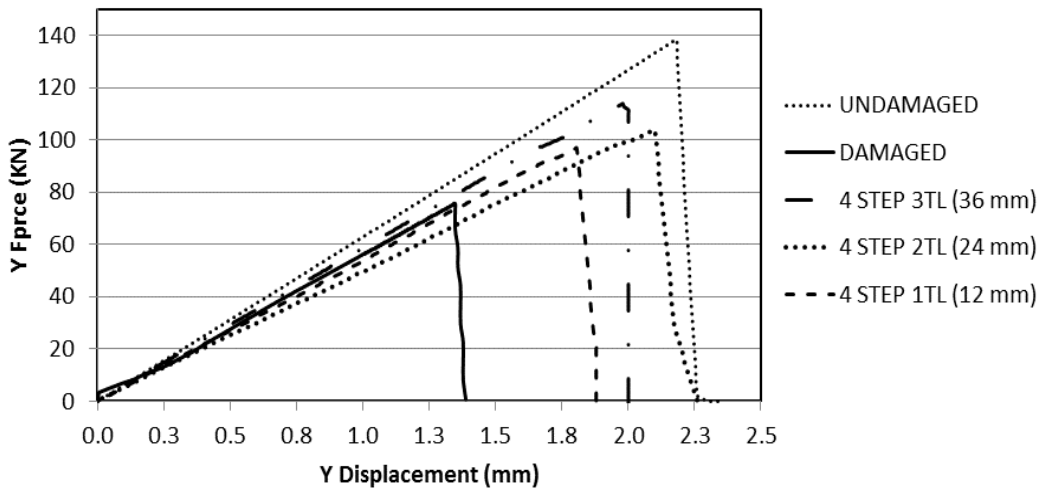
**Figure 5. 11 Numerical compression after impact model of the repaired 11 Plies CFRP composite laminate.**

Figure 5.12 shows the failure load of stepped joints (three steps) for various overlap lengths (TL). The failure loads increase when the total overlap length increases from 12 mm to 36 mm as shown in Figure 5.13 and this behaviour is quite expected. The undamaged laminate failed at an average of 140 KN and damaged laminate failed at a significantly smaller compression load compared to the undamaged laminate, with an average reduction in peak load of 52%. As seen in Figure 5.12 the three stepped lap joint with the three different overlap lengths was able to restore the compression failure load of the damaged laminate to 82% of the undamaged laminate. The compression failure load increases by 14% when the overlap length increases from 24 mm to 36 mm. Therefore, it has been defined the optimal overlap length 36 mm in the three stepped lap joint level.



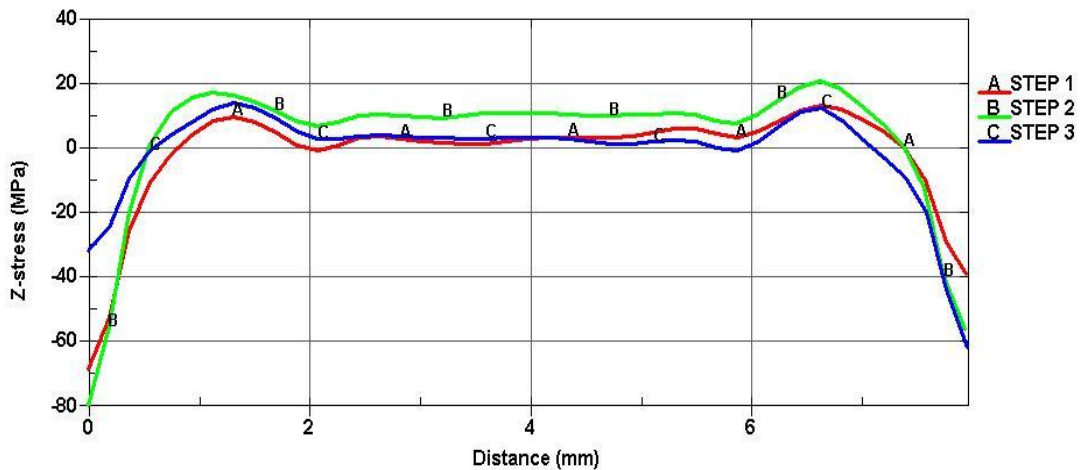
**Figure 5. 12 Numerical analysis on failure load versus displacement for various three stepped lap joint for 11 Plies CFRP composite laminate.**

A compressive failure load versus displacement is shown in Figure 5.13 for the four stepped lap joint with the three different overlap lengths. It is apparent that the compressive failure load of damage laminate is much less than undamaged laminate by 53 %. The compressive failure load for repaired laminate increase by 17 % when the overlap length increase from 24 mm to 36 mm as shown in Figure 5.13.



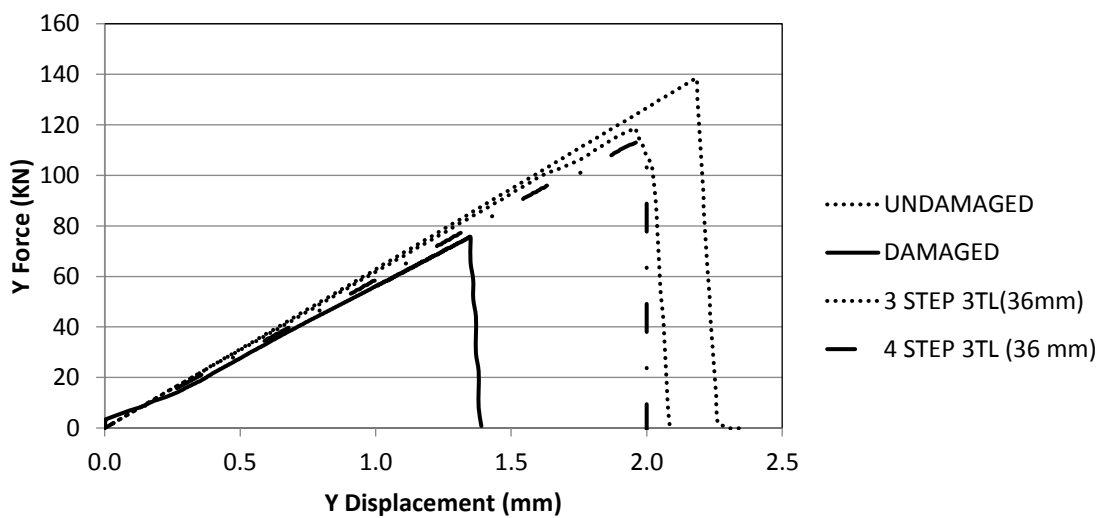
**Figure 5. 13 Numerical modelling on compressive failure load versus displacement for various 4-stepped lap joint with different overlap length.**

Figure 5.14 shows the stress (z-direction) along the path line of mid-surface of various stepped lap joint. The peak stress at the end step explains why failure always initiates at the end step of the bonded region. Two main factors which have been studied in a repaired geometry were number of steps and overlap length. Figure 5.14 shows the overall stress level increases with the increase of overlap length.



**Figure 5. 14 Stress along the path line of mid-surface of the stepped lap joint.**

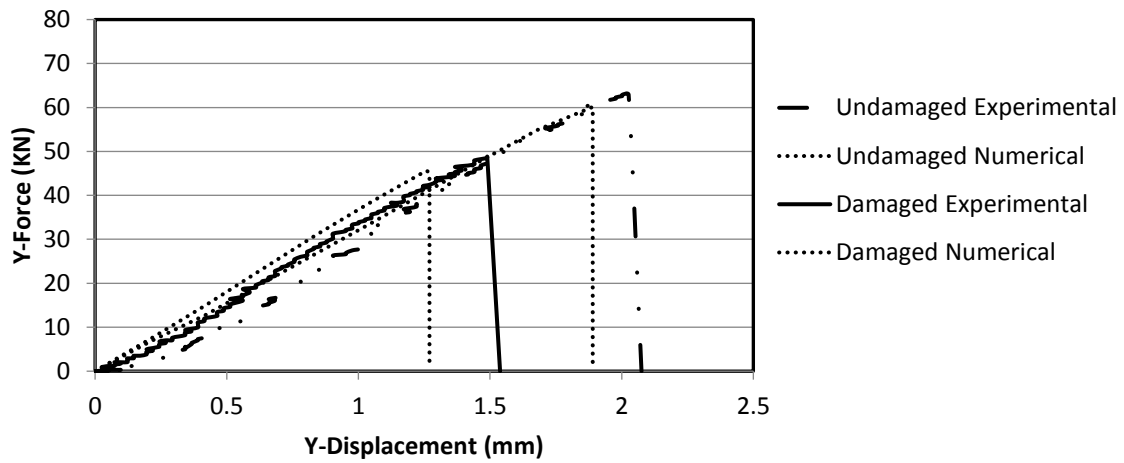
Considering the results presented in Figure 5.15 in terms of repaired methods (number of steps), the maximum failure load is the same for both stepped joints about 120 KN. However, 3 stepped joint showed higher stiffness in comparison with the 4 stepped joint. Therefore, the optimum repair of 11 Plies CFRP composite laminate subjected to impact damage was stepped lap joint with three step and 36 mm overlap length which this result and behaviour is expected. The impact damage reduce the failure load to 75 KN from 120 KN. However, the failure load for optimum joint increase to 120 KN which restore about 90% of original failure load.



**Figure 5. 15 Comparison between undamaged and damaged model with different steps for 11 Plies CFRP composite laminate.**

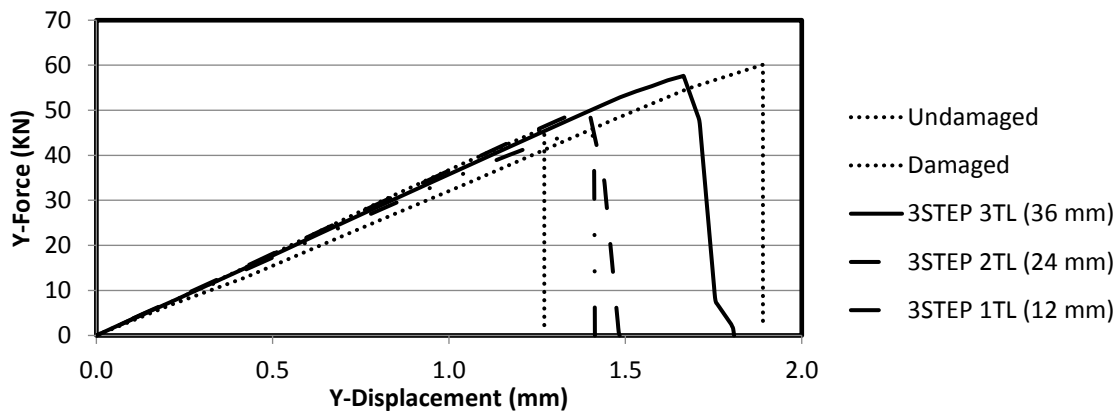
### 5.3.2 7 Plies CFRP composite laminate

Figure 5.16 shows the failure load of undamaged and damage 7 Plies CFRP composite laminate. The simulation damaged laminate failed at 46 KN and during experimental test the laminate failed at 50 KN, this different is because of restoring of stress during experimental testing process. However, undamaged laminate failed at a higher compression load compared to the damaged laminate, with an average increase in peak load of 25%.



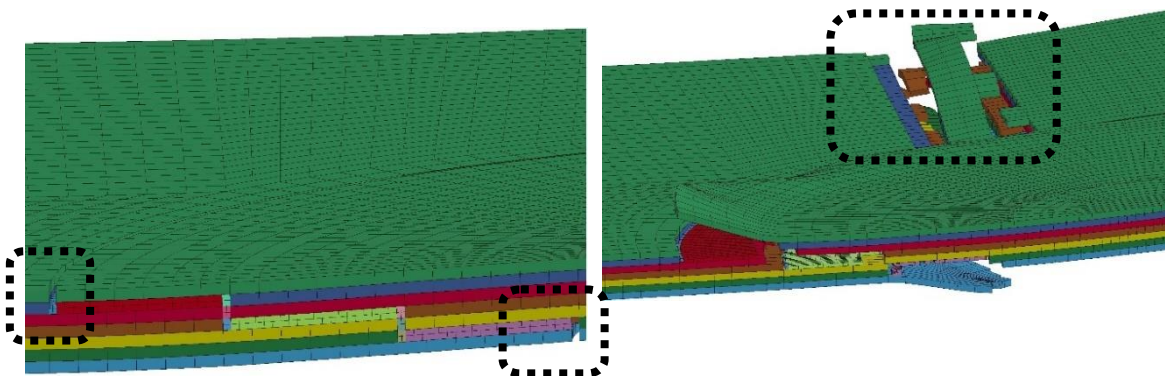
**Figure 5. 16 Failure load versus displacement for undamaged and damage of CFRP composite laminate with 7 plies.**

Figure 5.17 shows the compressive failure load versus displacement for the repaired CFRP composite laminate with 7 plies by the stepped joints. The stepped joints (three steps) was applied to different geometries to find the optimum repaired method such as various overlap lengths (TL). In this case the failure loads increase by 25% when total overlap length increases from 12 mm to 36 mm as shown in Figure 5.17. The optimum stepped lap joint configuration was able to restore about 90% of the compression failure load of the undamaged laminate. The compression failure load increases by 14% when the overlap length increases from 24 mm to 36 mm. Therefore, stepped lap joint with three step and 36 mm overlap length has been defined the optimal repair method for the damaged CFRP composite laminate with 7 plies.



**Figure 5. 17 Numerical modelling on compressive failure load versus displacement for various 4-stepped lap joint with different overlap length for 7 Plies CFRP composite laminate.**

Figure 5.18 shows the behaviour of a repaired CFRP composite laminate with 7 layers under compression loading. The failure starts at the adhesive material placed on the corner of stepped lap joint in the specimen lower face then continues in other edge of stepped lap joint in the specimen upper face which is expected because the stress level in the edge area is higher than other area. Then the damage propagated until loading reaches the failure load level. At this level, the crack is propagated around the repair zone until the full damage happen on the sides of the specimen which causes ultimate failure within the specimen, as shown in Figure 5.18.



**Figure 5. 18 The behaviour of a repaired 7 Plies CFRP composite laminate under compression loading**

Finally, the objective of this study was to utilise the commercial tools such as LS-DYNA and Truegrade programs to predict the optimum repair method to restore the failure load of the damaged composite structures with some condition such as the limited resource and time. In this chapter the compression after impact test has been used to determine the compressive failure load for the damaged and undamaged specimens and used to validate the simulation results. The numerical model was performed to define the optimum repair joints. The stepped lap joint with three step and 36 mm overlap length was the optimum repair method for the damaged CFRP composite laminate with 7 and 11 layers.



# **Chapter 6**

## **Conclusions and Future Work**

## **6.1. Introduction**

The study provide a practical numerical methodology to predict the optimum repair method to repair the damaged Carbon Fibre Reinforced Plastic (CFRP) composite structure under high velocity impact during some operations and exercise activities by using commercial tool. To establish an appropriate methodology, it was required to be study the behaviour of CFRP composite laminates under high velocity impact and the behaviour of undamaged, damaged and repaired CFRP composite laminates under compression load by using compression after impact test

## **6.2. Conclusion**

In the study the experimental test and numerical model proposed to predict the non-linear mechanical response of CFRP composites laminates subject to high velocity impact. The compression after impact test used to defined the failure load for damage (impact damage) and undamaged CFRP composites laminates, also a numerical model of compression after impact test was created to defined the failure load for damage (impact damage), undamaged and repaired CFRP composites laminates to predict the optimum repair method. Moreover, this study included the behaviour of different thickness (16 plies, 11 plies and 7 plies) of woven CFRP composite laminates subject to range of impact velocity between 100 m/s to 500 m/s by using experimental method in (chapter 3) and numerical method in chapter (4) and chapter (5).

The first step of the study was to review TRUEGRID and LSDYNA solver manual to find the suitable techniques to model the behaviour of composite laminates subject to high velocity impact damage and to model the compression after impact test. The impact damage section presented the following findings:

The results of the simulation show the capability of the numerical methodology to capture the material failure mechanisms during penetration such as compression through thickness failure, out-of-plane shear failure and in-plane tensile failure of the fibres located at the rear surface, where high tensile stresses develop.

Moreover, there a similarity of the residual kinetic energy between numerical and experimental with 5.0 % difference. This slight difference in the residual kinetic energy of the projectile can be attributed to neglect of the frictional energy of eroding elements surrounding the projectile during penetration, and/or the mesh size may not be refined enough for the penetration.

In order to predict the optimum repair method after impact damage, the compression after impact test was conducted to obtain the compressive failure load for undamaged and damaged woven CFRP composite laminates then used these results to validate the numerical model for undamaged, damaged and repaired CFRP composite laminate. The compressive failure load of each specimen is measured by compression after Impact test using a special fixture. the optimum repair method presented the following findings:

Test results show that the compressive failure load of CFRP composite laminate is reduced as the impact velocity increases. The experimental and numerical show the compressive failure occurs by delamination propagation perpendicular to the loading direction due to local buckling that started at the impact damage location. This failure behaviour was predicated because the failure for damaged specimen happens in the weakest area and failed by crushing brooming and both were failed in the same area.

The difference between compressive failure load in numerical model and experimental test for of damaged and undamaged 7 plies CFRP composite laminates about 10%, this difference because of restore stress in experimental damaged laminate. However, undamaged laminate failed at a higher compression load compared to the damaged laminate, with an average increase in peak load of 25%.

For 11 plies composite laminates the simulations results provide a good match with the experimental results with difference about 5% for damage and undamaged laminate. Moreover, the damaged laminate failed at lower compression load compared with the undamaged laminate, with an average decrease in peak load of 57%.

The second step, after proving the numerical modelling can be determine the compressive failure load for damaged and undamaged CFRP composite laminates. The numerical model was extending to simulate the repaired CFRP composite laminate under compression load to optimise the stepped lap joints to repair different woven CFRP composite laminates thickness (11 plies and 7 plies). The design of experiments procedure used as optimisation method which include number of case studies. These case studies have used the number of steps and overlap length as main criteria in the optimisation method. Moreover, in this work has confirmed the importance of optimising the number of step and overlap length to provide an effective joint within CFRP

The defects in the stepped lap joints are an outcome from the adhesive bonded. The optimum stepped lap joint restores a significant percentage of their original compressive failure load. In 11 plies CFRP compost laminate, the compressive failure load recovery after repaired exceeded 90% with respect to their undamaged laminate. Furthermore, the compressive failure load recovery after repaired 7 plies CFRP compost laminate exceeded 90% with respect to their undamaged laminate.

According to the numerical studies the optimum number of step and overlap length of the stepped lap joint is approximately three step and 36 mm length for 11 plies and three step and 36 mm length for 7 plies CFRP composite laminates. Finally, the above results show the study achieved the main contributions to knowledge which is established a practical numerical methodology to predict the optimum joint to repair the damaged CFRP composite structure under high velocity impact during some operations and exercise activities.

### **6.3. Future Work**

- Modified the gas gun rig to increase the speed measurement capability and use low speed camera to study impact behaviour in detail.
- Advanced post impact inspection instrument such as C-scan will be used to measure damage size and type.
- Created repaired capability to assessment the numerical modelling.
- Expand the numerical modelling to include other factors affect to repaired procedure such as void in adhesive and layup angle.

### **6.4. Publications**

N. Alzeanidi, H. Ghasemnejad, Effect of High Velocity Impact Damage on the Repairability of Composite Panels, Composite Structures, Under Review, 2017.

## References

- Abrate S. (2001), "Modeling of impacts on composite structures". *Compos Struct* vol.51, pp. 129–138.
- Abrate, S. (1991), "Impact on laminated composite materials", *Applied Mechanics Review*, vol. 44, pp. 155-190.
- Abrate, S. (1994), "Impact on laminated composite materials: recent advances", *Applied Mechanics Review*, vol. 47, pp. 517-544.
- Abrate, S. (1998), *Impact on composite structures*, Cambridge University Press, Cambridge.
- Ambur, D. R., Jaunky, N., Lawson, R. E. and Knight, N. F. (2001), "Numerical simulations for high-energy impact of thin plates", *International Journal of Impact Engineering*, vol. 25, no. 7, pp. 683-702.
- Aviation Research and Analysis Report AAR-2007-021, Australian Transport Safety Bureau, (2007).
- Baker, A. (1997), "Joining and repair of aircraft composite structures", in *UNITED STATES*, New York: Marcel Dekker, Inc. (Materials Engineering. Vol. 11).
- Baker, Alan Dutton, Stuart Kelly, Donald. (2004). "Composite Materials for Aircraft Structures" (2nd Edition). American Institute of Aeronautics and Astronautics
- Ball, R. E. (1985), *The fundamentals of aircraft combat survivability analysis and design [(Book)]*, .
- Belhouari, M., Bachir Bouiadjra, B., Megueni, A. and Kaddouri, K. (2004), "Comparison of double and single bonded repairs to symmetric composite structures: a numerical analysis", *Composite Structures*, vol. 65, no. 1, pp. 47-53.
- Bendemra H, Compston P, Phillip J. (2015), "Crothers Optimisation study of tapered scarf and stepped-lap joints in composite repair patches", *Composite Structures* 130 1–8
- Bland, P. W. and Dear, J. P. (2001), "Observations on the impact behaviour of carbon-fibre reinforced polymers for the qualitative validation of models", *Composites Part A: Applied Science and Manufacturing*, vol. 32, no. 9, pp. 1217-1227.
- Bogdanovich, A. E. and Kizhakkethara, I. (1999), "Three-dimensional finite element analysis of double-lap composite adhesive bonded joint using submodeling approach", *Composites Part B: Engineering*, vol. 30, no. 6, pp. 537-551.
- Campilho, R. D. S. G., de Moura, M. F. S. F. and Domingues, J. J. M. S. (2009), "Numerical prediction on the tensile residual strength of repaired CFRP under different geometric changes", *International Journal of Adhesion and Adhesives*, vol. 29, no. 2, pp. 195-205.

Cantwell WJ, Morton J. (1986), "An assessment of the impact performance of CFRP reinforced with high-strain carbon-fibers". *Compos Sci Technol* 25 133–148.

Cantwell, W. J. and Morton, J. (1985), "Detection of impact damage in CFRP laminates", *Composite Structures*, vol. 3, no. 3-4, pp. 241-257.

Cantwell, W. J. and Morton, J. (1989), "Comparison of the low and high velocity impact response of cfrp", *Composites*, vol. 20, no. 6, pp. 545-551.

Cantwell, W. J. and Morton, J. (1990), "Impact perforation of carbon fibre reinforced plastic", *Composites Science and Technology*, vol. 38, no. 2, pp. 119-141.

Cantwell, W. J. and Morton, J. (1991), "The impact resistance of composite materials — a review", *Composites*, vol. 22, no. 5, pp. 347-362.

Chan, S., Fawaz, Z., Behdinin, K. and Amid, R. (2007), "Ballistic limit prediction using a numerical model with progressive damage capability", *Composite Structures*, vol. 77, no. 4, pp. 466-474.

Chang, F. and Chang, K. (1988), "A progressive damage model for laminated composites containing stress concentrations: Chang, F. and Chang, K. *Journal of Composite Materials* Vol 21 (September 1987) pp 834–855", *Composites*, vol. 19, no. 4, pp. 329-329.

Chen, J. K., Allahdadi, F. A. and Carney, T. C. (1997), "High-velocity impact of graphite/epoxy composite laminates", *Composites Science and Technology*, vol. 57, no. 9-10, pp. 1369-1379.

Choi, H. and Chang, F. U. - U. O. (1992), "A model for predicting damage in graphite/epoxy laminated composites resulting from low-velocity point impact", vol. 26, no. 14, pp. 2134-2169.

Choi, H., Downs, R. J. and Chang, F. U.- K. U. O. (1991), "A new approach toward understanding damage mechanisms and mechanics of laminated composites due to low-velocity impact. I - Experiments", vol. 25, pp. 992-1011.

Choi, H., Wu, H. S. I.- Y. U. N. G. T. and Chang, F. U. -K. U. O. (1991), "A new approach toward understanding damage mechanisms and mechanics of laminated composites due to low-velocity impact. II - Analysis", vol. 25, pp. 1012-1038.

Chue, C. and Liu, T. J. (1995), "The effects of laminated composite patch with different stacking sequences on bonded repair", *Composites Engineering*, vol. 5, no. 2, pp. 223-230.

Department of Mechanical Engineering at City College of New York, Final Report-High Velocity Gas Gun, available at: <http://www-me.ccnycuny.edu/cur-reform/product/gasgunreport.pdf> (accessed 6<sup>th</sup> July 2009).

Dilger, R., Hicketier, H. and Greenhalgh, M. D. (2009), "Eurofighter a safe life aircraft in the age of damage tolerance", *International Journal of Fatigue*, vol. 31, no. 6, pp. 1017-1023.

Fujii, K., Aoki, M., Kiuchi, N., Yasuda, E. and Tanabe, Y. (2002), "Impact perforation behavior of CFRPs using high-velocity steel sphere", *International Journal of Impact Engineering*, vol. 27, no. 5, pp. 497-508.

Ganesh, V. K. and Choo, T. S. (2002), "Modulus Graded Composite Adherends for Single-Lap Bonded Joints", *Journal of Composite Materials*, vol. 36, no. 14, pp. 1757-1767.

Garcia-Castillo SK, Sanchez-Saez S, López-Puente J, Barbero E, Navarro C. (2009), "Impact behaviour of preloaded glass/polyester woven plates". *Compos Sci Technol* 69 711–717.

Guan, Z. W., Cantwell, W. J. and Abdullah, R. (2008), "Numerical modeling of the impact response of fiber-metal laminates", *Polymer Composites*, vol. 36, no. 5, pp. 603-611.

Guild, F. J., Potter, K. D., Heinrich, J., Adams, R. D. and Winsom, M. R. (2001), "Understanding and control of adhesive crack propagation in bonded joints between carbon fibre composite adherends II. Finite element analysis", *International Journal of Adhesion and Adhesives*, vol. 21, no. 6, pp. 445-453.

Gunnion, A. J. and Herszberg, I. (2006), "Parametric study of scarf joints in composite structures", *Composite Structures*, vol. 75, no. 1-4, pp. 364-376.

Hammond, R. I., Proud, W. G., Goldrein, H. T. and Field, J. E. (2004), "High-resolution optical study of the impact of carbon-fibre reinforced polymers with different lay-ups", *International Journal of Impact Engineering*, vol. 30, no. 1, pp. 69-86.

Hart-Smith L. (1973), "Adhesive-bonded scarf and stepped-lap joints, Tech. Rep. NASA CR 112237, Langley Research Center, Hampton: VA.

Hazell, P.J., Kister, G., Stennett, C. Bourque, P. & Cooper, G. (2008), "Normal and oblique penetration of woven CFRP laminates by a high velocity steel sphere". *Composite* 39 866-874.

Hosur MV, Vaidya UK, Ulven C, Jeelani S. (2004), "Performance of stitched/unstitched woven carbon/epoxy composites under high velocity impact loading". *Compos Struct* 64 455–566.

Hosur, M. V., Vaidya, U. K., Myers, D. and Jeelani, S. (2003), "Studies on the repair of ballistic impact damaged S2-glass/vinyl ester laminates", *Composite Structures*, vol. 61, no. 4, pp. 281-290.

Hou, J. P., Petrinic, N., Ruiz, C. and Hallett, S. R. (2000), "Prediction of impact damage in composite plates", *Composites Science and Technology*, vol. 60, no. 2, pp. 273-281.



- Hu, F. Z. and Soutis, C. (2000), "Strength prediction of patch-repaired CFRP laminates loaded in compression", *Composites Science and Technology*, vol. 60, no. 7, pp. 1103-1114.
- Iannucci, L. and Willows, M. L. (2006), "An energy based damage mechanics approach to modelling impact onto woven composite materials—Part I: Numerical models", *Composites Part A: Applied Science and Manufacturing*, vol. 37, no. 11, pp. 2041-2056.
- Ichikawa K, Shin Y, Sawa. (2008), "A three-dimensional finite-element stress analysis and strength evaluation of stepped-lap adhesive joints subjected to static tensile loadings" *Int J Adhes Adhes* 28 464–470.
- Kim HS, Lee SJ, Lee DG. Development of a strength model for the cocured stepped lap joints under tensile loading. *Compos Struct* 32(1995) 593–600.
- Kim JH, Park BJ, Han YW. (2004), "Investigating the flexural resistance of fibre reinforced cementitious composites under biaxial condition" *Compos Struct* 66 69–75.
- Kim, K., Yoo, J., Yi, Y. and Kim, C. (2006), "Failure mode and strength of uni-directional composite single lap bonded joints with different bonding methods", *Composite Structures*, vol. 72, no. 4, pp. 477-485.
- Kimiaefar A, Lund E, Thomsen OT, Sorensen JD. (2013) "Asymptotic Sampling for reliability analysis of adhesive bonded stepped lap composite joints". *Eng Struct* 49 655–663.
- Li D, Qing G, Liu Y. (2011), "A layerwise/solid-element method for the composite stiffened laminated cylindrical shell structures". *Compos Struct* 93 1673–1682.
- Livermore Software Tech. Corp. (2007), *LS-DYNA User Manual Version 971*, Livermore Software Tech. Corp.
- López-Puente J, Zaera R, Navarro C. (2007), "An analytical model for high velocity impacts on thin CFRPs woven laminates". In *J Solids Struct* 44 2837–2851.
- López-Puente J, Zaera R, Navarro C. (2003), "High energy impact on woven laminates". *J Phys IV* 110 639–644.
- López-Puente J, Zaera R, Navarro C. (2002), "The effect of low temperatures on the intermediate and high velocity impact response of CFRP". *Composites: Part B* 33 559–566.
- López-Puente, J., Zaera, R. and Navarro, C. (2008), "Experimental and numerical analysis of normal and oblique ballistic impacts on thin carbon/epoxy woven laminates", *Composites Part A: Applied Science and Manufacturing*, vol. 39, no. 2, pp. 374-387.

- Megueni, A. and Lousdad, A. (2008), "Comparison of symmetrical double sided and stepped patches for repairing cracked metallic structures", *Composite Structures*, vol. 85, no. 1, pp. 91-94.
- Muslim A, Anupam C. (2016) "Impact behavior of FRP composite plate under low to hyper velocity impact". *Composites Part B* 95462-474
- Nikhil V Nayak, (2014), "Composite Materials in Aerospace Applications", *International Journal of Scientific and Research Publications*, Volume 4, Issue 9.
- Odi, R. A. and Friend, C. M. (2002), "A Comparative Study of Finite Element Models for the Bonded Repair of Composite Structures", *Journal of Reinforced Plastics and Composites*, vol. 21, no. 4, pp. 311-332.
- Olsson, R. (2000), "Mass criterion for wave controlled impact response of composite plates", *Composites Part A: Applied Science and Manufacturing*, vol. 31, no. 8, pp. 879-887.
- Pernas-Sánchez J, Artero-Guerrero J.A, Zahr Viñuela J, Varas D, López Puente J. (2014), "Numerical analysis of high velocity impacts on unidirectional laminates". *Composite Structures* 107 629–634
- Potter, K. D., Guild, F. J., Harvey, H. J., Wisnom, M. R. and Adams, R. D. (2001), "Understanding and control of adhesive crack propagation in bonded joints between carbon fibre composite adherends I. Experimental", *International Journal of Adhesion and Adhesives*, vol. 21, no. 6, pp. 435-443.
- Rispler, A. R., Tong, L., P. Steven, G. and Wisnom, M. R. (2000), "Shape optimisation of adhesive fillets", *International Journal of Adhesion and Adhesives*, vol. 20, no. 3, pp. 221-231.
- William G. Roeseler, Branko Sarh, Max U. Kismarton (2007), "Composite structures: the first 100 years", 16th international conference on composite materials.
- Salih Akpınar, (2014), "The strength of the adhesively bonded step-lap joints for different step" *Numbers Composites: Part B* 67 170–178
- Silva, M. A. G. (1999), "Low speed impact on polyethylene and aramidic FRP laminates ", *Proceedings of Conference on Integrity, Reliability and Failure*, Porto., .
- Soutis, C., Duan, D. and Goutas, P. (1999), "Compressive behaviour of CFRP laminates repaired with adhesively bonded external patches", *Composite Structures*, vol. 45, no. 4, pp. 289-301.
- Sun, C. T. and Potti, S. V. (1996), "A simple model to predict residual velocities of thick composite laminates subjected to high velocity impact", *International Journal of Impact Engineering*, vol. 18, no. 3, pp. 339-353.

Tanabe, Y., Aoki, M., Fujii, K., Kasano, H. and Yasuda, E. (2003), "Fracture behavior of CFRPs impacted by relatively high-velocity steel sphere", *International Journal of Impact Engineering*, vol. 28, no. 6, pp. 627-642.

Varas D, Artero-Guerrero J.A, Pernas-Sánchez J, López-Puente J. (2013), "Analysis of high velocity impacts of steel cylinders on thin carbon/epoxy woven laminates". *Composite Structures* 95 623–629.

Wang, C. H. and Gunnion, A. J. (2008), "On the design methodology of scarf repairs to composite laminates", *Composites Science and Technology*, vol. 68, no. 1, pp. 35-46.

Xin S, Wen H. (2015), "A progressive damage model for fiber reinforced plastic composites subjected to impact loading". *Int J impact Eng* 75 40-52.

XYZ Scientific Application, I. (2001), *True Grid Manual Version 2.1.0* XYZ Scientific Application, Inc.

yen, C. F. (2002), "Ballistic impact modelling of composite materials.", *Proceedings of the 7th international LS-DYNA users conference, Penetration / Explosive*. Southfield, Michigan.

Zukas, J. A. (1990), *High velocity impact dynamics*, Wiley, New York; Chichester.

# APPENDIX A

**Truegrid input file to Model11 plies composite Laminate subject to High velocity impact defined as:**

```
*****
lsdyna keyword
*****
*               create symmetric laminate               *
*****
c symmetry plane yoz, normal x
plane 1 0 0 0 1 0 0 0.01 symm;
sd 4 plane 0 -75 0 0 -74 0;
sd 3 plane 0 75 0 0 74 0;
*****
*               create reflect the model                *
*****
lct 1 rxz;
*****
*               create composite laminate model         *
*****
*               r: hole riduse D: adhesive thickness TAD: Laminate thickness *
*               Tall: total laminate length N : No. of step *
*****
parameter r 12 D 0.375 TAD 4.125 N 3 T 3 Tall 75
f [%N+1]
if (%N .eq.3) then
f1 [(%TAD/%f)+0.09375]
elseif (%N .eq. 4)then
f1 [(%TAD/%f)-0.075]
endif
*****
*               create step high (h) and step length (L) *
*****
h1 [%f1]                c high step 1
h2 [%f1+%h1]            c high step 2
h3 [%f1+%h2]            c high step 3
if (%N .eq. 4)then
h4 [%f1+%h3]            c high step 4
endif
L1 [(%r*(%TR))/ %N]     c length step 1
L2 [(%r*(%TR))/ %N]     c length step 2
L3 [(%r*(%TR))/ %N]     c length step 3
if (%N .eq. 4)then
```

```

L4 [(%r*(%TR))/ %N]          c length step 4
endif
*****
*           Defined the main points in the model  in z-direction           *
*****

k1 0
k4 0
k5 %TAD
k8 %TAD
k9 %h1
k10 [%h1]
k11 %h2
k12 [%h2]
k13 %h3
k14 [%h3]
if (%N .eq. 4)then
k15 %h4
k16 [%h4]
endif
k19 %TAD
*****

*           Defined the main points in the model  in x-direction           *
*****

k20 [%r+%D]
k21 [%r+%D]
K22 [%r+%L1+%D]
k23 [%r+%L1+%D]
k24 [%r+%L1+%L2+%D]
k25 [%r+%L1+%L2+%D]
k26 [%r+%L1+%L2+%L3+%D]
k27 [%r+%L1+%L2+%L3+%D]
if (%N .eq. 4) then
k28 [%r+%L1+%L2+%L3+%L4+%D]
k29 [%r+%L1+%L2+%L3+%L4+%D]
endif
if (%N .eq. 3)then
k31 %k27
k15 %k19
elseif (%N .eq. 4)then
k31 %k29
k17 %k19
endif;
sid 1 lsdsi 2;
*****

*           Create the projectile model                                   *
*****

block
1 6 12;
1 6 12 18 24;
1 6 12 18 24;
0 3.0 3.0;
-3.0 -3.0 0 3.0 3.0;
7.4 7.4 10.4 13.4 13.4;
dei 0 2 3;1 2 0 4 5;;
dei 0 2 3;;1 2 0 4 5;
dei ;1 2 0 4 5;1 2 0 4 5;
orpt - 0.0 0.0 5.0

```

```

sd 2 sp 0 0 10.4 6
sfi 1 -3;-1 -5;-1 -5;sd 2
mate 1
endpart
*****
*   Create the hole area ( joint area) model  in composite laminate   *
*****

block
1 [((%k20/%D)/4)+1] [((%k20/(%D))/4)+5];
1 [((%k20/%D)/4)+1] [((%k20/(%D))/4)+5];
1 2 3 4 5 6 7 8 9 10 11 12;
0 [%k20/3] [%k20/3]; 0 [%k20/3] [%k20/3];
0 .375 .75 1.125 1.5 1.875 2.25 2.625 3 3.375 3.75 4.125;
dei 2 3; 2 3;;
sfi 1 -3;1 -3;1 12;cy 0 0 0 0 1 [%r-4];
mti ; ;1 2;2
:
:
:
:
mti ; ;11 12;12
lrep 0 1;
cylinder 1 3; 1 [((%k20/%D)/2)+1];
1 2 3 4 5 6 7 8 9 10 11 12;
[%r-4] [%r-2]; 0 90;
0 .375 .75 1.125 1.5 1.875 2.25 2.625 3 3.375 3.75 4.125;
bb 2 1 1 2 2 12 1;
mti ; ;1 2;2
:
:
:
:
mti ; ;11 12;12
lrep 0 1;
cylinder 1 3; 1 [((%k20/%D))+16];
1 2 3 4 5 6 7 8 9 10 11 12;
[%r-2] [%r+%d]; 0 90;
0 .375 .75 1.125 1.5 1.875 2.25 2.625 3 3.375 3.75 4.125;
trbb 1 1 1 1 2 12 1;
mti ; ;1 2;2
:
:
:
:
mti ; ;11 12;12
lrep 0 1;
*****
*                               Model the step in joint area                               *
*****
c first step with different possible high and length *
*****
if (%k10 .le. 1)then
cylinder 1 [(((%k22-%k20)))-3]; 1 [((%k20/%D))+16];
1 2 3 4 5 6 7 8 9 10;
%k20 %k22; 0 90; [%k10] [%k10+0.375] [%k10+0.75] [%k10+1.125] [%k10+1.5]
[%k10+1.875] [%k10+2.25] [%k10+2.625] [%k10+3] [%k10+3.375];
mti ; ;1 2;4
:

```

```

:
:
mti ; ;9 10;12
lrep 0 1;
elseif (%k10 .eq. 1.125)then
cylinder 1 [(((%k22-%k20)))-3]; 1 [((%k20/%D))+16];
1 2 3 4 5 6 7 8 9;
%k20 %k22; 0 90; [%k10] [%k10+0.375] [%k10+0.75] [%k10+1.125] [%k10+1.5]
[%k10+1.875] [%k10+2.25] [%k10+2.625] [%k10+3];
mti ; ;1 2;5
:
:
:
:
mti ; ;8 9;12
lrep 0 1;
endif
*****
c Second step with different possible high and length *
*****
if (%k12 .eq. 2.25)then
cylinder 1 [(((%k24-%k22)))-3]; 1 [((%k20/%D))+16];
1 2 3 4 5 6;
%k22 %k24; 0 90;
[%k12] [%k12+0.375] [%k12+0.75] [%k12+1.125] [%k12+1.5] [%k12+1.875];
mti ; ;1 2;8
:
:
:
:
mti ; ;5 6;12
lrep 0 1;
elseif (%k12 .eq. 1.5)then
cylinder 1 [(((%k24-%k22)))-3]; 1 [((%k20/%D))+16];
1 2 3 4 5 6 7 8;
%k22 %k24; 0 90;
[%k12] [%k12+0.375] [%k12+0.75] [%k12+1.125] [%k12+1.5]
[%k12+1.875] [%k12+2.25] [%k12+2.625];
mti ; ;1 2;6
:
:
:
:
mti ; ;7 8;12
lrep 0 1;
endif
C *****
c third step with different possible high and length *
C *****
if (%k14 .eq. 3.375)then
cylinder 1 [(((%k26-%k24)))-3]; 1 [((%k20/%D))+16];
1 2 3;
%k24 %k26; 0 90;
[%k14] [%k14+0.375] [%k14+0.75];
mti ; ;1 2;11
mti ; ;2 3;12
lrep 0 1;
elseif (%k14 .eq. 2.25)then

```

```

cylinder 1 [(((%k26-%k24)))-3]; 1 [((%k20/%D))+16];
1 2 3 4 5 6;
%k24 %k26; 0 90;
[%k14] [%k14+0.375] [%k14+0.75] [%k14+1.125] [%k14+1.5] [%k12+1.875];
mti ; ;1 2;8
:
:
:
mti ; ;5 6;12
lrep 0 1;
endif

```

```

*****
* fourth step with different possible high and length *
*****

```

```

if (%N .gt. 3)then
cylinder 1 [(((%k28-%k26)))-3]; 1 [((%k20/%D))+16];
1 2 3 4;
%k26 %k28; 0 90;
[%k16] [%k16+0.375] [%k16+0.75] [%k16+1.125];
mti ; ;1 2;10
mti ; ;2 3;11
mti ; ;3 4;12
lrep 0 1;
endif

```

```

c *****
c Model the step in Parent Area *

```

```

c *****
c first step with different possible high and length *
*****

```

```

if (%k9.le.1)then
cylinder 1 [(((%k23-%k21)))-3]; 1 [((%k20/%D))+16];
1 2 3;
%k21 %k23; 0 90; [%k9-0.75] [%k9-0.375] [%k9];
mti ; ;1 2;2
mti ; ;2 3;3
lrep 0 1;
elseif (%k9 .eq. 1.125)then
cylinder 1 [(((%k23-%k21)))-3]; 1 [((%k20/%D))+16];
1 2 3 4;
%k21 %k23; 0 90; [%k9-1.125] [%k9-0.75] [%k9-0.375] [%k9];
mti ; ;1 2;2
mti ; ;2 3;3
mti ; ;3 4;4
lrep 0 1;
endif

```

```

* second step with different possible high and length *
*****

```

```

if (%k11 .eq. 2.25)then
cylinder 1 [(((%k25-%k23)))-3]; 1 [((%k20/%D))+16];
1 2 3 4 5 6 7;
%k23 %k25; 0 90; [%k11-2.25] [%k11-1.875] [%k11-1.5] [%k11-1.125]
[%k11-0.75] [%k11-0.375] [%k11];

```



```

mti ; ;1 2;2
:
:
:
mti ; ;6 7;7
lrep 0 1;
elseif (%k11 .eq. 1.5)then
cylinder 1 [(((%k25-%k23)))-3]; 1 [((%k20/%D))+16];
1 2 3 4 5;
%k23 %k25; 0 90; [%k11-1.5]
[%k11-1.125] [%k11-0.75] [%k11-0.375] [%k11];
mti ; ;1 2;2
mti ; ;2 3;3
mti ; ;3 4;4
mti ; ;4 5;5
lrep 0 1;
endif
*****
*           third step with different possible high and length           *
*****
if (%k13 .eq. 3.375)then
cylinder 1 [(((%k27-%k25)))-3]; 1 [((%k20/%D))+16];
1 2 3 4 5 6 7 8 9 10;
%k25 %k27; 0 90;
[%k13-3.375] [%k13-3] [%k13-2.625] [%k13-2.25] [%k13-1.875] [%k13-1.5]
[%k13-1.125] [%k13-0.75] [%k13-0.375] [%k13];
mti ; ;1 2;2
:
:
:
mti ; ;9 10;10
lrep 0 1;
elseif (%k13 .eq. 2.25)then
cylinder 1 [(((%k27-%k25)))-3]; 1 [((%k20/%D))+16];
1 2 3 4 5 6 7;
%k25 %k27; 0 90;
[%k13-2.25] [%k13-1.875] [%k13-1.5][%k13-1.125]
[%k13-0.75] [%k13-0.375] [%k13];
mti ; ;1 2;2
:
:
:
mti ; ;6 7;7
lrep 0 1;
endif
*****
*           fourth step with different possible high and length           *
*****
if (%N .gt. 3)then
cylinder 1 [(((%k29-%k27)))-3]; 1 [((%k20/%D))+16];
1 2 3 4 5 6 7 8 9;
%k27 %k29; 0 90;
[%k15-3] [%k15-2.625]
[%k15-2.25] [%k15-1.875] [%k15-1.5] [%k15-1.125]
[%k15-0.75] [%k15-0.375] [%k15];
mti ; ;1 2;2

```

```

:
:
:
mti ; ;8 9;9
lrep 0 1;
endif
*****
*                composite area out of repair area                *
C *****
cylinder 1 [(((%k31+2)-%k31))+1]; 1 [(((%k20/%D))+16)];
1 2 3 4 5 6 7 8 9 10 11 12;
%k31 [%k31+3]; 0 90; 0 .375 .75 1.125 1.5 1.875 2.25 2.625
3 3.375 3.75 4.125;
mti ; ;1 2;2
:
:
:
mti ; ;11 12;12
lrep 0 1;
block 1 [((%k20/%D)/2)+9];
1 [((%k20/%D)/2)+6];
1 2 3 4 5 6 7 8 9 10 11 12;
0 [(%k31+3)*0.707]; [(%k31+3)*0.707] %TAll;
0 .375 .75 1.125 1.5 1.875 2.25 2.625 3
3.375 3.75 4.125;
sfi ; -1 2; ;cy 0 0 0 0 0 7 [%k31+3];
mti ; ;1 2;2
:
:
:
mti ; ;11 12;12
lrep 0 1;
block 1 [((%k20/%D)/2)+6];
1 [((%k20/%D)/2)+9];
1 2 3 4 5 6 7 8 9 10 11 12;
[(%k31+3)*0.707] %TAll; 0 [(%k31+3)*0.707];
0 .375 .75 1.125 1.5 1.875 2.25 2.625 3
3.375 3.75 4.125;
sfi -1 2; ; ;cy 0 0 0 0 0 7 [%k31+3];
mti ; ;1 2;2
:
:
:
mti ; ;11 12;12
lrep 0 1;
block 1 [((%k20/%D)/2)+6];
1 [((%k20/%D)/2)+9];
1 2 3 4 5 6 7 8 9 10 11 12;
[(%k31+3)*0.707] %TAll; [(%k31+3)*0.707] %TAll;
0 .375 .75 1.125 1.5 1.875 2.25 2.625 3
3.375 3.75 4.125;
mti ; ;1 2;2
:
:
:

```

```

mti ; ;11 12;12
lrep 0 1;
endpart
merge
stp 0.1
nset node1 = srf 3 .01;
nset node2 = srf 4 .01;
labels nodeset node1;
labels nodeset node2;
write

```

## APPENDIX B

### LS-DYNA Keyword file for 11 plies composite Laminate subject to High velocity impact defined as:

```

$#*****
$#          LS-DYNA Keyword file for repaired composite laminate
$#          subject to compression load          *
$#*****
*KEYWORD 90000000
*TITLE
$#*****
$# title
lsdyna model: projectile Sphere Impact a composite plate at High velocity
$#*****
$# Difined Dynamic relaxation and damping parameters
$#*****
*CONTROL_DYNAMIC_RELAXATION
$# nrcyck  drtol  drfctr  drterm  tssfdr  irelal  edttl  idrflg
   250    0.001  5.995    0.00    0.00    0      0.04    0
*DAMPING_GLOBAL
$# lcid  valdmp  stx  sty  stz  srx  sry  srz
   0    1800.0  90.0  90.0  90.0  0.00  0.00  0.00
*CONTROL_DAMPING
$# nrcyck  drtol  drfctr  drterm  tssfdr  irelal  edttl  idrflg
   250  0.001000  0.995000
$#*****
$#          Contact Algorithm
$#*****
*CONTROL_CONTACT
$# slsfac  rwpnal  islchk  shlthk  penopt  thkchg  orien  enmass
  0.100000  0.000    2      0      0      0      1
$# usrstr  usrfrc  nsbcs  interm  xpene  ssthk  ecdt  tiedprj
   0      0      0      0  4.000    0      0      0
$# sfric  dfric  edc  vfc  th  th_sf  pen_sf
  0.30000  0.10000
$# ignore  frceng  skiprwg  outseg  spotstp  spotdel  spothin
   1      1
$# isym  nserod  rwgaps  rwgdth  rwksf  icov  swradf  ithoff
   1      0      0  0.000  1.000000    0  1.000000

```

```

$# shledg
  0
*CONTACT_ERODING_SINGLE_SURFACE_ID
$#  cid                      title
    1TrueGrid
$#  ssid  msid  sstyp  mstyp  sboxid  mboxid  spr  mpr
    0    0    5    5    0    0    1    1
$#  fs   fd   dc   vc   vdc  penchk   bt   dt
    0.300 0.100 0.000 0.000 0.000   1 1.00e-9
$#  sfs  sfm  sst  mst  sfst  sfmt   fs  vsf
    10.00000 10.00000
$#  isym  erosop  iadj
    1    1    1
$#  soft  sofsc1  lcidab  maxpar  sbopt  depth  bsort  frcfreq
    2 0.600000   0 1.025000 2.000000   2    0    1
$#  penmax  thkopt  shlthk  snlog  isym  i2d3d  sldthk  sldstf
    0.000   0    0    0    0    0.000  0.000
$#*****
$#                               Control Parameters
$#*****
*CONTROL_ENERGY
$#  hgen  rwen  slnten  rrlen
    2    1    2    2
*CONTROL_HOURLASS
$#  ihq  qh
    2 0.100000
*CONTROL_SOLID
$#  esort  fmatrix  niptets
    1    0    4
$#  pm1  pm2  pm3  pm4  pm5  pm6  pm7  pm8  pm9  pm10
    0    0    0    0    0    0    0    0    0    0
*CONTROL_TERMINATION
$#  endtim  endcyc  dtmin  endeng  endmas
    3.0E-4
*CONTROL_TIMESTEP
$#  dtinit  tssfacc  isdo  tslimt  dt2ms  lctm  erode  ms1st
    0.000 0.300000   0 0.000 0.000   0    1
$#  dt2msf  dt2mslc  imsc1
    0.000   0    0
$#*****
$#                               Output Results
$#*****
*DATABASE_BNDOUT
$#  dt  binary  lcur  ioopt
    1.0000E-4   1
*DATABASE_ELOUT
$#  dt  binary  lcur  ioopt
    1.0000E-4   1
*DATABASE_GLSTAT
$#  dt  binary  lcur  ioopt
    1.0000E-4   1    0    1
*DATABASE_MATSUM
$#  dt  binary  lcur  ioopt
    1.0000E-4   1    0    1
*DATABASE_NCFORC
$#  dt  binary  lcur  ioopt
    1.0000E-4   1

```

```

*DATABASE_NODOUT
$# dt binary lcur iopt dthf binhf
1.0000E-4 1 0 0 0.000-842150451
*DATABASE_SLEOUT
$# dt binary lcur iopt
1.0000E-4 1
*DATABASE_BINARY_D3PLOT
$# dt lcdt beam npltc psetid
5.0000E-6
$# iopt
0
*DATABASE_EXTENT_BINARY
$# neiph neips maxint strflg sigflg epsflg rltflg engflg
0 0 0 1 1 1 2 1
$# cmpflg ieverp beamip dcomp shge stssz n3thdt ialemat
1 0 0 1 1 1 2
$# nintslid pkp_sen sclp unused msscl therm iniout iniout
0 1 1.000000 0 0 OALL ALL
$#*****
$# Bondary condation
$#*****
*BOUNDARY_NON_REFLECTING
$# ssid ad as
1 0.00 0.00
*BOUNDARY_SPC_SET_ID
$# id heading
0 y_top
$# nsid cid dofx dofy dofz dofrx dofry dofrz
1 0 1 1 1 1 1 1
*SET_NODE_LIST_TITLE
y_top
$# sid da1 da2 da3 da4
1 0.00 0.00 0.000 0.000
$# nid1 nid2 nid3 nid4 nid5 nid6 nid7 nid8
25383 25384 25435 25436 25487 25488 25539 25540
56558 56584 56610 56636 56662 56688 56714 56740
56766 56792 56818 56844 0 0 0 0
*BOUNDARY_SPC_SET_ID
$# id heading
0 x_right
$# nsid cid dofx dofy dofz dofrx dofry dofrz
3 0 0 0 0 0 0 0
*SET_NODE_LIST_TITLE
x_right
$# sid da1 da2 da3 da4
3 0.00 0.00 0.000 0.00
$# nid1 nid2 nid3 nid4 nid5 nid6 nid7 nid8
38139 38140 38141 38142 38143 38144 38145 38146
*BOUNDARY_SPC_SET_ID
$# id heading
0 y_bootm
$# nsid cid dofx dofy dofz dofrx dofry dofrz
2 0 1 1 1 1 1 1
*SET_NODE_LIST_TITLE
y_bootm
$# sid da1 da2 da3 da4
2 0.00 0.00 0.000 0.00

```

```

$# nid1 nid2 nid3 nid4 nid5 nid6 nid7 nid8
31311 31312 31363 31364 31415 31416 31467 31468

```

```

$#*****

```

```

$# Material Definition

```

```

$#*****

```

```

*PART

```

```

$# title

```

```

projectile in steel

```

```

$# pid secid mid eosid hgid grav adpopt tmid
1 1 1 1 1

```

```

*SECTION_SOLID

```

```

$# secid elform aet
1 1

```

```

*MAT_ELASTIC_PLASTIC_HYDRO

```

```

$# mid ro g sigy eh pc fs charl
1 7.870E-9 86000.000 215.00000 200000.0 0.0000 0.200000 0.000

```

```

$# eps1 eps2 eps3 eps4 eps5 eps6 eps7 eps8
0.000 0.000 0.000 0.000 0.000 0.000 0.000 0.000

```

```

$# eps9 eps10 eps11 eps12 eps13 eps14 eps15 eps16
0.000 0.000 0.000 0.000 0.000 0.000 0.000 0.000

```

```

$# es1 es2 es3 es4 es5 es6 es7 es8
0.000 0.000 0.000 0.000 0.000 0.000 0.000 0.000

```

```

$# es9 es10 es11 es12 es13 es14 es15 es16
0.000 0.000 0.000 0.000 0.000 0.000 0.000 0.000

```

```

*EOS_GRUNEISEN

```

```

$# eosid c s1 s2 s3 gamao a e0
1 4.570e6 1.490000 0.000 0.000 2.20000 1.500000 0.000

```

```

$# v0
0.000

```

```

*HOURGLASS

```

```

$# hgid ihq qm ibq q1 q2 qb/vdc qw
1 4 .03

```

```

*PART

```

```

$# title

```

```

composite material 0/90 degree fibre direction

```

```

$# pid secid mid eosid hgid grav adpopt tmid
2 2 2 0 2

```

```

*SECTION_SOLID

```

```

$# secid elform aet
2 1

```

```

*MAT_COMPOSITE_FAILURE_SOLID_MODEL

```

```

$ DEFINITION OF MATERIAL 2

```

```

$# mid ro ea eb ec prba prca prcb
2 1.5120E-9 72200.000 72200.000 1120.0000 0.040000 4.0000E-4 0.044000

```

```

$# gab gbc gca kf aopt macf
6000.0000 6000.0000 6000.0000 300.00000 2.000000 1.000000

```

```

$# xp yp zp a1 a2 a3
0.000 0.000 0.000 1.000000

```

```

$# v1 v2 v3 d1 d2 d3 beta
0.000 0.000 0.000 1.000 1.000000

```

```

$# sba sca scb xxc yyc zzc
100.00000 160.29999 160.29999 698.00000 833.00000 16980.000

```

```

$# xxt yyt zzt
833.00000 698.00000 233.00000

```

```

*HOURGLASS

```

```

$# hgid ihq qm ibq q1 q2 qb/vdc qw
2 4 0.010000

```

```

*PART
$# title
composite material 45/-45 degree fibre direction
$# pid secid mid eosid hgid grav adpopt tmid
   3   3   3   0   3
*SECTION_SOLID
$# secid elform aet
   3   1
*MAT_COMPOSITE_FAILURE_SOLID_MODEL
$ DEFINITION OF MATERIAL 3
$# mid ro ea eb ec prba prca prcb
   3 1.5120E-9 72200.000 72200.000 1120.0000 0.040000 4.0000E-4 0.044000
$# gab gbc gca kf aopt macf
6000.0000 6000.0000 6000.0000 300.00000 2.000000 1.000000
$# xp yp zp a1 a2 a3
   0.000 0.000 0.000 1.000000 1.000000
$# v1 v2 v3 d1 d2 d3 beta
   0.000 0.000 0.000 0.000 1.000000
$# sba sca scb xxc yyc zzc
100.00000 160.29999 160.29999 698.00000 833.00000 16980.000
$# xxt yyt zzt
833.00000 698.00000 233.00000
*HOURGLASS
$# hgid ihq qm ibq q1 q2 qb/vdc qw
   3   4 0.010000
*PART
$# title
composite material 0/90 degree fibre direction
$# pid secid mid eosid hgid grav adpopt tmid
   4   4   4   0   4
*SECTION_SOLID
$# secid elform aet
   4   1
*MAT_COMPOSITE_FAILURE_SOLID_MODEL
$ DEFINITION OF MATERIAL 4
$# mid ro ea eb ec prba prca prcb
   4 1.5120E-9 72200.000 72200.000 1120.0000 0.040000 4.0000E-4 0.044000
$# gab gbc gca kf aopt macf
6000.0000 6000.0000 6000.0000 300.00000 2.000000 1.000000
$# xp yp zp a1 a2 a3
   0.000 0.000 0.000 1.000000
$# v1 v2 v3 d1 d2 d3 beta
   0.000 0.000 0.000 1.000000 1.000000
$# sba sca scb xxc yyc zzc
100.00000 160.29999 160.29999 698.00000 833.00000 16980.000
$# xxt yyt zzt
833.00000 698.00000 233.00000
*HOURGLASS
$# hgid ihq qm ibq q1 q2 qb/vdc qw
   4   4 0.010000
*PART
$# title
composite material 45/-45 degree fibre direction
$# pid secid mid eosid hgid grav adpopt tmid
   5   5   5   0   5
*SECTION_SOLID
$# secid elform aet

```

```

5      1
*MAT_COMPOSITE_FAILURE_SOLID_MODEL
$ DEFINITION OF MATERIAL 5
$# mid ro ea eb ec prba prca prcb
5 1.5120E-9 72200.000 72200.000 1120.0000 0.040000 4.0000E-4 0.044000
$# gab gbc gca kf aopt macf
6000.0000 6000.0000 6000.0000 300.00000 2.000000 1.000000
$# xp yp zp a1 a2 a3
0.000 0.000 0.000 1.000000 1.000000
$# v1 v2 v3 d1 d2 d3 beta
0.000 0.000 0.000 0.000 1.000000
$# sba sca scb xxc yyc zzc
100.00000 160.29999 160.29999 698.00000 833.00000 16980.000
$# xxt yyt zzt
833.00000 698.00000 233.00000
*HOURGLASS
$# hgid ihq qm ibq q1 q2 qb/vdc qw
5 4 0.010000
*PART
$# title
composite material 0/90 degree fibre direction
$# pid secid mid eosid hgid grav adpopt tmid
6 6 6 0 6
*SECTION_SOLID
$# secid elform aet
6 1
*MAT_COMPOSITE_FAILURE_SOLID_MODEL
$ DEFINITION OF MATERIAL 6
$# mid ro ea eb ec prba prca prcb
6 1.5120E-9 72200.000 72200.000 1120.0000 0.040000 4.0000E-4 0.044000
$# gab gbc gca kf aopt macf
6000.0000 6000.0000 6000.0000 300.00000 2.000000 1.000000
$# xp yp zp a1 a2 a3
0.000 0.000 0.000 1.000000
$# v1 v2 v3 d1 d2 d3 beta
0.000 0.000 0.000 1.000000 1.000000
$# sba sca scb xxc yyc zzc
100.00000 160.29999 160.29999 698.00000 833.00000 16980.000
$# xxt yyt zzt
833.00000 698.00000 233.00000
*HOURGLASS
$# hgid ihq qm ibq q1 q2 qb/vdc qw
6 4 0.010000
*PART
$# title
composite material 45/-45 degree fibre direction
$# pid secid mid eosid hgid grav adpopt tmid
7 7 7 0 7
*SECTION_SOLID
$# secid elform aet
7 1
*MAT_COMPOSITE_FAILURE_SOLID_MODEL
$ DEFINITION OF MATERIAL 7
$# mid ro ea eb ec prba prca prcb
7 1.5120E-9 72200.000 72200.000 1120.0000 0.040000 4.0000E-4 0.044000
$# gab gbc gca kf aopt macf
6000.0000 6000.0000 6000.0000 300.00000 2.000000 1.000000

```



```

$# xp yp zp a1 a2 a3
0.000 0.000 0.000 1.000000 1.000000
$# v1 v2 v3 d1 d2 d3 beta
0.000 0.000 0.000 0.000 1.000000
$# sba sca scb xxc yyc zzc
100.00000 160.29999 160.29999 698.00000 833.00000 16980.000
$# xxt yyt zzt
833.00000 698.00000 233.00000
*HOURLASS
$# hgid ihq qm ibq q1 q2 qb/vdc qw
7 4 0.010000
*PART
$# title
composite material 0/90 degree fibre direction
$# pid secid mid eosid hgid grav adpopt tmid
8 8 8 0 8
*SECTION_SOLID
$# secid elform aet
8 1
*MAT_COMPOSITE_FAILURE_SOLID_MODEL
$ DEFINITION OF MATERIAL 8
$# mid ro ea eb ec prba prca prcb
8 1.5120E-9 72200.000 72200.000 1120.0000 0.040000 4.0000E-4 0.044000
$# gab gbc gca kf aopt macf
6000.0000 6000.0000 6000.0000 300.00000 2.000000 1.000000
$# xp yp zp a1 a2 a3
0.000 0.000 0.000 1.000000
$# v1 v2 v3 d1 d2 d3 beta
0.000 0.000 0.000 1.000000 1.000000
$# sba sca scb xxc yyc zzc
100.00000 160.29999 160.29999 698.00000 833.00000 16980.000
$# xxt yyt zzt
833.00000 698.00000 233.00000
*HOURLASS
$# hgid ihq qm ibq q1 q2 qb/vdc qw
8 4 0.010000
*PART
$# title
composite material 45/-45 degree fibre direction
$# pid secid mid eosid hgid grav adpopt tmid
9 9 9 0 9
*SECTION_SOLID
$# secid elform aet
9 1
*MAT_COMPOSITE_FAILURE_SOLID_MODEL
$ DEFINITION OF MATERIAL 9
$# mid ro ea eb ec prba prca prcb
9 1.5120E-9 72200.000 72200.000 1120.0000 0.040000 4.0000E-4 0.044000
$# gab gbc gca kf aopt macf
6000.0000 6000.0000 6000.0000 300.00000 2.000000 1.000000
$# xp yp zp a1 a2 a3
0.000 0.000 0.000 1.000000 1.000000
$# v1 v2 v3 d1 d2 d3 beta
0.000 0.000 0.000 0.000 1.000000
$# sba sca scb xxc yyc zzc
100.00000 160.29999 160.29999 698.00000 833.00000 16980.000
$# xxt yyt zzt

```

```

833.00000 698.00000 233.00000
*HOURGLASS
$# hgid ihq qm ibq q1 q2 qb/vdc qw
   9   4 0.010000
*PART
$# title
composite material 0/90 degree fibre direction
$# pid secid mid eosid hgid grav adpopt tmid
   10   10   10   0   10
*SECTION_SOLID
$# secid elform aet
   10   1
*MAT_COMPOSITE_FAILURE_SOLID_MODEL
$ DEFINITION OF MATERIAL 10
$# mid ro ea eb ec prba prca prcb
   10 1.5120E-9 72200.000 72200.000 1120.0000 0.040000 4.0000E-4 0.044000
$# gab gbc gca kf aopt macf
6000.0000 6000.0000 6000.0000 300.00000 2.000000 1.000000
$# xp yp zp a1 a2 a3
   0.000 0.000 0.000 1.000000
$# v1 v2 v3 d1 d2 d3 beta
   0.000 0.000 0.000 1.000000 1.000000
$# sba sca scb xxc yyc zzc
100.00000 160.29999 160.29999 698.00000 833.00000 16980.000
$# xxt yyt zzt
833.00000 698.00000 233.00000
*HOURGLASS
$# hgid ihq qm ibq q1 q2 qb/vdc qw
   10   4 0.010000
*PART
$# title
composite material 0/90 degree fibre direction
$# pid secid mid eosid hgid grav adpopt tmid
   11   11   11   0   11
*SECTION_SOLID
$# secid elform aet
   11   1
*MAT_COMPOSITE_FAILURE_SOLID_MODEL
$ DEFINITION OF MATERIAL 11
$# mid ro ea eb ec prba prca prcb
   11 1.5120E-9 72200.000 72200.000 1120.0000 0.040000 4.0000E-4 0.044000
$# gab gbc gca kf aopt macf
6000.0000 6000.0000 6000.0000 300.00000 2.000000 1.000000
$# xp yp zp a1 a2 a3
   0.000 0.000 0.000 1.000000
$# v1 v2 v3 d1 d2 d3 beta
   0.000 0.000 0.000 1.000000 1.000000
$# sba sca scb xxc yyc zzc
100.00000 160.29999 160.29999 698.00000 833.00000 16980.000
$# xxt yyt zzt
833.00000 698.00000 233.00000
*HOURGLASS
$# hgid ihq qm ibq q1 q2 qb/vdc qw
   11   4 0.010000
*PART
$# title
composite material 45/-45 degree fibre direction

```

```

$# pid secid mid eosid hgid grav adpopt tmid
   12  12  12   0   12
*SECTION_SOLID
$# secid elform aet
   12   1
*MAT_COMPOSITE_FAILURE_SOLID_MODEL
$ DEFINITION OF MATERIAL 12
$# mid ro ea eb ec prba prca prcb
   12 1.5120E-9 72200.000 72200.000 1120.0000 0.040000 4.0000E-4 0.044000
$# gab gbc gca kf aopt macf
 6000.0000 6000.0000 6000.0000 300.00000 2.000000 1.000000
$# xp yp zp a1 a2 a3
   0.000 0.000 0.000 1.000000 0.000000
$# v1 v2 v3 d1 d2 d3 beta
   0.000 0.000 0.000 1.000 1.000000
$# sba sca scb xxc yyc zzc
100.00000 160.29999 160.29999 698.00000 833.00000 16980.000
$# xxt yyt zzt
833.00000 698.00000 233.00000
*HOURGLASS
$# hgid ihq qm ibq q1 q2 qb/vdc qw
   12  4 0.010000

```

```

$#*****
$# Erosion condation
$#*****

```

```

*MAT_ADD_EROSION
$# mid excl mxpres mneps
   2
$# mnpres sigp1 sigvm mxeps epssh sigth impulse failtm
   0.000 0.000 0.000 0.800000
*MAT_ADD_EROSION
$# mid excl mxpres mneps
   3
$# mnpres sigp1 sigvm mxeps epssh sigth impulse failtm
   0.000 0.000 0.000 0.800000
*MAT_ADD_EROSION
$# mid excl mxpres mneps
   4
$# mnpres sigp1 sigvm mxeps epssh sigth impulse failtm
   0.000 0.000 0.000 0.800000
*MAT_ADD_EROSION
$# mid excl mxpres mneps
   5
$# mnpres sigp1 sigvm mxeps epssh sigth impulse failtm
   0.000 0.000 0.000 0.800000
*MAT_ADD_EROSION
$# mid excl mxpres mneps
   6
$# mnpres sigp1 sigvm mxeps epssh sigth impulse failtm
   0.000 0.000 0.000 0.800000
*MAT_ADD_EROSION
$# mid excl mxpres mneps
   7
$# mnpres sigp1 sigvm mxeps epssh sigth impulse failtm
   0.000 0.000 0.000 0.800000
*MAT_ADD_EROSION

```

```

$# mid excl mxpres mneps
8
$# mnpres sigp1 sigvm mxeps epssh sigth impulse failtm
0.000 0.000 0.000 0.800000
*MAT_ADD_EROSION
$# mid excl mxpres mneps
9
$# mnpres sigp1 sigvm mxeps epssh sigth impulse failtm
0.000 0.000 0.000 0.800000
*MAT_ADD_EROSION
$# mid excl mxpres mneps
10
$# mnpres sigp1 sigvm mxeps epssh sigth impulse failtm
0.000 0.000 0.000 0.800000
*MAT_ADD_EROSION
$# mid excl mxpres mneps
11
$# mnpres sigp1 sigvm mxeps epssh sigth impulse failtm
0.000 0.000 0.000 0.800000
*MAT_ADD_EROSION
$# mid excl mxpres mneps
12
$# mnpres sigp1 sigvm mxeps epssh sigth impulse failtm
0.000 0.000 0.000 0.800000

```

```

$#*****

```

```

$# Projectile Velocity

```

```

$#*****

```

```

*INITIAL_VELOCITY_GENERATION

```

```

$#nsid/pid styp omega vx vy vz ivatn
4 3 0.000 0.000 0.000 -2.00E+5 0
$# xc yc zc nx ny nz phase iridid
0.000 0.000 0.000 0.000 0.000 0.000 0 0

```

```

*SET_NODE_LIST_TITLE

```

```

projectile

```

```

$# sid da1 da2 da3 da4
4 0.000 0.000 0.000 0.000
$# nid1 nid2 nid3 nid4 nid5 nid6 nid7 nid8
64957 64958 64959 64960 64961 64962 64963 64964
68406 68407 68408 68409 68410 68411 68412 68413
68414 68415 65455 0 0 0 0 0

```

```

*SET_SEGMENT

```

```

$# sid da1 da2 da3 da4
1 0.000 0.000 0.000 0.000
$# n1 n2 n3 n4 a1 a2 a3 a4
25383 25384 25436 25435 0.000 0.000 0.000 0.000
64254 64930 64956 64280 0.000 0.000 0.000 0.000

```

```

$#*****

```

```

$# Element and Node

```

```

$#*****

```

```

*ELEMENT_SOLID

```

```

$ ELEMENT CARDS FOR SOLID ELEMENTS

```

```

$# eid pid n1 n2 n3 n4 n5 n6 n7 n8
1 2 1 21 23 3 2 22 24 4
60742 1 68390 68415 67596 67591 67169 67170 67176 67175

```

```

*NODE

```

```

$ NODES

```

```

$# nid      x      y      z      tc      rc
   1      0.000    0.000    0.000    1      5
   2      0.000    0.000    0.3750000    1      5
68415    4.0042791    3.1595690    13.3595695    0      0
*END
$#*****

```

## APPENDIX C

**Truegrid and La-Dyna input file for repaired 11 plies composite Laminate subject to compression loading defined as:**

Then the steps length on Truegrid input file defined as:

```

C*****
C* create parameters r: hole radius D: adhesive thickness *
C* TAD: Laminate thickness Tall: total laminate length N: No. of step *
C* TR: relation between hole radius and total length of steps *
C*****
parameter r 12 D 0.375 TAD 6 N 3 TR 1 Tall 75
C*****
C* length of steps *
C*****
L1 [(%r*(%TR))/ %N] C* length of step 1
L2 [(%r*(%TR))/ %N] C* length of step 2
L3 [(%r*(%TR))/ %N] C* length of step 3
if (%N .eq. 4) then
L4 [(%r*(%TR))/ %N] C* length of step 4
Endif

```

Then the steps high on Truegrid input file defined as:

```

C*****
C* high of steps *
C*****
f [%N+1] C* applied this conduction to be sure the step high
if (%N .eq.3) then C* is equal layer thickness and match
f1 [%TAD/%f]
elseif (%N .eq. 4) then
f1 [(%TAD/%f)-0.075]
elseif (%N .eq. 5) then
f1 [(%TAD/%f)-0.25]
endif

h1 [%f1] C* high of step 1
h2 [%f1+%h1] C* high of step 2
h3 [%f1+%h2] C* high of step 3
if (%N .eq. 4) then
h4 [%f1+%h3] C* high of step 4

```

endif

The outer boundary and tip of steps has been defined as critical points in this model. These points have been used to control length, height, and the number of steps. These points on Truegrid input file are defined as:

```
C*****
C* defined critical points in geometry which control of high and length of steps *
C*****
k1 0
k4 0
k5 %TAD
k8 %TAD
k9 %h1
k10 [%h1+%D]
k11 %h2
k12 [%h2+%D]
k13 %h3
k14 [%h3+%D]
if (%N .eq. 4) then
k15 %h4
k16 [%h4+%D]
endif
k19 %TAD

k20 %r
k21 [%r+%D]
k22 [%r+%L1]
k23 [%r+%L1+%D]
k24 [%r+%L1+%L2]
k25 [%r+%L1+%L2+%D]
k26 [%r+%L1+%L2+%L3]
k27 [%r+%L1+%L2+%L3+%D]
if (%N .eq. 4) then
k28 [%r+%L1+%L2+%L3+%L4]
k29 [%r+%L1+%L2+%L3+%L4+%D]
endif
if (%N .eq. 3)then
k31 %k27
k15 %k19
elseif (%N .eq. 4) then
k31 %k29
k17 %k19
endif;
```

The main factor in this part of the model was maintaining the aspect ratio for the element less than five. Then these parts were defined on the Truegrid input file as:

```
C*****
C* This part to defined mesh size and material type for composite *
C* area out of repair area by used cylinder and sphere model technic *
C*****
cylinder 1 [(((%k31+2)-%k31))+1]; 1 [(((%k20/%D))-7);
1 2 3 4 5 6 7 8 9 10 11 12 13 14 15 16 17;
%k31 [%k31+3]; 0 90; 0 .375 .75 1.125 1.5 1.875 2.25 2.625
3 3.375 3.75 4.125 4.5 4.875 5.25 5.625 6;
```

```

block 1 [((%k20/%D)/2)-3]; 1 [((%k20/%D)/2)+15];
1 2 3 4 5 6 7 8 9 10 11 12 13 14 15 16 17;
0 [(%k31+3)*0.707]; [(%k31+3)*0.707] %TAll;
0 .375 .75 1.125 1.5 1.875 2.25 2.625 3
3.375 3.75 4.125 4.5 4.875 5.25 5.625 6;
sfi ; -1 2; ;cy 0 0 0 0 7 [%k31+3];

```

C\* project regions onto a surface

```

block 1 [((%k20/%D)/2)+15]; 1 [((%k20/%D)/2)-3];
1 2 3 4 5 6 7 8 9 10 11 12 13 14 15 16 17;
[(%k31+3)*0.707] %TAll; 0 [(%k31+3)*0.707];
0 .375 .75 1.125 1.5 1.875 2.25 2.625 3
3.375 3.75 4.125 4.5 4.875 5.25 5.625 6;
sfi -1 2; ; ;cy 0 0 0 0 7 [%k31+3];
block 1 [((%k20/%D)/2)+15]; 1 [((%k20/%D)/2)+15];
1 2 3 4 5 6 7 8 9 10 11 12 13 14 15 16 17;
[(%k31+3)*0.707] %TAll; [(%k31+3)*0.707] %TAll;
0 .375 .75 1.125 1.5 1.875 2.25 2.625 3
3.375 3.75 4.125 4.5 4.875 5.25 5.625 6;

```

C\* project regions onto a surface

In TrueGrid input file was defined the hole area (joint) after repaired as:

```

C*****
C* This part to defined mesh size and material type for hole (joint) area *
C* by used cylinder and sphere projection technic *
C*****

```

```

block
1 [((%k20/%D)/4)-1] [((%k20/(%D))/4)+2];
1 [((%k20/%D)/4)-1] [((%k20/(%D))/4)+2];
1 2 3 4 5 6 7 8 9 10 11 12 13 14 15 16 17;
0 [%k20/3] [%k20/3]; 0 [%k20/3] [%k20/3];
0 .375 .75 1.125 1.5 1.875 2.25 2.625 3 3.375
3.75 4.125 4.5 4.875 5.25 5.625 6;
dei 2 3; 2 3;;
sfi 1 -3;1 -3;1 17;cy 0 0 0 0 1 [%r-4];

```

C\* delete regions of the part

C\* project regions onto a surface

```

cylinder 1 3; 1 [((%k20/%D)/2)-3]; 1 2 3 4 5 6
7 8 9 10 11 12 13 14 15 16 17; [%r-4] [%r-2];
0 90; 0 .375 .75 1.125 1.5 1.875 2.25 2.625 3
3.375 3.75 4.125 4.5 4.875 5.25 5.625 6;
bb 2 1 1 2 2 17 1;

```

C\* block boundary interface and Master side 1 definition

```

cylinder 1 3; 1 [((%k20/%D))-7]; 1 2 3 4 5 6 7
8 9 10 11 12 13 14 15 16 17; [%r-2] [%r]; 0 90;
0 .375 .75 1.125 1.5 1.875 2.25 2.625 3 3.375
3.75 4.125 4.5 4.875 5.25 5.625 6;
trbb 1 1 1 1 2 17 1;

```

C\* block boundary interface and Slave side 1 definition

In next step was defined the steps area in three parts joint, parent and adhesive and in next paragraph has been described first step as example.

```

C*****
C* This part to defined mesh size and material type for joint part *
C* (steps area) by used cylinder model technic *
C*****
C*****

```

```

C* Model first step with different possible high and length *
C*****
if (%k10 .eq. 0.75) then
high step

```

```

cylinder 1 [(%k22-%k20)]; 1 [(%k20/%D)-7];
1 2 3 4 5 6 7 8 9 10 11 12 13 14 15; %k20 %k22;
0 90; [%k10] [%k10+0.375] [%k10+0.75]
[%k10+1.125] [%k10+1.5] [%k10+1.875] [%k10+2.25]
[%k10+2.625] [%k10+3] [%k10+3.375] [%k10+3.75]
[%k10+4.125] [%k10+4.5] [%k10+4.875] [%k10+5.25];

```

```

elseif (%k10 .eq. 1.125) then
cylinder 1 [(%k22-%k20)]; 1 [(%k20/%D)-7];
1 2 3 4 5 6 7 8 9 10 11 12 13 14; %k20 %k22; 0 90;
[%k10] [%k10+0.375] [%k10+0.75] [%k10+1.125]
[%k10+1.5] [%k10+1.875] [%k10+2.25] [%k10+2.625]
[%k10+3] [%k10+3.375] [%k10+3.75]
[%k10+4.125] [%k10+4.5] [%k10+4.875];

```

```

elseif (%k10 .eq. 1.5)then
cylinder 1 [(%k22-%k20)]; 1 [(%k20/%D)-7];
1 2 3 4 5 6 7 8 9 10 11 12 13; %k20 %k22; 0 90;
[%k10] [%k10+0.375] [%k10+0.75] [%k10+1.125]
[%k10+1.5] [%k10+1.875] [%k10+2.25] [%k10+2.625]
[%k10+3] [%k10+3.375] [%k10+3.75]
[%k10+4.125] [%k10+4.5];
Endif

```

```

C*****
C* This part to defined mesh size and material type for Parent part *
C* (steps area) by used Cylinder model technic *
C*****
C* Model first step with different possible high and length *
C*****

```

```

if (%k9 .eq. 0.375)then
cylinder 1 [(%k23-%k21)]; 1 [(%k20/%D)-7]; 1 2;
%k21 %k23; 0 90; [%k9-0.375] [%k9];

```

```

elseif (%k9 .eq. 0.75)then
cylinder 1 [(%k23-%k21)]; 1 [(%k20/%D)-7]; 1 2 3;
%k21 %k23; 0 90; [%k9-0.75] [%k9-0.375] [%k9];

```

```

elseif (%k9 .eq. 1.125)then
cylinder 1 [(%k23-%k21)];1 [(%k20/%D)-7]; 1 2 3 4;
%k21 %k23; 0 90; [%k9-1.125] [%k9-0.75] [%k9-0.375] [%k9];
endif

```

```

C*****
C* This part to difened mesh size and material type for adhesive *
C* area by used Cylinder model technic *
C*****
C* Model first step with different possible high and length *
C*****

```



```
cylinder 1 [2*((%k21-%k20)/%D)+1]; 1 [(2*(%k20/%D))+9];
1 [2*((%k9-%k4)/%D)+1]; %k20 %k21; 0 90; %k4 %k9;
```

```
cylinder 1 [2*((%k21-%k20)/%D)+1]; 1 [(2*(%k20/%D))+9];
1 [2*((%k10-%k9)/%D)+1]; %k20 %k21; 0 90; %k9 %k10;
```

```
cylinder 1 [2*((%k22-%k21)/%D)+1]; 1 [(2*(%k20/%D))+9];
1 [2*((%k10-%k9)/%D)+1]; %k21 %k22; 0 90; %k9 %k10;
```

The adhesive surface sign as slave and other surfaces (joint and parent) sign as master

```
C*****
C* Sliding interfaces contact between Adhesive and composite Material *
C*****
sid 1 ldsi 2;
sid 25 ldsi 2;
sid 44 ldsi 2;
```

The next paragraph presents part of LSDYNA input file, with the detail of).

```
$#*****
$# LS-DYNA Keyword file for repaired composite laminate *
$# subject to compression load *
$#*****
*KEYWORD 90000000
*TITLE
$#*****
$# title
lsdyna model: repaired laminate by stepped joint under compression load
$#*****
$# Dified Dynamic relaxation and damping parameters
$#*****
*CONTROL_DYNAMIC_RELAXATION
$# nrcyck drtol drfctr drterm tssfdr irelal edttl idrflg
250 0.001 5.995 0.00 0.00 0 0.04 0
*DAMPING_GLOBAL
$# lcid valdmp stx sty stz srx sry srz
0 1800.0 90.0 90.0 90.0 0.00 0.00 0.00
*DAMPING_PART_STIFFNESS
$# pid coef
2 0.20
:
:
*DAMPING_PART_STIFFNESS
$# pid coef
34 0.20
$#*****
$# Contact Algorithm
$#*****
*CONTROL_CONTACT
$# slsfac rwpnal islchk shlthk penopt thkchg orien enmass
0.100 0.0 0 0 2 0 1 0
$# usrstr usrfrc nsbcs interm xpene ssthk ecdt tiedprj
0 0 0 0 4.0 0 0 0
```

```

$# sfric  dfric  edc  vfc  th  th_sf  pen_sf
   0.0    0.0    0.0  0.0  0.0  0.0    0.0
$# ignore frceng skiprwg outseg spotstp spotdel spothin
   0      0      0      0      0      0      0.000
$# isym  nserod  rwgaps  rwgth  rwksf  icov  swradf  ithoff
   0      0      0      0.0  1.0    0      0.0    0
$# shledg
   0

```

\*CONTACT\_ERODING\_SINGLE\_SURFACE\_ID

```

$# cid title
   1 TrueGrid
$# ssid  msid  sstyp  mstyp  sboxid  mboxid  spr  mpr
   0      0      5      5      0      0      0      0
$# fs  fd  dc  vc  vdc  penchk  bt  dt
   0.1  0.3  0.0  0.0  0.0  1  1.0e-9
$# sfs  sfm  sst  mst  sfst  sfmt  fsf  vsf
   1.00  1.00
$# isym  erosop  iadj
   1      1      1
$# soft  sofsc1  lcidab  maxpar  sbopt  depth  bsort  frcfrq
   1  0.10  0  1.025  2.0  2  0  1
$# penmax  thkopt  shlthk  snlog  isym  i2d3d  sldthk  sldstf
   0.0  0  0  0  0  0  0.0  0.0

```

\*CONTACT\_TIED\_SURFACE\_TO\_SURFACE\_ID

```

25, TrueGrid Sliding Interface # 25
$# ssid  msid  sstyp  mstyp  sboxid  mboxid  spr  mpr
   1  2  0  0  0  0  0  0
$# fs  fd  dc  vc  vdc  penchk  bt  dt
   0.1  0.3  0.0  0.0  0.0  1  1.0e-9
$# sfs  sfm  sst  mst  sfst  sfmt  fsf  vsf
   10.0  20.0  0.0  0.0  0.0  0.0  0.0  0.0
$# soft  sofsc1  lcidab  maxpar  sbopt  depth  bsort  frcfrq
   1  0.10  0  1.025  2.0  2  0  1

```

```

$#*****
$#          Boundary condation
$#*****

```

\*BOUNDARY\_PRESCRIBED\_MOTION\_SET\_ID

```

$# id heading
   0  move
$# nsid  dof  vad  lcid  sf  vid  death  birth
   1  2  2  1  -1.0  0  1.E+28  0.0

```

\*BOUNDARY\_SPC\_SET\_ID

```

$# id heading
   1  move
$# nsid  cid  dofz  dofz  dofz  dofz  dofz  dofz
   1  0  1  0  1  1  1  1

```

\*BOUNDARY\_SPC\_SET\_ID

```

$# id heading
   0  consntrate
$# nsid  cid  dofz  dofz  dofz  dofz  dofz  dofz
   2  0  1  1  1  1  1  1

```

\*DEFINE\_CURVE\_TITLE

```

displacement
$# lcid  sidr  sfa  sfo  offa  offo  dattyp
   1  0  1.0  1.0  0.0  0.0  0

```

```

$#          a1          o1
           0.0         0.0
           1.0        300.0

```

```

$#*****
$#                               Material
$#*****

```

```

*PART
$# title
composite material 45/-45 degree fibre direction
$# pid  secid  mid  eosid  hgid  grav  adpopt  tmid
   2    2    2    0    2    0    0    0
*SECTION_SOLID
$# secid  elform  aet
   2    1    0
*MAT_COMPOSITE_FAILURE_SOLID_MODEL
$ DEFINITION OF MATERIAL 3
$# mid  ro  ea  eb  ec  prba  prca  prcb
   2 1.5E-9 72200.0 72200.0 1120.0 0.04 4.0E-4 0.04
$# gab  gbc  gca  kf  aopt  macf
 6000.0 6000.0 6000.0 6000.0 2.0 1.0
$# xp  yp  zp  a1  a2  a3
  0.0  0.0  0.0  1.0  0.0  0.0
$# v1  v2  v3  d1  d2  d3  beta
  0.0  0.0  0.0  1.0  1.0  0.0  0.0
$# sba  sca  scb  xxc  yyc  zzc
 833.0 350.0 350.0 698.0 833.0 880.0
$# xxt  yyt  zzt
 833.0 698.0 888.0
*HOURGLASS
$# hgid  ihq  qm  ibq  q1  q2  qb/vdc  qw
   2    4  0.01  0  0.0  0.0  0.0  0.0

```

```

*MAT_ADD_EROSION
$# mid  excl  mxpres  mneps  effeps  voleps  numfip  ncs
   2    0.0  0.0  0.0  0.0  0.0  0.0  0.0
$# mnpres  sigp1  sigvm  mxeps  epssh  sigth  impulse  failtm
  0.0  0.0  0.0  0.025  0.0  0.0  0.0  0.0

```

```

*PART
$# title
adhesive linear
$# pid  secid  mid  eosid  hgid  grav  adpopt  tmid
  20    20    20    0    20    0    0    0
*SECTION_SOLID
$# secid  elform  aet
  20    1    0
*MAT_PIECEWISE_LINEAR_PLASTICITY_TITLE
adhesive
$# mid  ro  e  pr  sigy  etan  fail  tdel
  20 0.879E-9 2600 0.38 40.0 50.0 0.1585 1.0E-10
$# c  p  lcss  lcsr  vp
  0.0  0.0  0  0  0.0
$# eps1  eps2  eps3  eps4  eps5  eps6  eps7  eps8
  0.0  0.01  0.02  0.03  0.07  0.0  0.0  0.0
$# es1  es2  es3  es4  es5  es6  es7  es8
  0.0  20.0  40.0  40.0  40.0  0.0  0.0  0.0

```

\*HOURGLASS

\$#	hgid	ihq	qm	ibq	q1	q2	qb/vdc	qw
	20	4	0.03	0	0.0	0.0	0.0	0.